

# The tectonic evolution of the Bredasdorp Basin and its implications for oil and gas formation

---

**Rethabile Tau**

**Supervised by**

Dr Stephanie Enslin

Prof Musa Manzi

Dr Eric Saffou

A dissertation submitted to the Faculty of Science, University of the Witwatersrand in fulfilment of the requirements for the degree of Master of Science

School of Geosciences, Johannesburg

2023



# DECLARATION

I Rethabile Tau (800746) am a student registered for MSc in Geology in the year 2022, hereby declare the following:

- I am aware that plagiarism (the use of someone else's work without their permission and/or without acknowledging the original source) is wrong.
- I confirm that the work submitted for assessment for the above course is my own unaided work except where I have explicitly indicated otherwise.
- I have followed the required conventions in referencing the thoughts and ideas of others.
- I understand that the University of the Witwatersrand may take disciplinary action against me if there is a belief that this is not my own unaided work or that I have failed to acknowledge the source of the ideas or words in my writing.

**Signature**

  
\_\_\_\_\_

**Date**

27th October 2023

## ABSTRACT

The Bredasdorp Basin is an offshore rift basin located in the southernmost tip of Africa, within the larger Outeniqua Basin. Previous studies have indicated the presence of hydrocarbons, as well as structures or evidence that allude to the presence of hydrocarbons, where the basin has not yet been extensively drilled or explored. In this study, seismic attributes applied to high resolution pre-stack time migrated 3D seismic data are analyzed, in conjunction with well logs, specifically the gamma ray logs. By employing these methods, the study aims to delineate the presence of hydrocarbons and their migration, as well as deduce the evolution of the basin based on the structures observed. Using artificial neural network (ANN) to predict the lithologies and analyzing the patterns in the gamma ray logs, the stratigraphic results show that the basin begins with a marine dominated environment from the Valanginian age to Aptian age. From the Aptian to Albian age, there are consistent changes in sea level and sedimentation, caused by thermal sag and uplift. Past the Albian age to present age, the deposition environment is dominated by sandstones and coarse sediments. This is due to the evolving basin moving from a distal to a proximal environment of deposition. Using seismic attributes such as envelope attribute, edge detection and variance attribute, structures such as paleo pockmarks and fluid escape structures are identified. These identified paleo pockmarks have diameters ranging from 400m to 900m. In addition to these structures, erosive features were observed which could be classified as submarine channels or slump structures, with the dominating channel having depths of up to 1585 m. Using variance and ant-tracking, the fault structures observed of the study areas revealed two dominating phases of rifting. The first phase has horsts and grabens bounded by normal faults trending E-W, with implications that the rifting propagated N-S in this phase of rifting. This phase of rifting ends during the Aptian age. The next phase of rifting begins during the Santonian age, with the fault bound horsts and grabens trending N-S, which indicate an E-W rifting direction.

## **ACKNOWLEDGEMENTS**

My greatest gratitude goes out to my supervisors, Dr Stephanie Enslin, Prof Musa, and Dr Eric Saffou for their guidance, constructive criticism on my work and their constant support and advice. It has truly been an honor to learn from these individuals and integrate their expertise in my personal and work growth.

I would also like to extend many thanks to the National Research Fund (NRF) and Centre of Excellence of Integrated Mineral and Energy Resource Analysis (CIMERA) for their monetary support in the completion of this project. Additionally, I would like to acknowledge Wits Seismic Research Centre, Schlumberger PETREL 2018 and DUG Insight 2021 for the provision of the equipment and software to complete the interpretation of the data. Furthermore, the availability of the data would not have been possible, had it not been for PetroSA and their generosity in sharing the Bredasdorp Basin seismic data.

To the mentor that PetroSA introduced me to, Connie Nyapule, thank you for your guidance in both the data, how to navigate through the PETREL 2018 software and career advice and guidance.

I am also indebted to my colleagues in the Geophysics department, who helped me in understanding geophysics fundamentals to better enhance my understanding of my work, especially having been trained in mainly geology in my undergraduate and Honours years. Your guidance and support on those sleepless nights does not go unnoticed.

Last but certainly not least, to my friends and family, your unwavering support throughout these years, your words of encouragement and even help with managing my time as a young mother has been beyond what I could have asked for. I would not have been where I am today, finished writing this thesis had it not been for that extra support. Love and light to all.

# Contents

<i>DECLARATION</i> .....	<i>i</i>
<i>ABSTRACT</i> .....	<i>i</i>
<i>ACKNOWLEDGEMENTS</i> .....	<i>ii</i>
<i>1. INTRODUCTION</i> .....	<i>1</i>
<i>2. GEOLOGICAL BACKGROUND</i> .....	<i>6</i>
<i>3. SEISMIC REFLECTION THEORY AND WELL LOGS</i> .....	<i>12</i>
<i>4. METHODOLOGY</i> .....	<i>25</i>
<i>5. HORIZON PICKING USING STRATIGRAPHIC CORRELATION</i> .....	<i>40</i>
<i>6. FAULT PICKING USING VOLUMETRIC AND HORIZON ATTRIBUTES</i> .....	<i>51</i>
<i>7. EVIDENCE OF HYDROCARBON MIGRATION</i> .....	<i>58</i>
<i>8. TECTONIC EVOLUTION OF THE BREDASDORP BASIN</i> .....	<i>63</i>
<i>9. CONCLUSIONS</i> .....	<i>65</i>
<i>10. REFERENCES</i> .....	<i>67</i>

## Table of Figures

Figure 1.1	The split of West Gondwanaland, which included Africa, Antarctica, and South America, between 155 and 135 MA. b) The split between South America and Southwest Africa which caused the creation of half-grabens. The Agulhas Falkland Fracture Zone (AFFZ), also known as the dextral shear fracture zone, is situated south of Africa. Modified after Mahlalela (2018).	pp. 2
Figure 1.2	The Outeniqua Basin, a group of five rift basins with accompanying basement highs, off the coast of South Africa. The Infanta Arch on the east and Agulhas Arch on the west which are basement highs, define the Bredasdorp Basin, situated on the westernmost side. Study site is specifically in the field of operations (Petroleum Agency SA 2013)	pp. 2
Figure 2.1	a) The reconstruction of Gondwana and the respective paleopositions of the continents in the early Jurassic (200 Ma). b) The continents are pulled apart as seen at 160 Ma, c) Early Cretaceous (130 Ma) dextral shear movement was then seen (Fitzgerald, 2012). Labels: AP, Antarctic Peninsula; TI, Thurston Island; MBL, Marie Byrd Land; CR, Chatham Rise; CP, Campbell Plateau; SNZ, southern New Zealand; NNZ, northern New Zealand; LHR, Lord Howe Rise; WS, Weddell Sea.	pp. 7
Figure 2.2	Bredasdorp Basin chronostratigraphic column showing different seismic horizons labelled 1At, 5At1, 13At1, etc., which indicate type 1 erosive unconformities. The cyclical thermal subsidence, followed by uplift and erosion, is indicated by these seismic horizons (Sonibare et al, 2018). Indicated on the diagram as black, green, and red circles, respectively, are several source rock intervals as well as oil and gas.	pp.10
Figure 2.3	Hydrogen Index (HI) vs Tmax plot for the Bredasdorp Basin which shows that the oil and gas are both type II indicating the origin of the organic material to be that of marine (Van der Spuy, 2003).	pp. 11
Figure 2.4	The Outeniqua Basin, a group of five rift basins with accompanying basement highs, off the coast of South Africa. The Infanta Arch on the east and Agulhas Arch on the west which are basement highs, define the Bredasdorp Basin, situated on the westernmost side. Study site is specifically in the field of operations (Petroleum Agency SA 2013)	pp. 12
Figure 3.1	Schematic illustration of seismic survey vessel, with the source (airgun) and resultant raypaths reflected at different interfaces (changes in acoustic impedance). The streamer with hydrophones attached to it receives the reflected energy from different boundaries (Cameselle, 2016).	pp. 14
Figure 3.2	Open-hole logs and well logs with their characteristic profiles and units of measurement (Wong et al., 2009)	pp. 23
Figure 3.3	Sonic log displaying some typical responses of the lithology within the formation. The interval transit time ( $\Delta T$ ), which increases from right to left, shale and coal typically have high $\Delta T$ values whilst compacted rock will result in low $\Delta T$ . The effect of compaction is especially obvious in the thickest shale layer whereby $\Delta T$ decreases as the rock transitions from less compact to compact. Adapted after Rider, 1986.	pp. 24

Figure 4.1	Figure 4.1: The summarized methodology workflow used in the study. The data processing section of the workflow was done by the company that provided the data, whilst the seismic interpretation workflow is part of this study's workflow.	pp. 26
Figure 4.2	Well to seismic tie displaying gamma ray (GR), resistivity (SFLU) and sonic log (DT) from FO-. Sonic and density logs were used to produce a synthetic seismogram, which matches the well log as the peaks on the seismic panel.	pp. 27
Figure 4.3	Figure 4.3: a) Location map of wells; b) A NE-SW section well correlation from FO-1 (far left), F-08 and F-06 showing the horizons, gamma ray log (GR) and sonic log (DT) c) A WNW-ESE section showing well correlation from F-01 (far left), F-R1 and F-S1. The well correlations images display the use of gamma ray log (GR) and sonic log (DT) and how it relates to the facies such as sandstone, siltstone and shale.	pp. 28
Figure 4.4	Seismic section showing all the horizons picked, starting from lAt1, which is Valanginian in age, up to the present- day sea floor of the Bredasdorp Basin.	pp. 32
Figure 4.5	Chaos sections showing variations of parameters with the inline and crossline as indicators of position. a) Seismic chaos section with sigma filter of 2.5 in the X, Y, Z directions. b) Z slice at the TWT 1467 showing the sigma filter of X, Y, Z in the range of 2.5. c) Seismic chaos section (same as a) with the sigma filter of 1.5 in the X, Y, Z directions. D) Z slice at TWT 1467 showing the sigma filter of X, Z, Y in the range of 1.5.	pp. 34
Figure 4.6	Seismic section with the variance attribute applied with different parameters. These parameters include: a) Dip correction on with crossline and inline range of 2 and vertical smoothing of 8; b) Dip correction off with crossline and inline range of 2 and vertical smoothing of 8; c) Dip correction on with the same crossline and inline range of 2 and vertical smoothing of 15; d) Dip correction off with same crossline and inline range, and vertical smoothing; e) Dip correction on crossline and inline range of 3 with vertical smoothing of 8; f) Dip correction off with crossline and inline range of 3, with vertical smoothing of 8. Within the yellow and red circles, these are the faults used to compare the increase or decrease of resolution as the parameters are changed.	pp. 35
Figure 4.7	Stereonet filter used for ant-track to determine which dip and azimuth would be accepted for extracting faults. The gray area is the range of azimuth that was rejected, and the white is the range of azimuth that was accepted when running the ant-tracking filter. The red arrow indicates that the azimuth is the region 'around' the Stereonet and the black arrow shows the dip which goes from degrees at the center of the Stereonet to 90 degrees at the outer edge of the circle/Stereonet. The accepted region has a dip ranging from 0° to 90° and Azimuth ranging from 285 to 150 (top). Conversely, the rejected region has a dip of 150 to 285 and an azimuth ranging from 75 to 330.	pp. 39

Figure 5.1	Figure 5.1: Sonic velocities (DT) versus gamma ray values (GR) for a range of rock types. Coarse sandstones show low sonic velocities (DT) and gamma values (GR), medium grained sandstones show low sonic velocity values but range in gamma ray values, siltstones have medium to high gamma and sonic values, whilst shale shows highest gamma ray and sonic values. This data was obtained using FO-1, FS-1 and FR-1 wells	pp. 41
Figure 5.2	Stratigraphic patterns showing onlap, downlap, and toplap, in relation to the top or bottom stratigraphy (Mountain et al, 2007).	pp. 43
Figure 5.3	The four basic seismic reflection configurations (Papadimitriou, 2017).	pp. 43
Figure 5.4	Terminating stratal patterns on inline 2330 displaying toplap termination against a younger top boundary, onlap terminating against older strata, and downlap terminating downward against older strata.	pp. 43
Figure 5.5	The red arrows show top, which is strata below the 14At1 horizon, truncating onto it. While a toplap termination is seen, majority of the layers are subparallel to the 14At1 boundary.	pp. 44
Figure 5.6	The yellow arrow indicates downlap onto 14At1 with sediment movement from east to west. The strata truncate on to the older horizon (14At1).	pp. 44
Figure 5.7	Figure 5.7: Yellow arrow shows downlap truncating on the 15At1 horizon, followed by red arrow showing toplap getting truncated by the 16At1 horizon. The downlap occurs during the Cenomanian age and the toplap occurs below the Coniacian age.	pp. 45
Figure 5.8	Gamma ray (GR) log patterns linked to sediment supply and sedimentary facies (Radwan, 2021).	pp. 49
Figure 5.9	The gamma ray log from BUSM to 1At1 and 1At1 to 6At1 showing a repetitive coarsening upward patterning. This is known as funnel shape. From left to right, the figure shows the FO-1, FR-1, and FS-1 wells which are oriented NNW-SSE.	pp. 49
Figure 5.10	From 6At1(Hauterivian) to 13At1 (Aptian) showing a general trend of fining upward, which is a bell shape.	pp. 49
Figure 5.11	Patterns from 14At1 (annotated as horizon 2) to 16At1 (Coniacian aged) display a cylindrical gamma ray pattern, whereby there is neither coarsening to fining upward of lithology.	pp. 50
Figure 5.12	From 16At1 (Coniacian age) to 16Bt1 (Santonian age), the gamma ray pattern displays a symmetrical shape, whereby there is initial fining upward of sequence followed by coarsening upward of sequence within one interval.	pp. 50
Figure 5.13	Gamma ray log patterns (GR, red lines) in wells FO-1, FR-1 and FS-1 indicating prograding (upward coarsening), retrograding (upward fining) and aggradation sediment supply. This is supported by the logged rock types.	pp. 50
Figure 6.1	Ant-tracking with different filters and attributes applied to TWT 1257. a) Smoothing was applied to the variance slice prior to the ant-track algorithm applied, this attenuated the faults to a point where they nearly disappear. b) Ant-track algorithm without smoothing but with the passive filter applied to it. The red line represents faults that have been picked. c) Ant-track algorithm without smoothing, but with an aggressive filter applied to it. The aggressive	pp. 54

	filter shows more faults and hence the several red lines are marked. d) Ant-track algorithm showing the tracked faults intersecting this time slice. The general trend is west-southwest to east-northeast.	
Figure 6.2	Horizons 16At1 and 13At1 and intersecting faults. The colors represent the dip angle. Two phases of faulting are seen below horizon 13At1 and above 16At1, with limited faulting between these horizons.	pp. 55
Figure 6.3	First phase of faulting below the Aptian age 13At1 horizon, with the dominant faulting trending E-W.	pp. 55
Figure 6.4	Second phase of faulting above the Santonian aged 16At1 horizon, mainly with faults trending N-S forming grabens, and those trending E-W being parallel to one another.	pp. 56
Figure 6.5	Mapped faults in the study area, with two seismic sections with the chaos attribute applied? The first phase of faulting below horizon 13At1 shows faults with dips ranging from 20° to 50°. These faults have a higher dip towards the top and become shallower towards the bottom of the faults, thus exhibiting a listric fault pattern. The second phase of faulting above horizon 16At1 has dips greater than 55°, with N-S faults exhibiting a horst and graben pattern.	pp. 57
Figure 7.1	Time slices with the envelop attribute applied: a) 2134 sec TWT time slice with pockmark shown (red arrow) with a diameter of 860m. b) 1252 sec TWT time slice pockmarks trending NE-SW (red ellipse) varying from 400m to 900m in diameter. The second pockmark further north has a diameter of 750m (red arrow).	pp. 61
Figure 7.2	Time slice at 2134 sec TWT with dip ratio applied. The pockmark in the southwest (red arrow) is evident, with a diameter of 860m. The diameter of the pockmark is shown by the high dip ratio (white), and the center of the diameter highlighted by the low dip ratio.	pp. 61
Figure 7.3	a) Seismic section (crossline 482) showing strata that have been disturbed by a vertical structure (red rectangle) which terminates at 16At1 (seismic line below red rectangle). This disturbance propagates from the Aptian age 13At1. b) Chaos attribute applied; c) Variance attribute applied. The feature is clearer, as there is less noise in the background. d) Envelope attribute does not highlight the vertical feature but rather the strata which are disrupted on either side of the structure.	pp. 62
Figure 7.4	Horizon 15At1 with edge detection attribute applied. The black circles indicate the gas escape features seen in Figure 7.1b on time slice 1252. These features form circular structures on surface, with the exception of the left most black circle, which indicates an oblate shape.	pp. 63
Figure 7.5	Inline seismic section 2564 showing the undulating channel with the green line. The purple line above it presents the channel top. The red lines represent faults which bound the faults on either side.	pp. 63
Figure 7.6	Time slice at 1650 sec TWT, with a) dip illumination attribute applied which highlights the sub-circular channel (black circle), with the highest dip ratio at the edges of the channel; b) envelope attribute applied which illustrates the same sub-circular feature, being more pronounced on the northern side by the partial half circular bright spots (red and yellow), and possible channels that	pp. 64

	are slightly sinuous and parallel shown in the red arrow. The green arrows indicate the north direction.	
--	--	--

### Table of Tables

Table 4-1.	Major formation tops in the study area, including p-wave seismic velocity, density, age, and sediments found within each layer. These were used to calculate the reflection coefficient of each layer.	pp. 31
Table 4-2.	Wavelength of faults and detection limits.	pp. 32
Table 4-3.	Summary of the Chaos attribute parameters that were used in this study.	pp. 35
Table 4-4.	Ant-track parameters used in this study in PETREL 2018 Schlumberger software	pp. 38
Table 5-1.	Summary of the lithologies assigned using gamma ray (density) and seismic velocity values using the process of artificial neural networks.	pp. 40

### Table of Equations

Equation 1: Reflection coefficient	$Rc = \frac{\rho_2 V_2 - \rho_1 V_1}{\rho_2 V_2 + \rho_1 V_1}$	pp. 13
Equation 2: Convolution	$(S(t) = R(t) * W(t))$	pp. 15
Equation 3: Vertical Resolution	$v = f / (\lambda)$	pp. 16

Equation 4: Fresnel Zone	$Fr = \frac{v TWT}{f} \frac{1}{2}$	pp. 16
Equation 5: Dip Magnitude	$dip\ magnitude = \sqrt{\left(\frac{d}{dx}\right)^2 + \left(\frac{d}{dy}\right)^2}$	pp. 19
Equation 6: Dip Azimuth	$dip\ azimuth = \arctan\left(\frac{dt/dy}{dt/dx}\right)$	pp. 19
Equation 7: Trace Envelope	$(A(t) = \sqrt{x^2(t) + y^2(t)})$	pp. 19
Equation 8: Curvature	$(z(x, y) = ax^2 + by^2 + cxy + dx + ey + f)$	pp. 20
Equation 9: Chaos	$(J = 2\lambda_2 - 1)$ $\lambda_1 + \lambda_3$	pp. 21

# 1. INTRODUCTION

---

## 1.1 INTRODUCTION

The Bredasdorp Basin has been explored for hydrocarbons. The initial exploration was done in 1987 and concentrated on gas fairway along the northern flank of the basin (Van Wyk, 1989). It was discovered that the Aptian aged upper shallow marine sandstones were a quality reservoir in a trapping situation (Van der Spuy, 2003). The significant porosity and permeability of this sandstone heralded the Moss gas development project which focused on gas and condensate production via the F-A platform in 1992. Since then, over 200 boreholes have been drilled and burial studies have shown potential maturity over large areas of the Bredasdorp Basin to have generated and expelled oil (Roux, 1997). Furthermore, multichannel reflection seismic studies and a variety of geology disciplines (paleontology, geomechanics, petrography and geochemistry) have been utilized to explore the basin's potential for hydrocarbons. Through these various disciplines, TOTAL has been able to make a large gas discovery in the Brulpadda region, which is located between the Southern Outeniqua and Bredasdorp Basins. The region is estimated to contain approximately one-billion-barrel oil equivalent (BOE) (EPCM Holdings, 2019). Given the proximity of the gas discovery to the chosen study area, this project aims to delineate structures and stratigraphical successions that will benefit the understanding of how gas is trapped within the studied sequences and in turn delineate the possibility of the study area hosting hydrocarbons. This will be done through the reviewing of available literature in conjunction with the interpretation of seismic data.

The breakup of West Gondwana heralded the formation of rift basins along the southern tip of Africa during the late Jurassic to the early Cretaceous (Dingle and Scrutton, 1974). The breakup resulted in the formation of rift basins within the intracratonic Outeniqua Basin, which were later structurally modified by dextral shear stress along the Agulhas Falkland Fracture Zone (AFFZ) (Figure 1) (Roux, 1997). The Outeniqua Basin comprises five sub-basins, four are along the coast of southern Africa, and all these basins converge into the fifth sub-basin further to the south, named the Southern Outeniqua Basin (Figure 2) (Ramiah et al., 2018). The western basin, known as the Bredasdorp Basin, is the focus of this study. This basin trends NW-SE covers an area of 18 000 km<sup>2</sup> and is filled with upper Jurassic and lower Cretaceous synrift continental and marine strata, as well as post Cretaceous and Cenozoic divergent rocks (Van der Spuy, 2003). The Bredasdorp Basin is bound by basement high arches, namely the Infanta arch on the east and Agulhas arch on the west. The basement highs are composed of Ordovician to Devonian metamorphic sediments of the Cape Supergroup and follow the NW-SE structural grain of the Cape fold belt (Davies, 1997).

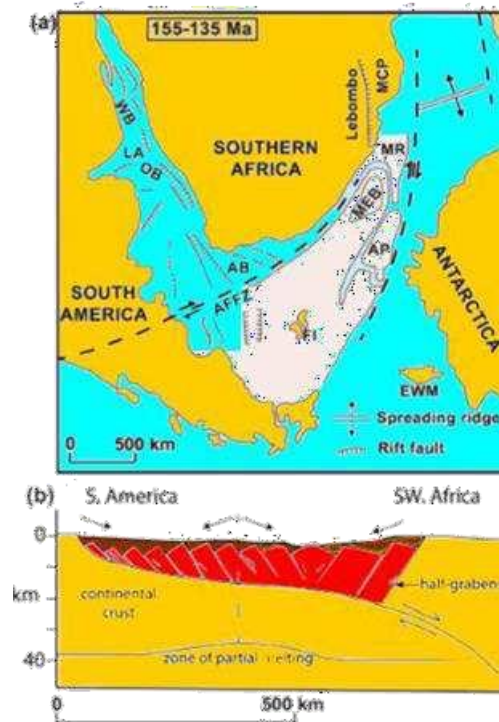


Figure 1.1: a) The split of West Gondwanaland, which included Africa, Antarctica, and South America, between 155 and 135 MA. b) The split between South America and Southwest Africa which caused the creation of half-grabens. The Agulhas Falkland Fracture Zone (AFFZ), also known as the dextral shear fracture zone, is situated south of Africa. Modified after Mahlalela (2018).

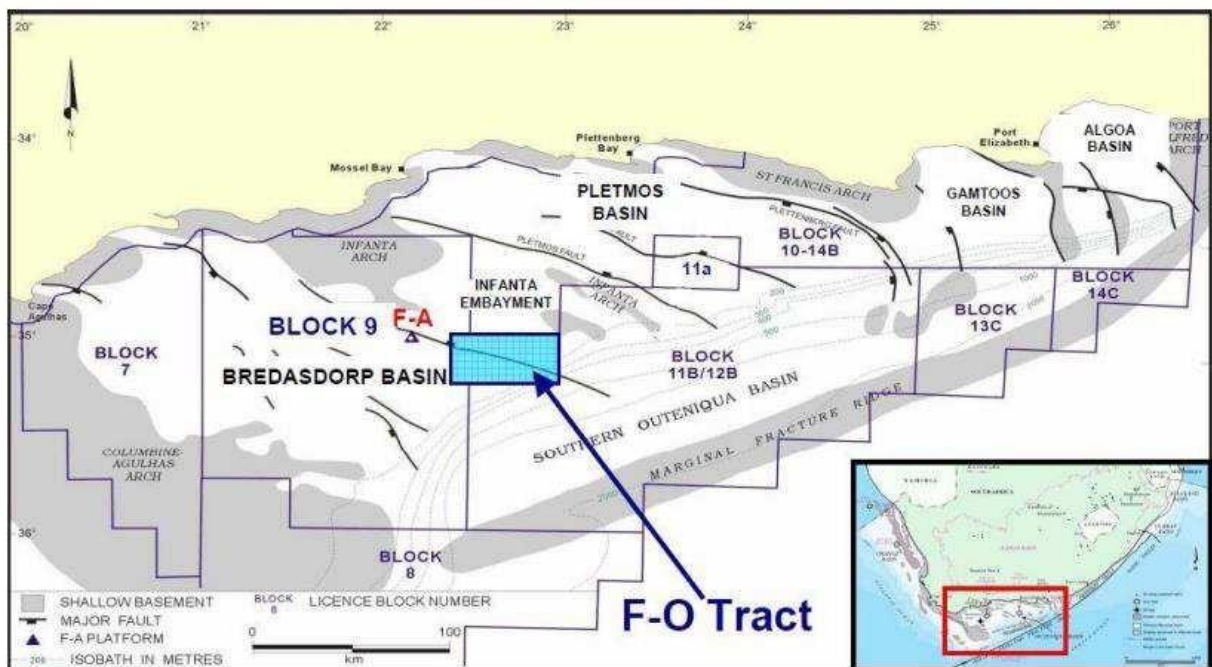


Figure 1.2: The Outeniqua Basin, a group of five rift basins with accompanying basement highs, off the coast of South Africa. The Infanta Arch on the east and Agulhas Arch on the west which are basement highs, define the Bredasdorp Basin, situated on the westernmost side. Study site is specifically in the field of operations (Petroleum Agency SA 2013).

Over the past decades, seismic technology has proved to be useful in mapping subsurface geology which

in turn can be used to explore for potential hydrocarbons or various other commodities. Seismic data have long been used for lithologic prediction and for imaging of depositional elements (Posamentier, 2004). 2D reflection seismic data are useful for interpreting seismic sequence stratigraphy whilst 3D reflection seismic data are used to analyze seismic geomorphology. These are useful in the identification of stratigraphic traps and the prediction of lithologies (Posamentier, 2004). Additionally, 3D seismic data can provide improved signal-to-noise ratio and avoids aliasing of faults and structures. This allows for clearer imaging of shallow and deep-seated depositional systems, which can assist in developing useful targets for hydrocarbons (Davies et al, 2004). In the past and less so in the present, 2D seismic data were and still are useful for the purpose of hydrocarbon exploration and identifying possible structures. The decision to use 2D or 3D seismics is based on a cost/benefit analysis. In general, 2D seismic is acquired in frontier areas because it is cheaper, and the hydrocarbon province is not proven yet.

The seismic interpretation of structures and depositional elements can assist in understanding the development of the source rock, the migration of fluids and gases, the impact of igneous bodies on source maturation, as well as traps for hydrocarbons. Igneous bodies play a vital role in the migration and maturation of hydrocarbons. Additionally, the mapping of faults on the seismic data can help determine if there is ingress of fresh oxygenated water and help understand gas migration pathways (Davies, 1997). Seismic sequence stratigraphy can be used to determine the extent of the source rock as well as the sequences, which in turn can help determine periods of sediment starvation and deposition of organic matter (Bearnish, 1989). The sequence stratigraphy work conducted in the Bredasdorp Basin suggests that post transgression and early highstand deep marine sediments have greater organic matter content, yielding higher potential for oil and gas source rocks.

## **1.2 AIMS AND OBJECTIVES**

### **Aims**

The following aims will be achieved using 3D seismic reflection data:

- Understand the tectonic development of the Bredasdorp Basin and where the gas is trapped.
- Draw conclusions about Bredasdorp Basin's oil/gas capacity.

### **Objectives**

The aims of the project will be obtained by:

- Acquiring well data and seismic data from PetroSA and import it into PETREL 2018 Schlumberger 2018 Interpretation Software.
- Pick seismic horizons on the seismic data and constrain the interpretation with the well data.
- Find structures using seismic attributes and examine whether these structures host or have any effect on oil and gas migration and accumulation.

## 1.2 RESEARCH QUESTIONS

The questions that the project aims to answer are as follows:

- Given the proximity of the recent TOTAL gas discovery, how plausible is it that the proposed study area contains hydrocarbons and if so, what are the quantities.
- What is the relationship between tectonics and hydrocarbon migration?
- Which attributes are best to apply when working with hydrocarbons, and which attributes are impeccably effective in identifying small scale structural and stratigraphic features?

## 1.3 LAYOUT OF THESIS

The layout of the thesis is outlined below:

Chapter 1 introduces the location of the study area. It also lays out the research aims and objectives, as well as the layout of the thesis.

Chapter 2 outlines the background geology and history of the tectonism and sedimentation of the rift basin, as well as previous studies done on the accumulation of the hydrocarbons.

Chapter 3 discusses seismic data and its limitation, and relevant equations are discussed. In addition, an overview on the theory of various horizon and volume attributes is given and their uses in seismic interpretation.

Chapter 4 outlines the methods used in the study in detail. The data is initially subjected to seismic well ties. Thereafter, the methodology is divided into stratigraphic interpretation and structural interpretation. The stratigraphic interpretation includes well logs and artificial neural network (ANN). The structural interpretation includes horizon and fault picking, data conditioning and application of attributes.

Chapter 5 summarizes the results of stratal patterns found in the seismic sections, such as toplap, downlap and onlap patterns. It also addresses the summary of the lithology graph produced using gamma ray log and porosity log in the ANN algorithm and the well log correlation patterns that address progradation, retrogradation and aggradation.

Chapter 6 discusses the application of ant-tracking and other attributes in relation to the structural framework. It also summarizes the formation of the patterns found within the faults and their implications on the tectonic evolution of the basin.

Chapter 7 addresses the results that correlate with evidence of hydrocarbon migration and plays. It also discusses the use of attributes to highlight features such as pockmarks and fluid escape structures, which are synonymous with hydrocarbons migration.

Chapter 8 summarizes the implication of these results in terms of the tectonic evolution of basin.

Chapter 9, concluding remarks are made regarding the useful attributes and optimizing their parameters. The chapter summarizes all the findings of the study and future recommendations or shortfalls of the results.

## **2. GEOLOGICAL BACKGROUND**

### **2.1 PRE-RIFT GEOLOGY**

Prior to the breakup of Gondwana, the Cape Supergroup, comprising lithologies ranging from Ordovician (500-410 Ma) to late Devonian (380 Ma), were deposited on the Proterozoic crust surrounding the southern perimeter of the Kaapvaal craton (Davies, 1997). Between the Carboniferous (290-278 Ma) and late Triassic (230 Ma) periods, these sediments were overlain by the Karoo Supergroup sediments which included tillites, claystone, sandstones, extrusives and intrusives (Barnett et al., 1997).

During Karoo deposition, the Cape Orogeny took place and initiated when the Pacific plate was obliquely subducted below the Gondwana landmass, resulted in folding and faulting of the Cape Supergroup sandstones and shales and the southern Karoo Supergroup sediments (Dingle, 1974; Davies, 1997). The faulted folds predominantly trend east-west along the south-coast of South Africa and northwest southeast along the southwest coast. These structural architectures served as the structural grain for the present-day basins in the southern Cape (Barnett et al., 1997; Johnston, 2002).

The Outeniqua Basin formed as the Gondwana Basin broke up. According to Dingle (1974), the basin is an epicontinental feature that formed along pre-existing weakness in the continental crust. The basin is believed to be intermontane in nature, with detritus being derived from the southern Cape and Falkland Plateau areas. The Falkland Plateau was situated off the southeast coast of South Africa before Gondwana breakup. Initially, the deposition of the detritus was on the continental crust, but later, sediments spilled over into the oceanic areas.

### **2.2 SYN-RIFT**

The breakup of Gondwana around 180 Ma was heralded by the eruption of basalts and rhyolites resulting in the opening of a premature ocean that developed into the Indian ocean and the production of two individual landmasses, East Gondwana (South America, Africa, and Falklands) and West Gondwana (India, Madagascar, Seychelles, Antarctica, and Australia) (Figure 2.1) (Cox, 1992; Storey, 1995; Fitzgerald, 2002; Lawver et al., 1992). This breakup was driven by extension along the Mozambique-Zimbabwe border was initiated by the Karoo mantle plume, which resulted in the generation of major fractures in the crust (Storey, 1995; Hashim, 2015). The first continental syn-rift sediments which included fluvial and lacustrine deposits were deposited in the Outeniqua rifts. Additionally, a seaway transgressing south with time developed along the eastern margin of Africa and introduced marine conditions to the Outeniqua Basin (Norton and Sclater, 1979).

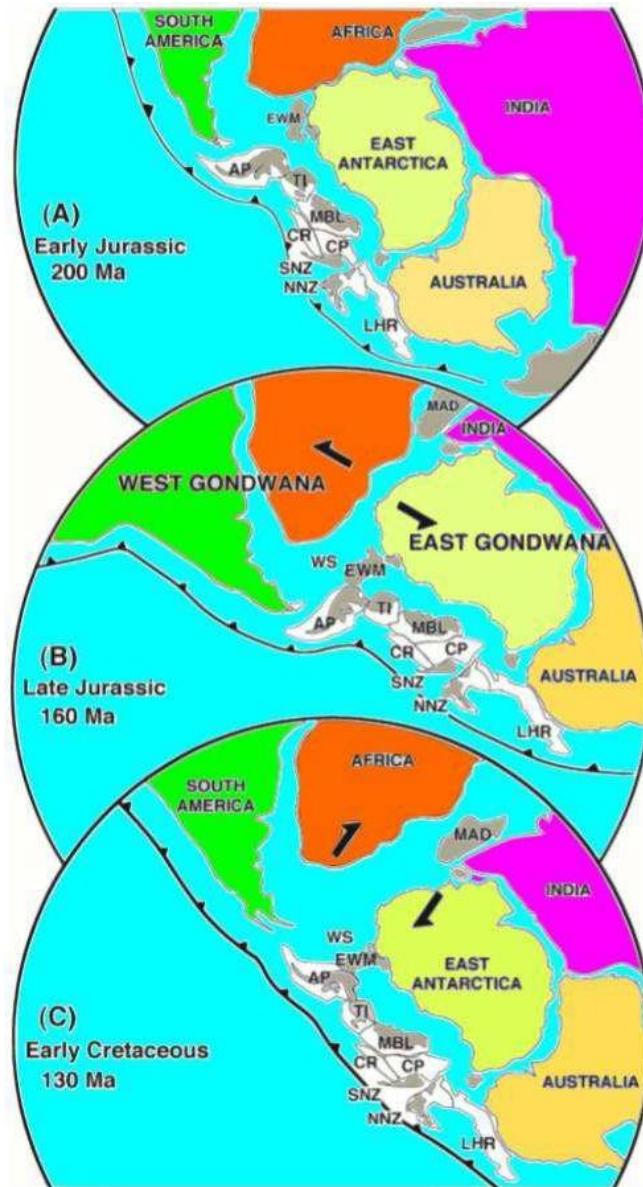


Figure 2.1: a) The reconstruction of Gondwana and the respective paleopositions of the continents in the early Jurassic (200 Ma). b) The continents are pulled apart as seen at 160 Ma, c) Early Cretaceous (130 Ma) dextral shear movement was then seen (Fitzgerald, 2012). Labels: AP, Antarctic Peninsula; TI, Thurston Island; MBL, Marie Byrd Land; CR, Chatham Rise; CP, Campbell Plateau; SNZ, southern New Zealand; NNZ, northern New Zealand; LHR, Lord Howe Rise; WS, Weddell Sea.

A series of horsts and grabens bounded by normal faults formed due to the breakup of Africa and the Antarctic in the Jurassic (180-160 Ma). The grabens form principal areas of depositions which are

divided into four en-echelon basins separated by the horsts comprising the basement meta-sediments of the Cape Supergroup (Ramiah et al., 2018). The faults bounding the horsts and grabens formed along the structural grain produced by the Permo-Triassic (255 Ma) Cape Fold Belt (Brown et al., 1995). The structures of the basins were evolved by the periodic movement of the Agulhas Falkland Fracture Zone during the Early Cretaceous (130 Ma) and inversions tectonics resulted from this event (Ramiah et al., 2018).

Rifting between South America and Africa between 130 and 120 Ma resulted in a large continental slab being detached from the south-eastern tip of Africa, which later became known as the Falkland Plateau (Hashim, 2018). This movement resulted in the creation of fractures in the oceanic crust which form part of the Agulhas – Falkland Fracture Zone (AFFZ) that truncates the Outeniqua Basin in the southeast (Dingle, 1974; Thomas et al., 1993). As Falkland Plateau separated from the eastern side of Africa, specifically along the Mozambique ridge, dextral shear stress was exerted along the AFFZ (Brown et al., 1995; Roux, 1997). Furthermore, the establishment of these fractures facilitated the formation of new ocean basins and enlargement of older adjacent ones (Dingle, 1974). According to Martin et al (1982), Davies (1997) and Johnston (2000), the mechanism of separation between southern Africa and the Falkland Plateau has been speculated to either be rotational or pull-apart. Most of the evidence supports a pull-apart mechanism, with a restricted marine basin developing between western Antarctica and the Falkland Plateau. This is supported by pre-rift structures correlating to those on the African craton which can be seen on seismic data acquired offshore from the Falkland Plateau without rotating the islands (Davies, 1997). These basins formed during the late Jurassic would become the deposition sites for syn-rift sedimentation.

### **2.3 DRIFT AND POST-RIFT**

The drift phase began at approximately 126 Ma during the Valanginian (Davies, 1997). This phase was accompanied by uplift and extensional erosion (Brown et al., 1995), as well as slow movement along the faults for 5 to 8 million years, resulting in the first major angular unconformity, horizon 1At1 in the Outeniqua Basin (Figure 4) (Davies, 1997; McMillan et al., 1997). As a result of the uplift, principal deposition was restricted to the basins, which increased the subsidence rates of the basins (Brown et al., 1995). Overlying the unconformity are shales interbedded with basin floor turbiditic sandstones deposited post thermal subsidence. The prevailing deposition environments were transgressive and marine conditions (Brown et al., 1995; Akinlua et al., 2014). The end of the Hauterivian (121-117 Ma) saw another tectonic event of uplift and intense erosion mainly along the margins of the divergent basins. This event coincided with major regression which is marked as seismic horizon 5At1 (Figure 2.2) (Davies, 1997; McMillan et al., 1997). The high subsidence rates ceased from the Barremian to early Aptian, due to reduced thermal decay caused by transpressional stress along the AFFZ. However, marine sedimentation persisted, and the circulation was restricted during early to mid-Cretaceous due

to the proximity of the Falkland Plateau to the southern Africa tip (Davies, 1997). Limited circulation resulted in depletion of oxygen, causing the development of anoxic conditions which better preserve organic material.

During the early Aptian, at approximately 125 Ma, improvement of oceanic circulation is attributable to the rift opening further and extension of the open marine conditions between Falkland and Africa. Brown et al (1995) stipulate that the final stage of separation between Falkland Plateau and South Africa, permanently connecting the oceans adjacent to the African plate (Indian and Atlantic Ocean)

allowed thermally driven subsidence rates to increase. The cyclicity of thermal subsidence followed by uplift and erosion continued throughout the Cretaceous era, resulting in widespread erosive type 1 unconformities i.e., seismic horizons, namely, 5At1 (Hauterivian), 13At1 (Aptian) and 15At1 (Turonian) (Figure 2.2). In addition, deep marine sediments deposited during transgressive and early highstand phases have high organic carbon content which makes them good source intervals, e.g., Aptian aged 13A sequence. The sequence from Hauterivian age to the K-T boundary (60 Ma) is mainly progradational, then transitions into aggradational in the Cenozoic era (Davies, 1997). Several source rock intervals are mapped between 1At1 and 15At1, and oil and/or gas has the organic at the 1A, 13A, and 14A sequences (Figure 2.2).

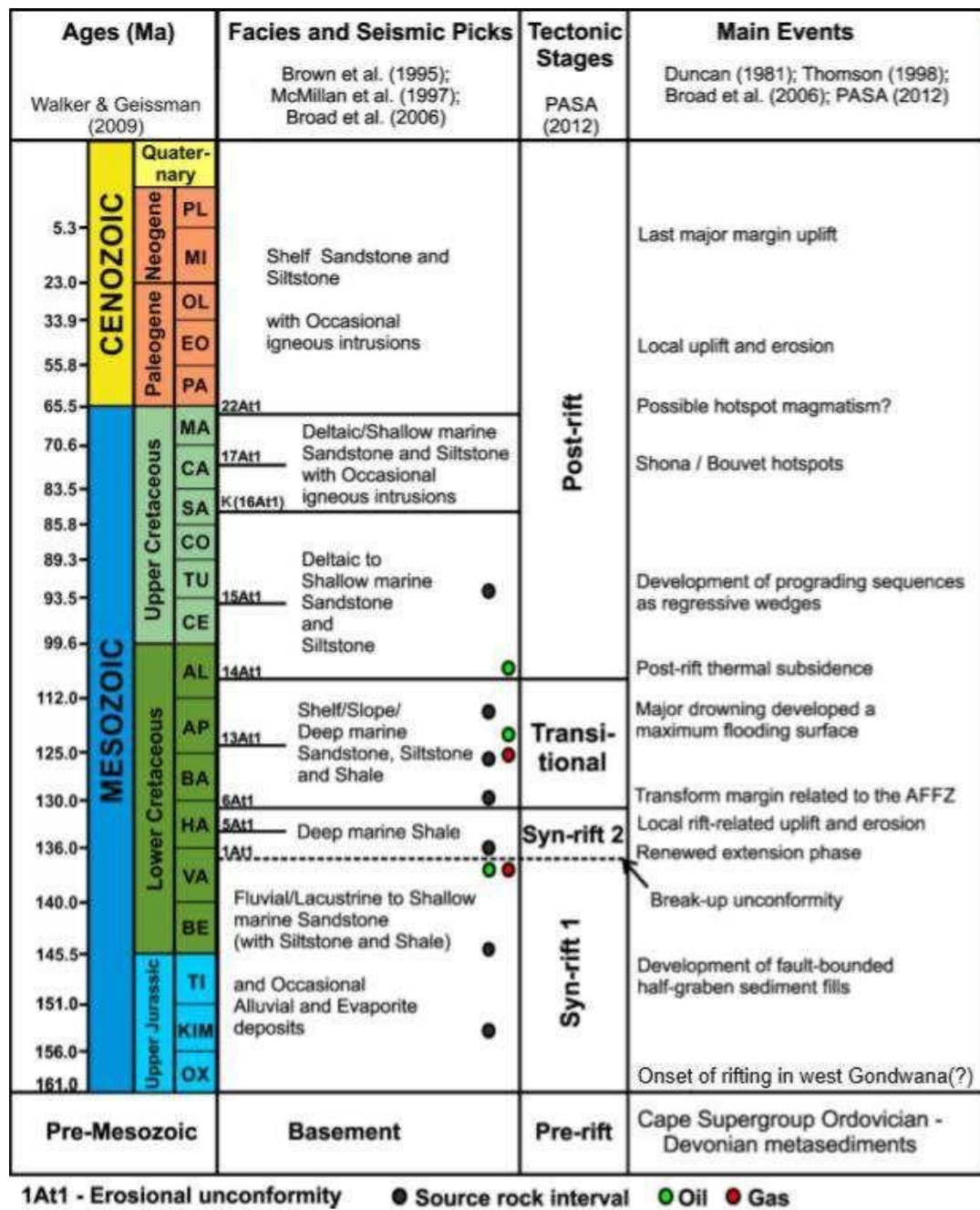


Figure 2.2: Bredasdorp Basin chronostratigraphic column showing different seismic horizons labelled 1At, 5At1, 13At1, etc., which indicate type 1 erosive unconformities. The cyclical thermal subsidence, followed by uplift and erosion, is indicated by these seismic horizons (Sonibare et al, 2018). Indicated on the diagram as black, green, and red circles, respectively, are several source rock intervals as well as oil and gas.

## 2.4 DEPOSITION OF SOURCE ROCK AND MATURATION

Over 200 exploration and appraisal boreholes have been drilled in the Bredasdorp Basin to assist in delineating seismic sequence stratigraphy of the Aptian sequence 13A (Winters et al., 1993; Van der Spuy, 2003). The sequence has source rock intervals and a quality sandstones reservoir. However, this source rock is not limited to the Aptian sequence only, but rather extends from the late Valanginian age, with the presence of wet gas and oil prone shales. The deposition periods and conditions play a vital role in the hydrocarbon plays. According to Bearmish (1989), Winters et al (1993) and Akinlua et al (2014), these regions of deposition are mainly lowstand turbidity tract systems.

Various studies have shown that that the source rock is mainly type II kerogen with type I component, which has implications for the origin of the organic matter (Figure 2.3). The organic material for the hydrocarbons is fossilized plankton and algae matter derived from a marine environment, with a mixture of terrestrial plant material and is responsible for the generation of oil (Akinlua et al., 2014). Restricted circulation during early to mid-Cretaceous allowed for development of anoxic conditions which assisted in the preservation of organic material thus yielding organic rich source intervals (Davies, 1997).

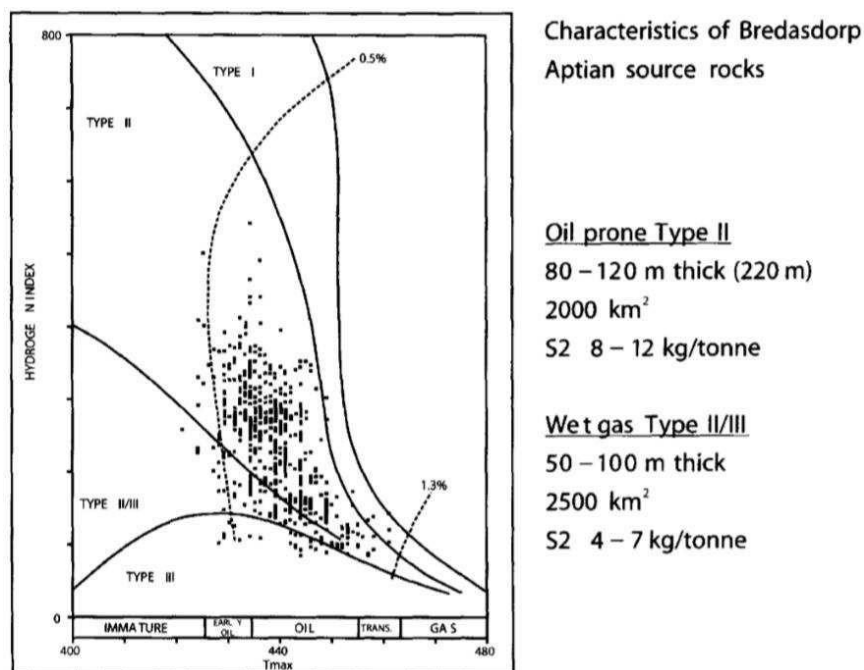


Figure 2.3: Hydrogen Index (HI) vs Tmax plot for the Bredasdorp Basin which shows that the oil and gas are both type II indicating the origin of the organic material to be that of marine (Van der Spuy, 2003).

The introduction of large quantities of fresh water in marine environments owing to greater precipitation and higher surface runoff led to density stratification in the deep Bredasdorp basin (Davies, 1997). This resulted in anoxicity and density stratification which are the conditions conducive for source rock

formation as seen in Angola and Namibia. The anoxic conditions coupled with periods of regional sediment starvation resulted in the deposition of organic rich claystones (Davies, 1997; Akinlua et al., 2014).

The maturation of the Aptian sequence and older formations is affected by several factors such as early burial, hotspot transit and a hydrothermal event (Ramiah et al., 2018). In terms of the burial, the pressures imposed on the sequences were found to exceed 3000 psi above hydrostatic. Furthermore, Akinlua et al (2014) used burial studies to show that the early Aptian generated and expelled oil, owing to sufficient maturation of large areas.

Generally, the distribution of potential hydrocarbons shows a trend which is parallel to the long axis of the basin (Figure 2.4). The hydrocarbons range from the early oil window to gas window, and each is distributed uniquely, with its own rock evaluation value (Van der Spuy, 2003). The potentially oil-prone source rock has an area of 2000 km<sup>2</sup> in the central part of the basin and has a rock evaluation pyrolysis S<sub>2</sub> value of 8-12 kg HC/t. These oil-bearing areas are surrounded by gas prone source rocks which have an area of 2500 km<sup>2</sup>, with a rock evaluation pyrolysis S<sub>2</sub> value of 4-7 kg HC/t (Van der Spuy, 2003).

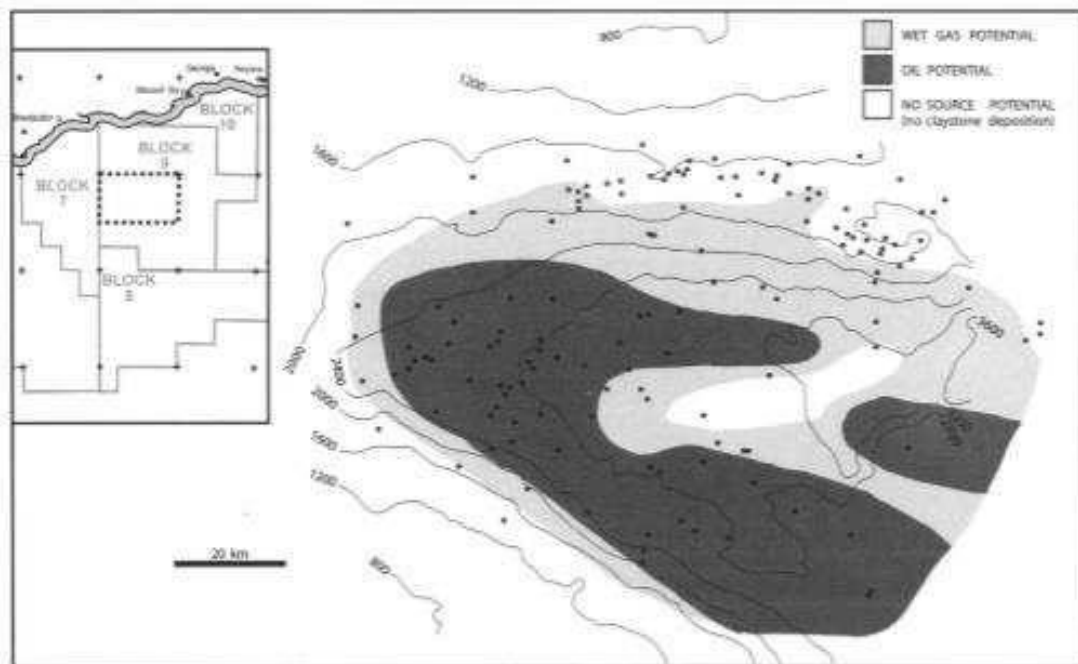


Figure 2.4 Oil and wet gas potential throughout the Bredasdorp Basin. The gas surrounds the oil, which is concentrated in the basin's center (Van der Spuy, 2003).

### 3. SEISMIC REFLECTION THEORY AND WELL LOGS

#### 3.1 SEISMIC ACQUISITION

In the process of acquiring seismic reflection data, an energy source and receivers are used. A shock wave is generated by an energy source (e.g., vibrosis, airgun, and sledgehammer) on the surface, to

pass downward toward the subsurface strata (Evans, 1997). Some of the shock waves are reflected from the rocks back to the surface due to lithological and structural boundaries where there is a change in physical properties of the rocks (Evans, 1997; Dentith and Mudge, 2014). This physical property is known as acoustic impedance and it is the product of P-wave velocity ( $V_p$ ) and density ( $\rho$ ) (Talagapu, 2005; Dentith and Mudge, 2014). The contrast of acoustic impedance, coupled with the reflection coefficient, as well as the dimension and geometry of the targets will determine if a boundary generates strong reflection (Malehmir et al., 2013; Manzi et al., 2019). The normal incident Reflection Coefficient  $R$  between two velocity layers is expressed as:

$$R_c = \frac{\rho_2 V_2 - \rho_1 V_1}{\rho_2 V_2 + \rho_1 V_1}$$

Equation 1

where  $\rho$  denotes density and  $V$  denotes velocity. Generally, the reflection coefficient - which is also dependent on the angle of incident- in the geological environment is usually around 0.2. However, a reflection is recognized when the contrast in acoustic impedance produces a reflection coefficient of approximately 0.6. The energy that is not reflected is transmitted. Thus, a large reflection coefficient will result in less transmitted energy and the reducing of the signal-to-noise ratio (Evans, 1997; Talagapu, 2005). This in turn will have an effect on the increase and decrease of amplitude, which can be a good indicator of hydrocarbons.

In marine surveys, one or more energy sources fastened parallel to one or more receiver lines are towed by a moving ship (Figure 3.1). The receiver line is a cable known as a streamer and contains several hydrophones (Evans, 1997; Talagapu, 2005). The source is an impulsive energy i.e., airgun, as opposed to vibrator sources which would result in the creation of gas bubbles and thus noise in the seismic trace. A pulse of compressed air is released into the water from an array of airguns. These airguns are fired at slightly different times to control frequency and energy of wavelet and counteract the cyclic effect of the expansion and collapse of gas bubbles (Evans, 1997; Dentith and Mudge, 2014).

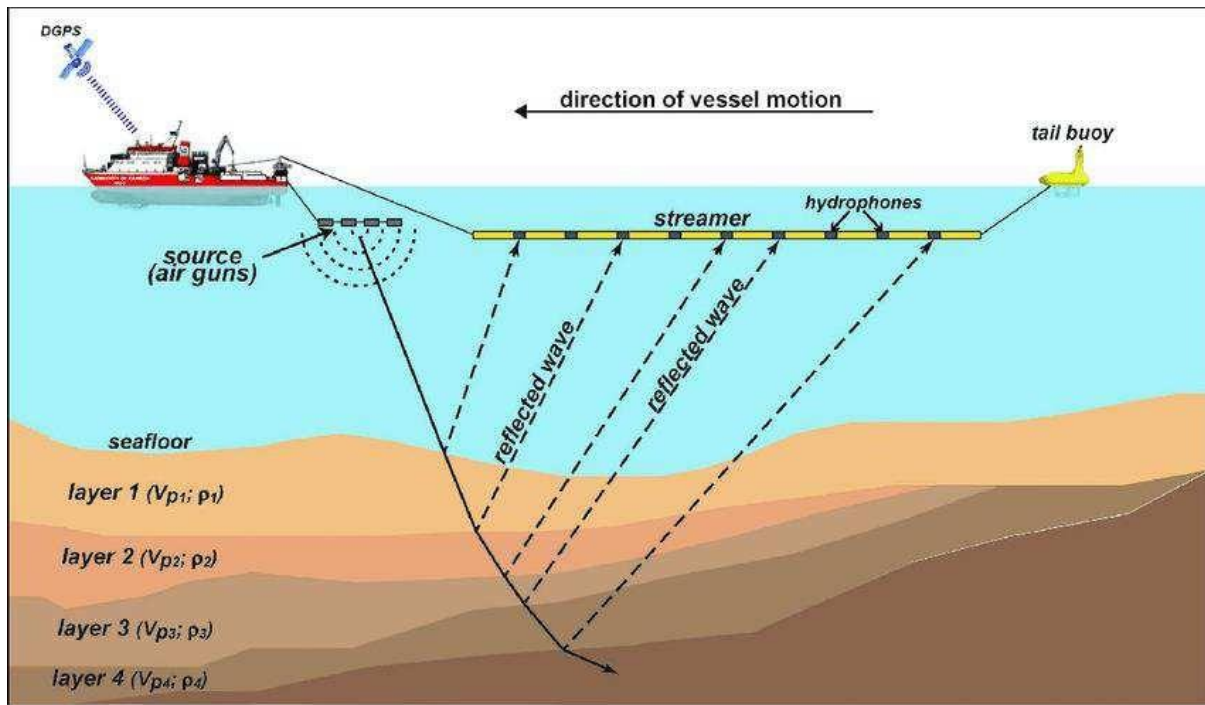


Figure 3.1: Schematic illustration of seismic survey vessel, with the source (airgun) and resultant raypaths reflected at different interfaces (changes in acoustic impedance). The streamer with hydrophones attached to it receives the reflected energy from different boundaries (Cameselle, 2016).

A single streamer and source would result in a single seismic profile. Several parallel sources and streamers would result in several parallel lines recorded at the same time. This has implications for 3D marine surveys as closely spaced parallel lines are recorded to achieve the production of 3D seismic data (Talagapu, 2005).

### 3.2 SEISMIC PROCESSING

The purpose of seismic processing is to convert field recorded seismic data to a form which can be used for geological interpretation. The seismic data recorded in the field contain reflections, coherent noise, and random ambient noise (Talagapu, 2005). Reflections are recognized as travel times whilst coherent noise includes reflections from near surface structures, and random noise is attributed to near surface irregularities or forces of nature such as wind. To extract useful information from the data, some aspects of the coherent and random noise are suppressed to uncover genuine reflections (Lines and Newrick, 2004).

By enunciating the true reflections and processing the seismic data, the signal-to-noise ratio is enhanced, seismic impulse is removed from the seismic trace through inverse filtering and reflectors are repositioned to their true locations thus making the data more palatable (Yilmaz, 2001; Talagapu, 2005).

There are three primary steps which are of paramount importance in seismic processing, and these are deconvolution, velocity analysis and migration. Secondary steps such as pre-processing, common midpoint (CMP) sorting, dip-Moveout (DMO) and stacking, assist in improving the effectiveness of the primary steps. Mathematically, the relationship between the source and the investigated structure is known as convolution (Lines and Newrick, 2004; Talagupu, 2005). This is represented as a seismograph ( $S(t)$ ):

$$S(t) = R(t) * W(t)$$

Equation 2

where  $W(t)$  is the initial wave radiating from the seismic source known as a wavelet and  $R(t)$  is the reflectivity function, which describes the subsurface influence on the wavelets (Talagupu, 2005). The process of deconvolution looks at extracting the reflectivity function  $R(t)$  by compressing the basic wavelet in the recorded seismograph, thus reducing reverberations (Yilmaz, 2001). This results in increased temporal resolution and higher visibility of subsurface structures (Talagupu, 2005; Dentith and Mudge, 2014).

The second primary step, velocity analysis, includes stacking and normal move out (NMO) correction. The NMO results from the variation in time taken for a seismic wave from a source to reflect off a horizon and reach a receiver, as the distance between the source and receiver is changed. Namely, the time will increase as the offset between the source and receiver increases (Sheriff, 2002; Lines and Newrick, 2004; Dentith and Mudge, 2014). This is done through common midpoint (CMP) gathers which is the common midpoint from a collection of seismic traces. By summing these common reflection points through a process known as stacking, the effect of random noise is reduced, and the signal-to-noise ratio increased (Yilmaz, 2001). The final primary step, migration, is a process wherein attempts are made to correct the directions and true subsurface positions of the geological structures in the seismic sections (Herron, 2011; Dentith and Mudge, 2014). This is done through the redistribution of energy to ensure that geological structures are better imaged.

### 3.3 SEISMIC RESOLUTION LIMIT

Seismic resolution describes how two reflections that are close together can be clearly defined. It is vital for extracting stratigraphic and structural information from seismic data (Chopra et al, 2006). Seismic resolution comprises two aspects derived from the seismic datum, namely, the temporal domain (also known as vertical resolution) and the spatial domain (also referred to as the lateral resolution) (Chopra et al., 2006; Herron, 2011). Both these aspects use the Nyquist Theorem, which describes how increasing the resolving power of the seismic data enables finer detailed interpretation of the subsurface geology (Herron, 2011). Additionally, it describes how resolution is dependent on signal wavelength,

which adversely depends on frequency of the seismic pulse and seismic velocity (Malehmir et al., 2013; Manzi et al., 2019).

Vertical resolution is the minimum distance at which two seismic events at different depth levels can be distinguished from one another (Chopra et al., 2006). The tuning thickness of the data which relates velocity, frequency, and wavelength determines whether the reflection will be discreet or discernible. Given the formula:

$$v = f/(\lambda)$$

Equation 3

where  $v$ ,  $\lambda$  and  $f$  represent velocity, wavelength, and frequency (specifically the dominant frequency), respectively. Raleigh limit of vertical resolution for a discernible reflector is  $\lambda/4$  (Lines and Newrick, 2004; Yilmaz, 2001; Herron, 2011). However, the Widess model suggests that in the case where there is high signal-to-noise ratio, the vertical resolution limit is  $\lambda/8$ , as it is difficult to separate reflection points below this limit (Yilmaz, 2001; Chopra et al, 2006). By reducing the wavelength and increasing the frequency through the process of deconvolution, vertical resolution can be improved (Lines and Newrick, 2004; Yilmaz, 2001). This being the case, earth filtering has to be considered as it directly impacts seismic wave propagation, mainly by attenuating faster/higher frequencies more than they do lower frequencies, resulting in lower frequencies being recorded from the signals that come from greater depths.

Lateral resolution assists in distinguishing displaced features on the same horizon as two distinct adjacent events (Chopra, 2006). Spatial resolving power of seismic data is determined by the Fresnel zone, which is an area where reflected energy from the reflector arrives within a half wavelength. The area of the Fresnel zone can be calculated using:

$$Fr = \frac{v TWT}{2} \left( \frac{1}{f} \right)^2$$

Equation 4

whereby  $v$  is velocity,  $TWT$  is two-way time travel, and  $f$  is frequency. These zones are measured using unmigrated seismic data (Herron, 2011). With increasing depth and seismic wavelength, lateral resolution decreases. Seismic migration can improve lateral resolution by increasing the frequency and collapsing the Fresnel zone which reduces the radius (Lines and Newrick, 2004; Yilmaz, 2001; Herron, 2011).

### 3.4 SEISMIC INTERPRETATION

Post seismic processing of data, 3D seismic data can be used to derive geological structures (e.g., faults, stratigraphic layers, and unconformities) which can be used to build a 3D subsurface geological model (Yilmaz, 2001). According to Dentith and Mudge (2014), interpretation is a qualitative process, whereby seismic vertical sections are examined in inline, crossline or any random direction, such as a time slice (Yilmaz, 2001; Manzi et al., 2012). Where seismic resolution cannot enhance geological features due to its limitations, seismic attributes can be used to detect features that are below the resolution limits (Herron, 2011). Contrast in acoustic impedance is used to pick strong seismic reflectors. This response of seismic reflectors comes from an attribute known as amplitude, which can be correlated to trends in the geological structures together with the involved rock and fluid properties (Herron, 2001).

### **3.4.1 Stratigraphic vs Structural Interpretation**

Seismic interpretation is approached mainly to identify horizons and faults. Amplitude plays a vital role such that maximum positive (peak) and maximum negative (trough) are used to determine an increase or decrease in acoustic impedance (Yilmaz, 2001). Boundaries between rock types, and/or erosive surfaces are identified when there is a significant impedance contrast between two layers. Stratigraphic interpretation is primarily based on identification of depositional sequences based on the changes in amplitude due to these changes in acoustic impedance (Lines and Newrick, 2004; Herron, 2001). Conversely, structural interpretation is based on reflection times that coincide with geological boundaries (Yilmaz, 2001; Herron, 2011). The fundamental difference between horizons and faults in a seismic section is the implication of the former exhibiting continuous seismic reflectors and the latter exhibiting patterns of discontinuities or truncation of reflectors (Lines and Newrick, 2004; Herron, 2011). The continuity of reflective horizons is determined by a process of interpretation known as picking or tracking.

### **3.4.2 Manual picking and Autotracking.**

Picking or tracking is an interpretation process used to correlate reflective horizons on seismic sections manually or automatically (autotracking). The choice between manual picking or autotracking is dependent on reflection continuity and data quality (Herron, 2011). Manual picking defines correlating the reflection by tracing the trends seen on the seismic section. Conversely, autotracking uses a computer algorithm to help trace the reflection horizons more swiftly, accurately, and efficiently, depending on the state of the data. Based on data, the interpreter sets the parameters which control the efficiency of the algorithm (Bizarro, 1998; Admasu et al., 2006). The most significant advantage of auto-tracking is that it draws attention to structures that are discontinuous. This allows the discernment between minor structures (minor fault) and major structures. This process assists in highlighting the structures and processes that occurred within the basin (Bizarro, 1998 and Herron, 2011). These parameters are dependent on the area due to spatial variations in geology or data, thus can be changed at the discretion of the interpreter (Admasu et al., 2006; Herron, 2011). Once the parameters have been

decided on, several starting points for the chosen tracking parameter are marked on the horizon. These starting points are known as seed points and are used for making correlations. Where there is no continuity or consistent reflection response suitable for autotracking, owing to reasons such as structural complexities in geology or poor data quality, horizon picking must be done manually (Dalley et al., 2007). Additionally, manual picking is an essential tool for fault picking (Herron, 2011; Manzi et al., 2012).

### **3.5 SEISMIC ATTRIBUTES**

Seismic attributes are a quantitative process of measuring seismic characteristics of subsurface strata (Chopra and Marfurt, 2005). Seismic attributes enhance and allow the study of small to large scale features (Herron, 2011; Manzi et al., 2019). This in turn allows accurate and detailed information to be provided on structural, stratigraphic, and lithological parameters of the seismic prospect.

Additionally, seismic attributes qualitatively analyze the geometry and physical parameters of the observed subsurface. The physical parameters of the rock type affect the amplitude, thus resulting in changes in acoustic impedance and reflection coefficient, while phase component determine the geometric parameters such geometric configuration (Taner, 2001). For this study, horizon-based and volumetric-based seismic attributes are used. Horizon-based attributes include edge detection, dip, dip azimuth and amplitude, whilst volumetric-based attributes include curvature and ant-tracking (Brown, 1996; Brown, 2001).

#### **3.5.1 Horizon seismic attributes**

##### **3.5.1.1 Dip and dip azimuth**

The amount or magnitude of inclination of a horizon and direction of the inclination from a local reference are known as dip and dip azimuth, respectively, calculated at each sample of the horizon grid (Riks and Jauffred, 1991; Dalley et al., 2007). These attributes are not only useful for the detection of faults and fractures, but also in the identification of displacements overlooked on seismic amplitude data. In addition to this, structural relationships such as cross-cutting and conjugate faults are enhanced (Chopra and Marfurt, 2007a; Manzi et al., 2012a). Dip and azimuth are calculated by fitting a plane along adjacent data points and computing the mean gradient (Riks and Jauffred, 1991; Dalley et al., 2007). The calculation is represented by:

$$dip\ magnitude = \sqrt{\left(\frac{dt}{dx}\right)^2 + \left(\frac{dt}{dy}\right)^2}$$

Equation  
5

$$dip\ azimuth = \arctan\left(\frac{dt/dy}{dt/dx}\right)$$

Equation  
6

where  $dt/dx$  and  $dt/dy$  are dip directions in the x and y directions, respectively, expressed in radians or  $ms\ m^{-1}$  (Dalley et al., 2007). For dip magnitude to perform its function effectively, the dip angle of the fault should differ from the horizon dip. Similarly, the dip direction of the fault should differ from the dip direction of the horizon, for dip azimuth to be effective (Riks and Jauffred, 1991). The difference in detectability between dip magnitude and dip azimuth is overcome by combining the attributes (Riks and Jauffred, 1991; Manzi et al., 2012b).

### 3.5.1.2 Edge Detection

The edge detection attribute is a combination of dip and azimuth variations, normalized to the local noise of the interpreted horizon for improved seismic discontinuity detection (Manzi et al., 2012b; Di and Gao, 2014). The technique is reliant on the detection of lateral amplitude and betterment of lateral resolution to characterize fault continuity and connectivity. This is achieved by modifying intensity, hue, and saturation values into a single display (Luo et al., 1996). The resulting high-resolution imaging of structures allows for detection of small-scale faults, and stratigraphic discontinuities, which is useful in the petroleum industry (Luo et al., 1996; Manzi et al., 2012b).

### 3.5.1.3 Envelope Trace Attribute

The envelope attribute is a trace attribute that is independent of phase or polarity of seismic data. It is calculated from a complex trace and governed by the formula:

$$A(t) = \sqrt{x^2(t) + y^2(t)},$$

Equation 7

where  $A(t)$  is the trace envelope,  $x(t)$  is the seismic trace and  $y(t)$  is the seismic trace rotated  $90^\circ$  (Barnes, 2007).

This attribute uses instantaneous energy of signal, proportional to the reflection coefficient in magnitude, to display acoustically strong events which show up as bright spots on both positive and negative events (Barnes, 2007 and Koson et al, 2014). Its ability to connect waveform peaks allows it to highlight features such as discontinuities, change in lithology, faults, and sequence boundary. This attribute is particularly useful when searching for hydrocarbons due to its ability to indicate gas as bright spots in clastic sediments (Koson et al, 2014 and Pigott et al, 2013).

### **3.5.2 Volumetric seismic attributes**

#### **3.5.2.1 Curvature**

Volumetric curvature measures how folded a surface is at a certain point. This attribute can be used to enhance crucial information about faults, folds, fracture orientation, and density in areas where seismic horizons are difficult to trace (Chopra and Marfurt, 2007b; Basir et al., 2013). Furthermore, by removing the effects of regional dip, small scale features such as depositional characteristics are emphasized (Chopra and Marfurt, 2007a). This is achieved through studying the geometric deformation as opposed to amplitude variations, whereby different wavelengths are examined at various scales to determine volumetric estimation of reflector curvature (Hakami et al., 2004; Basir et al., 2013). Curvature is calculated from volumetric methods i.e., estimation and computation of dip and azimuth to produce a full 3D volume of curvatures:

$$z(x, y) = ax^2 + by^2 + cxy + dx + ey + f$$

Equation 8

The shortfall of this attribute is that it does not give the precise location of the structural features identified (Basir et al., 2013). Conversely, it is advantageous such that in regions where there is no continuous surface, the need for picking horizons is alleviated (Chopra and Marfurt, 2007b).

#### **3.5.2.2 Chaos Attribute**

The chaos attribute highlights reflector disruption, known as chaotic texture, by measuring the lack of organization in dip and azimuth (Pigott et al, 2013). Coarse grained channel infill is typical for exhibiting such chaotic textures in a seismic slice. This property allows for one to infer differences or changes in sedimentary facies of varying depositional environments (i.e., sand to shale). Additionally, faults, angular unconformities, channel sand bodies, and fractures are indicated by zones of maximum chaoticness (Koson et al, 2014). The attribute chaos (J) is governed by the formula:

$$J = \frac{2\lambda_2 - 1}{\lambda_1 + \lambda_3}$$

Equation 9

where  $\lambda_1$ ,  $\lambda_2$ , and  $\lambda_3$  are eigenvalues that must be large to compute the dip and azimuth (Randen and Sonnenland, 2005).

### 3.5.2.3 Variance attribute

The variance attribute is an edge method that measures variability between traces (Pigott et al, 2013 and Koson et al, 2014). It is mathematically expressed as the coherence value minus one, thus its known as the reciprocal of the coherence attribute (Lawal, 2016,). Variance measures similarity between waveforms over lateral and/or vertical windows, thus allowing it to highlight discontinuities of faults and stratigraphy. This attribute can be used on both vertical and horizon slice of the seismic volume (Pigott et al, 2013). Due to changes in acoustic impedance along the horizon, features such as channel edges, fractures, unconformities, and major sequence boundaries can be highlighted using this attribute (Koson et al, 2014).

### 3.5.2.4 Ant-tracking

Ant-tracking is an unbiased technique used to identify and track faults and fractures by using various seismic attributes in a 3D seismic volume. The ant-tracking algorithm is based on swarm intelligence, whereby ants use pheromones to guide members of the colony to the most efficient route to food (Silva et al., 2005; Hu, 2014). Through this algorithm, the appearance of faults and related features are sharpened, and noise is suppressed by inputting seismic discontinuity attributes such as coherency (Basir et al., 2013; Miller et al., 2012). Generally, the ant-tracking workflow is initiated by structural smoothing and surface orientated filtering such as edge enhancement, followed by the application of discontinuity attributes such as chaos. The final step of the workflow is applying the algorithm which involves distributing many agents in the 3D volume (Cox and Seitz, 2007; Miller et al., 2012). This algorithm was developed by Schlumberger Stavanger Research and is unique to the PETREL software (Silva et al., 2005).

## 3.6 INTRODUCTION TO WELL LOGS

Well log interpretation is one of the most crucial tools in petroleum geology. A well's geophysical rock properties are continuously recorded from the bottom to the top of the well, at a sampling rate of 15cm intervals, although this can be as low as 2.5mm with certain specialized logs (Asquith et al., 2004 and

Rider, 1986). Well logs are also known as open hole logs as the lithology forms the well wall, whilst the closed hole are cemented and cased, thus the properties of the lithologies cannot be measured (Asquith et al., 2004 and Wong et al., 2009). They are recorded when the drilling tools have been taken out the well unlike MWD (measured while drilling) or LWD (logging while drilling), which occur during drilling of the formation (Asquith et al., 2004).

Logs can be used to calculate or define physical properties of rocks. These properties include but are not limited to porosity, water saturation, fluid type, and hydrocarbon density, all of which are necessary for quantifying the number of hydrocarbons (Bang-Liu, 2003 and Westbrook et al., 2008). Additionally, logs can assist in delineating lithology, grain size and sorting, and sedimentary structures, with the goal of correlating zones and with the creation of structural and isopach maps (Rider, 1986).

There are four important different types of logs (Figure 3.2). These are electrical logs, radioactivity logs, acoustic logs and dipmeter logs (Bjorlykke, 2010). Electrical logs measure the rock's electrical resistivity (R) and self-potential (SP) log (Wong et al, 2009). Radioactivity logs are obtained by measuring the natural emission of gamma rays in a rock, resulting in either a gamma log or density log (Rider, 1986 and Bjorlykke, 2010). The most used type of log in the interpretation process is the acoustic log, which measures how fast sound travels through the rock, thus yielding a sonic log. This log type is particularly useful in determining porosity of the rock and when used in correlation with the density log, it can aid in well ties (Bjorlykke, 2010 and Süs and Shaw, 2003). For this research, sonic logs will be discussed in detail. The dip of beds and laminations in rocks can be measured by a type of electrical log known as the dipmeter log. Other logs such as the caliper log, temperature log and image log measure properties of the well itself (Asquith et al., 2004 and Wong et al., 2009).

Well logs can be used quantitatively and qualitatively. Quantitatively, logging data can determine water-oil-gas contacts and determine the thickness and depth of these zones (Asquith et al., 2004 and Bjorlykke, 2010). Qualitatively, they can be used to correlate the stratigraphy and identify sedimentary facies, based on the characteristic reactions of various types of rocks (Rider, 1986).

When interpreting a well log, one must be aware of the type of mud used for drilling as this influences the log data results (Rider, 1986). There are three types of mud used: oil-based mud, synthetic-based mud, and water-based mud, with the first two types of muds having a rheology more sensitive than that of the water-based mud, specifically to temperature and pressure (Agwu et al, 2021). As of late, oil-based mud is being used frequently (Bjorlykke, 2010).

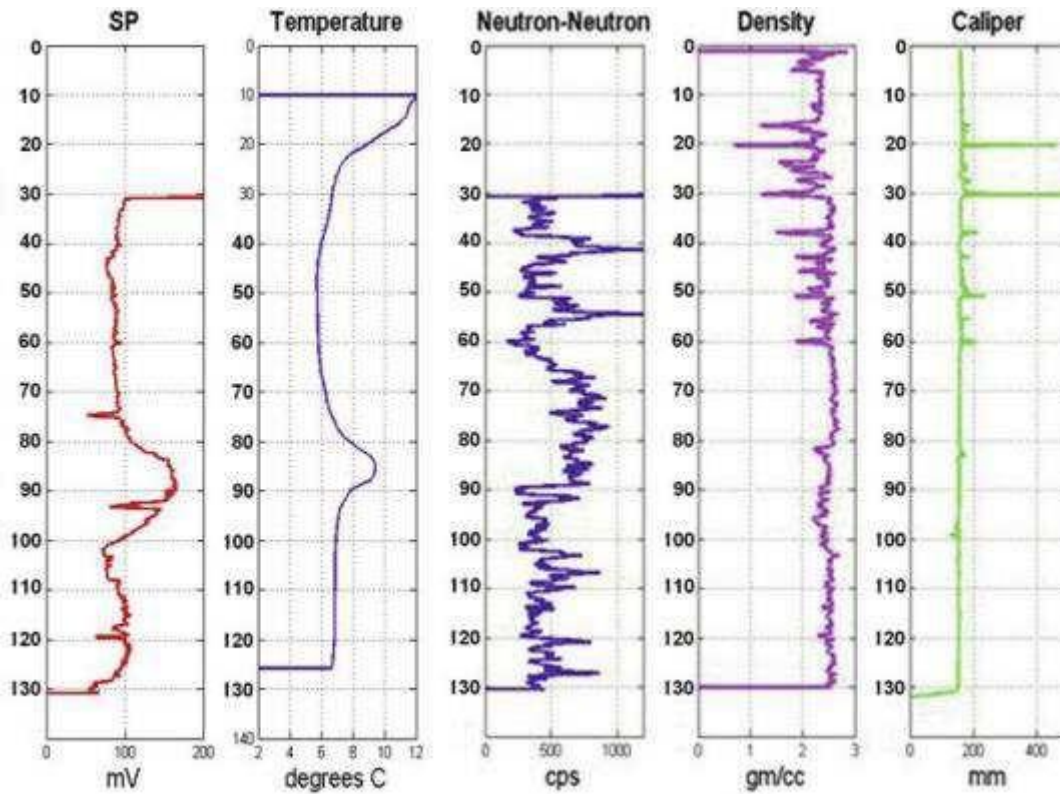


Figure 3.2: Open-hole logs and well logs with their characteristic profiles and units of measurement (Wong et al., 2009).

### 3.6.1. Sonic Log

As mentioned before, sonic logs measure the formation's capacity to transmit sound waves (Rider, 1986 and Bjorlykke, 2010). Sonic logs are mainly used to assess porosity, lithology, and permeability. In seismic interpretation, it is used for seismic section calibration, interval velocities, velocity profiles, and can be used in collaboration with the density log to yield an acoustic impedance log which in turn aids in making a synthetic seismic trace (Asquith et al., 2004). These are the quantitative uses of sonic logs.

The qualitative uses mainly depend on the sensitivity of the log to subtle textural variation in both sand and shales. This enables the identification of lithology and can indicate source rocks, compaction, and overpressure (Asquith et al., 2004 and Rider, 1986).

Acoustic energy is emitted by one or more transmitters, travels through formation and is detected by multiple receivers (Bjorlykke, 2010). The time difference of first arrival p-waves between two receivers is known as the interval transit time ( $\Delta T$ ). It is the inverse of velocity and is measured in  $\mu\text{sec}/\text{ft}$  (Figure 2) (Süss and Shaw, 2003 and Bang-Liu, 2008).

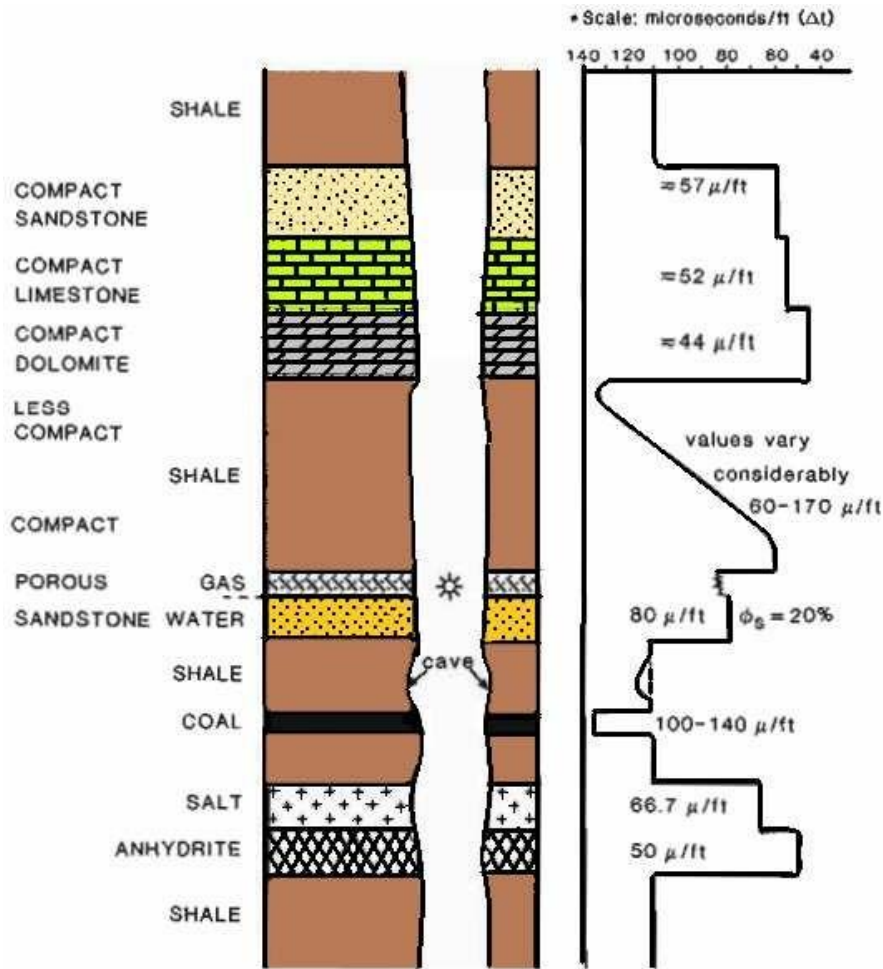


Figure 3.3: Sonic log displaying some typical responses of the lithology within the formation. The interval transit time ( $\Delta T$ ), which increases from right to left, shale and coal typically have high  $\Delta T$  values whilst compacted rock will result in low  $\Delta T$ . The effect of compaction is especially obvious in the thickest shale layer whereby  $\Delta T$  decreases as the rock transitions from less compact to compact. Adapted after Rider, 1986.

There are common undesirable logging effects which may distort the logging data, thus yielding incorrect interpretation if not correct or accounted for. In poor wells, cycle skipping, and noise spikes can occur (Wong et al., 2009). Cycle skipping occurs when the first arrival signal is not detected by the transmitter due to wave attenuation. The transmitter only detects subsequent arrivals, resulting in recorded time being long. Conversely if a noise signal trips a transmitter, it will result in noise spikes on logs, and this is common in limestone (Bjorlykke, 2002).

## 4. METHODOLOGY

In this project, well data will be used to constrain seismic data, allowing for horizons to be picked and the data interpreted (Figure 4.1). The seismic data was acquired by PGS Ramford Viking using a 2 airgun array every 25m, together with 8 streamers which produced 36-fold CMP gathers. The data was processed by Veritas DGC. This process begun with subjecting the data to pre-stack time migration (PSTM), which was followed by many other processes (Figure 4.1) that assisted in attenuating the water layer reverberations.

The well and seismic data acquired from PetroSA was loaded into PETREL Schlumberger 2018 Interpretation Software. A seismic-well tie was then carried out before well logs and corresponding formation tops were loaded and correlated with the seismic volume. Using the well logs, specifically the gamma ray and porosity logs, we apply the artificial neural network algorithm to predict lithologies within the FO-1, FR-1, and FS-1 wells.

Horizons were then picked, initially using automatic picking at every 100th, 50th, 20th and 10th interval. Thereafter, the horizons were picked manually to fix any mispicks that occurred during the automatic picking. Horizon picking and fault picking were done interchangeably where there were discontinuities observed, i.e., horizon displacement. To further enhance these structures, various attributes such as chaos, variance, and envelope ant-tracking were employed. Additionally, the application of these attributes allowed for the delineation of other structures such as pockmarks, gas chimneys and submarine channels.

Further information about each of these steps is provided below (Figure 4.1).

### 4.1 SEISMIC WELL TIES

Seismic-well tie is executed to determine the time-depth relationship between well data (in depth) and seismic volume and/or data (in seismic time). Well FO-1, FS-1, and FR-1 were chosen to tie the seismic data to the wells. A synthetic seismogram was generated using checkshots data, sonic log data, together with density data to better understand the time-depth relationship, while also attempting to understand the seismic response of lithologies at specific well locations. Using those sets of data allowed for the calculation of acoustic impedance, which was in turn used to calculate reflection coefficient (Eq. 1).

The Ricker wavelet was chosen due to its similar behavior to seismic waves in the subsurface, with the wavelet being described by a simple equation where central frequency is the only variable (Bianco, 2016). The frequency of the wavelet was set at 25Hz, with the sampling rate of 2ms, at a length of 128ms. Reflection coefficients were convolved with the wavelet to produce a synthetic seismogram.

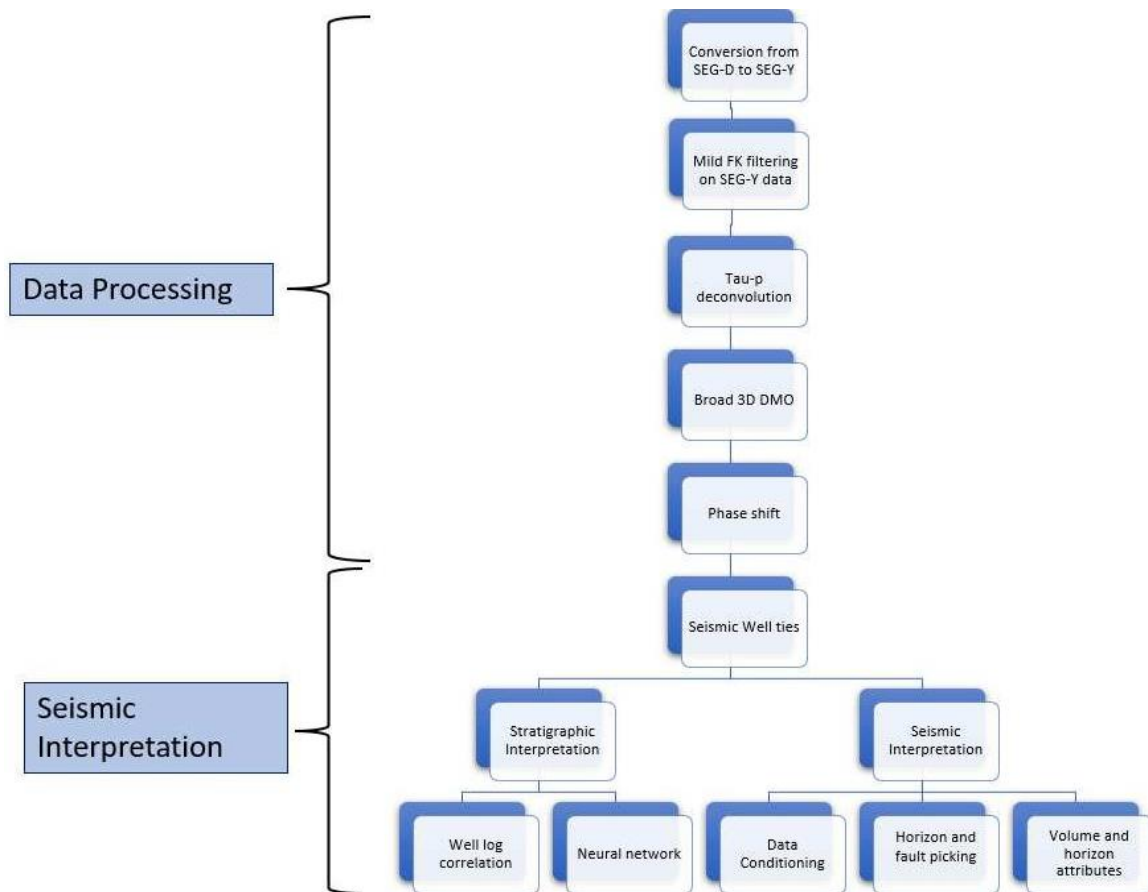


Figure 4.1: The summarized methodology workflow used in the study. The data processing section of the workflow was done by the company that provided the data, whilst the seismic interpretation workflow is part of this study's workflow.

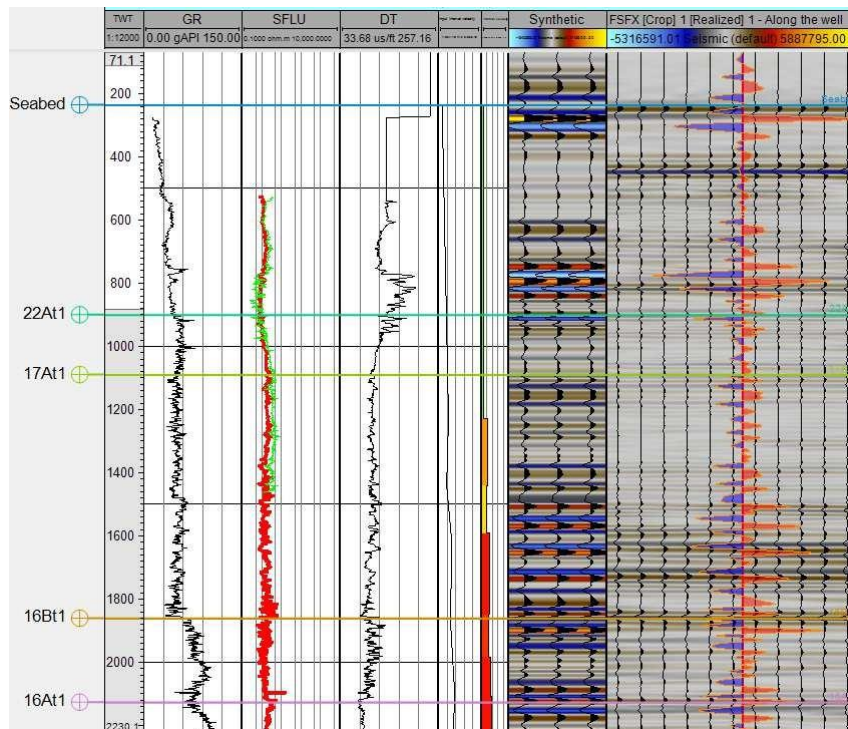


Figure 4.2: Well to seismic tie displaying gamma ray (GR), resistivity (SFLU) and sonic log (DT) from FO-. Sonic and density logs were used to produce a synthetic seismogram, which matches the well log as the peaks

on the seismic panel.

The synthetic seismogram was compared to the seismic volume to determine possible unconformities and pick horizons. Thereafter, the formation tops were imported and correlated with strong reflections in the synthetic seismogram (Figure 4.2).

## **4.2 STRATIGRAPHIC INTERPRETATION**

### **4.2.1 Well log correlation**

The imported formation tops (gamma ray and sonic) were used as guidelines to understand any major changes in the log properties (Figure 4.3.b). Additional formation top horizons were added in areas where there were sharp changes in the gamma ray or sonic logs that did not correlate with formation tops.

To determine the correlation between the different wells, cross-sections were created in the directions WNW to ESE, and NE-SW (Fig 4.3). To better correlate the similarities between log curves, a ghosting tool was used which allows the image of the curve from one well to be imposed on to the curve of another well. Once the wells were correlated, rock types (facies) based on gamma ray values were added onto the curve. The main purpose of the rock types (facies) column was training the neural network, which will be discussed below.

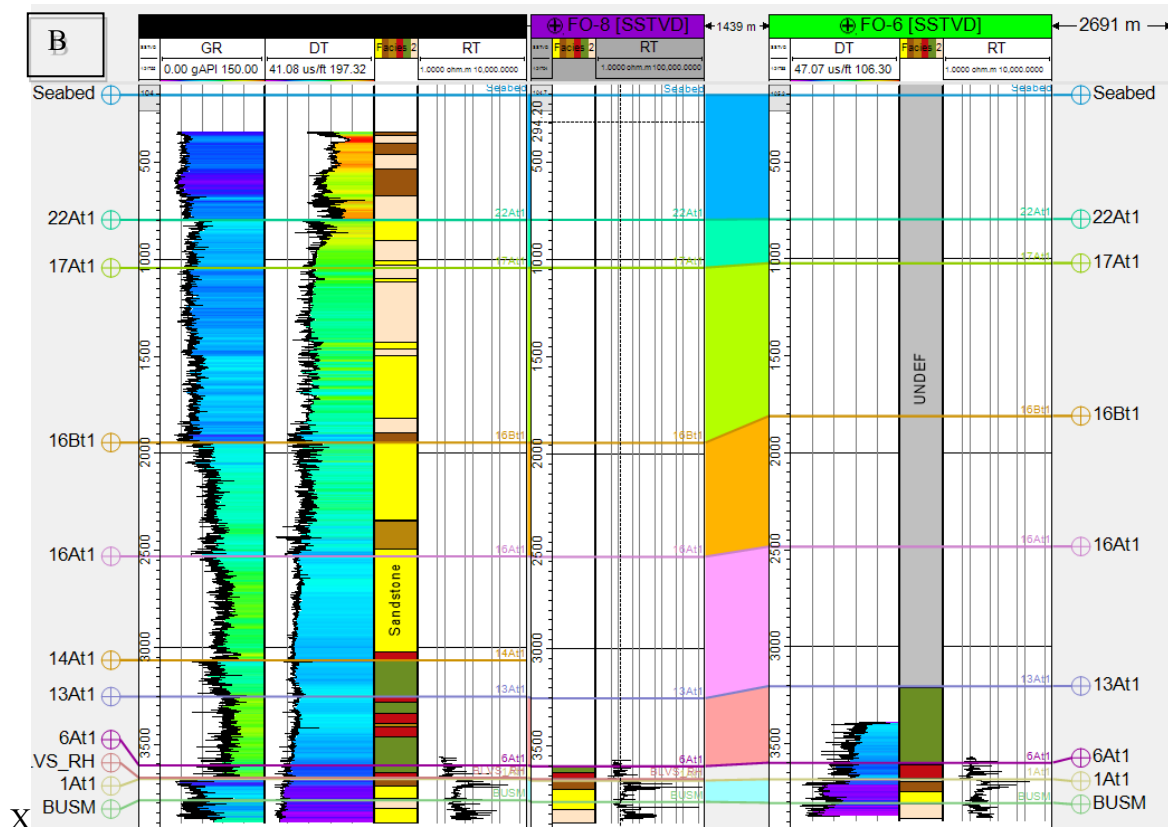
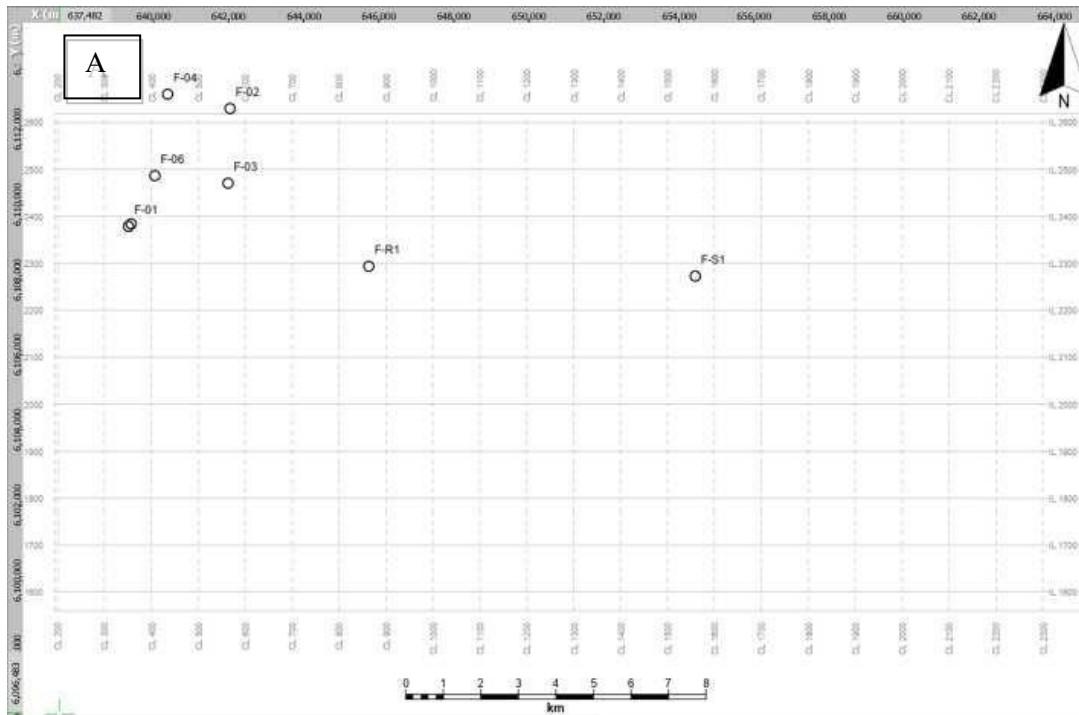
Gamma ray values from the logs were assigned generic rock types according to literature (Figure 4.3.b). These rock types included coarse, medium- and fine-grained sandstone, siltstone, shale, as well as siltstone interbedded with shale. Additionally, core log information was utilized to confirm these rock types, unfortunately, the core logs were limited to certain depths thus the rest of the well lithologies could not be confirmed with ‘physical evidence’.

### **4.2.2 Artificial Neural Network**

As aforementioned, artificial neural network (ANN) was developed to better predict the lithologies of the wells that did not have core logs or missing well information. According to Luisa et al (2009), artificial neural network allows for the extraction of non-linear relationships where there is sparse data. Logs that can be used to train ANN include density logs, sonic logs, gamma ray logs, and porosity logs. In the case of this study, gamma ray and porosity logs were used to train the ANN outcome. ANN works similarly to the neurons in the human brain consisting of dendrites, soma,

and axon, such that dendrites receive the signal, while soma calculates and sums signals, for it to be transmitted as information to other cells by the axon. In the case of ANN, a ‘simple neuron’ would consist of an input layer, activation function and output. The input would be the pseudo lithologies, as

well as the gamma ray and porosity logs mentioned above. The activation function would include all these parameters, which would yield the predictive lithologies in other wells as output.



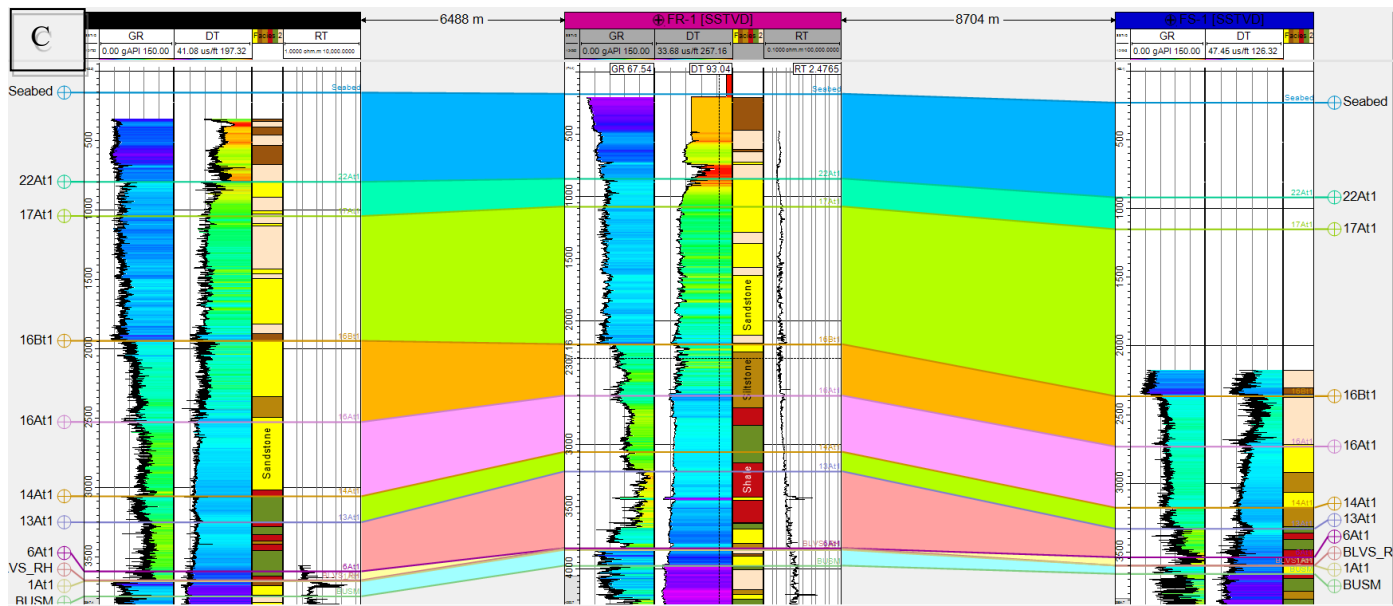


Figure 4.3: a) Location map of wells; b) A NE-SW section well correlation from FO-1 (far left), F-08 and F-06 showing the horizons, gamma ray log (GR) and sonic log (DT) c) A WNW-ESE section showing well correlation from F-01 (far left), F-R1 and F-S1. The well correlations images display the use of gamma ray log (GR) and sonic log (DT) and how it relates to the facies such as sandstone, siltstone and shale.

### 4.2.3 Horizon picking

Initially, well tops were loaded onto the software to determine the possible location of each of the horizons. Mistie analysis was done to determine if there were formation tops that were not aligned with a sharp increase or decrease in acoustic impedance. Strong reflectors were chosen according to their lateral continuity, and auto-tracking was initially used where the lateral continuity was easily observable. In areas that had low S/N ratio, manual picking of the horizons was carried out. The picking was initially done on every 100th, 50th, 20th, 10th, and 5th inline and crossline section, thereafter on every inline and crossline section to resolve mispicks or errors in regions with discontinuous reflections.

The first horizon to be picked was the seafloor (Figure 4.4 and Table 4-1). This horizon was made obvious not only by the formation tops but also by the difference between  $V_p$  and  $\rho$  of the seafloor sediments ( $V_p$ - 1800 ms and  $\rho$ -1079kg/ m<sup>3</sup>) and the seawater above it ( $V_p$ -1534.6 m/s and  $\rho$ - 1020 to 1029 kg/m<sup>3</sup>) (Ayodele et al, 2016). This increase in acoustic impedance is presented as a trough in the seismic section.

The next horizon picked was Paleogene (22At1) in age and is imaged due to the change in velocity (2000ms to 2500ms) and density (1070 kg/m<sup>3</sup> to 1081 kg/m<sup>3</sup>) between the shelf sediments of 22A and Maastrichtian aged deltaic sandstones and siltstones of horizon 17A (Mahlalela et al, 2021). The base of the 17At1 horizon displays a peak due to the change in velocity (3000m/s) and density (1090 kg/m<sup>3</sup>) for horizon 16At1.

The transition into the Turonian-Coniacian aged 15At1 horizon which shows a decrease in seismic velocity from the Santonian aged horizon causes a trough in the horizon. This horizon is mapped as a result of a change in shallow marine sandstones (2700m/s, and  $\rho$ -1090 kg/m<sup>3</sup>) of 16A to the deltaic shallow marine sandstones (Vp-3000m/s and  $\rho$ -2015 kg/m<sup>3</sup>) of 15At1 (Hashim, 2015 and Ayodele et al, 2016). The base of horizon 14A, which is Cenomanian-Albian in age, displays a change (trough) in velocities of siltstones (Vp- 3000m/s and  $\rho$ -2035 kg/m<sup>3</sup>) from the Turonian-Coniacian deltaic shallow marine sandstones (Vp-2700 and  $\rho$ -2015 kg/m<sup>3</sup>) (Brown, 1995 and Mahlalela et al, 2021).

The next unconformity picked is that of the deep marine sandstones and siltstones of Aptian age, 13 A, where there is a change in seismic velocity (3000m/s to 3500 m/s) and density (2035 kg/m<sup>3</sup>to 2050 kg/m<sup>3</sup>). The change from the Aptian aged deep marine sandstones and Barremian aged deep marine shales of 6A is not that obvious as there are only slight changes, with a velocity change from 3500m/s to 3700m/s and a density change from 2050 kg/m<sup>3</sup>to 2061 kg/m<sup>3</sup>(Hashim, 2015 and Mahlalela et al, 2021). However, it does form a slightly observable trough in the seismic section.

The change from Barremian aged deep marine shales and siltstones of 6A, to the deep marine shales of Valanginian aged 1At1 horizon is easily observable due to the strong seismic reflector. This is due to the major change in velocity (3700 m/s to 4500m/s) and density (2061 kg/m<sup>3</sup>to 2070 kg/m<sup>3</sup>) from the 6Aunconformity to the 1A unconformity (Magoba, 2019 and Mahlalela et al, 2021). To ensure quality picked horizons, manual picking was employed in some sections where there was low S/N ratio.

Table 4-1. Major formation tops in the study area, including p-wave seismic velocity, density, age, and sediments found within each layer. These were used to calculate the reflection coefficient of each layer.

	Sediments	Age	Average Vp (m/s)	Average P (g/cm <sup>3</sup> )	Reflection coefficient at boundary
water			1534.6	1.0	
seafloor sediments			1800	1.79	0.35
22A	Shelf sediments	Paleogene	2000	1.7	0.03
17A	Deltaic sandstone and siltstone	Maastrichtian	2500	1.81	0.14
16A	Shallow marine sandstones	Santonian	3000	1.9	0.11
15A	Deltaic shallow marine sandstones	Turonian-Coniacian	2700	2.15	0.82

14A	Siltstones	Cenomanian-Albian	3000	2.35	-0.78
13 A	Deep marine sandstones and siltstones	Aptian	3500	2.5	0.11
6A	Deep marine shales and siltstones	Barremian	3700	2.61	0.05
1A	Deep marine shales	Valanginian	4500	2.7	0.11

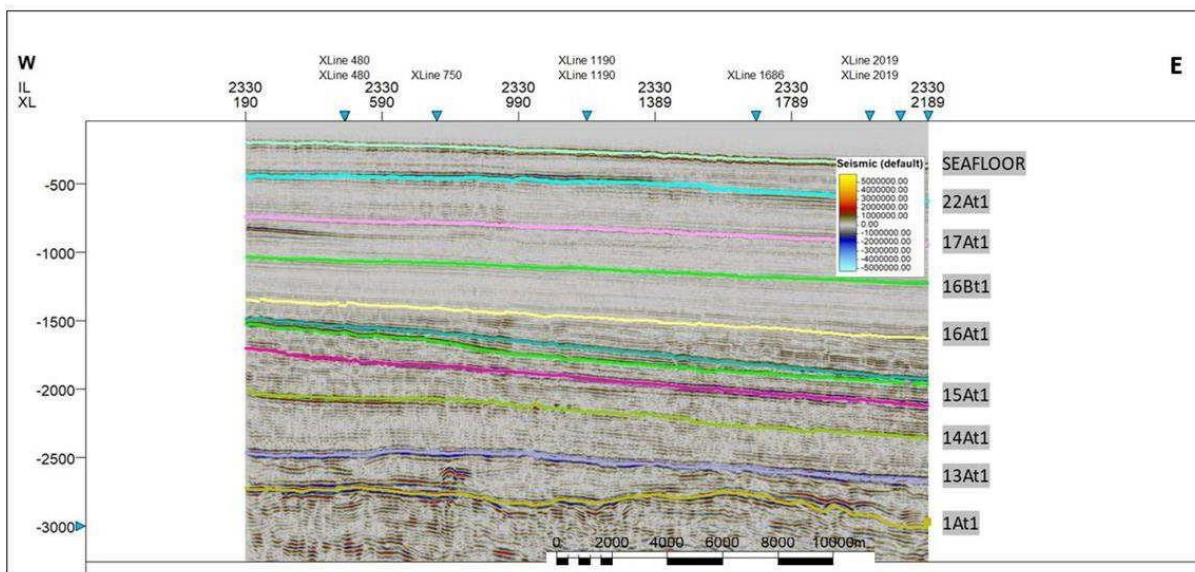


Figure 4.4: Seismic section showing all the horizons picked, starting from 1At1, which is Valanginian in age, up to the present-day sea floor of the Bredasdorp Basin.

Table 4-2 Wavelength of faults and detection limits.

Wavelength	$\lambda/4$	$\lambda/8$
28m	7m	3.5m

## 4.3 STRUCTURAL INTERPRETATION

### 4.3.1 Fault picking

The faults were initially picked across the inline section then across the crossline section as these faults have two sets of strikes. Faults are indicated by termination of continuity in horizons, as well as displacement of the horizon on the opposing side of the discontinuity. A time slice was used to determine whether the faults being picked were correct. It is important to note that not all discontinuities observed are faults; there may be other geological features such as gas seepages, unconformities, discontinuities between reflector packages, or imaging artefacts. The process of picking faults was done interchangeably with picking horizons as this prevents the error in auto-tracking where the horizon is picked in the incorrect place.

To determine the type of faults observed, the type of displacement was determined using the hanging wall (above displacement) and footwall (below displacement). Normal faults are observed when the hanging wall is downthrown relative to the footwall, and reverse faults are observed when the footwall is downthrown relative to the hanging wall. For the fault to be observable in seismic section, the vertical displacement should be greater or equal to one quarter of the dominant wavelength  $\lambda/4$ . If the S/N ratio is high, the detection limit can be defined by  $\lambda/8$ . In this study, the dominant frequency reported in the seismic acquisition is 104Hz, with the average seismic velocity of 2900m/s. Using these parameters, the wavelength and detection limits are calculated in Table 4-2.

### 4.3.2 Ant-tracking Attribute

The basic theory of ant-tracking is described in detail in previous chapters. For a slight recap, it is an algorithm which mimics ant swarm intelligence that uses pheromones to leave trails behind for other colonies to follow. It is an unbiased perspective utilizing a series of unique seismic attributes to identify and track faults. The ant-tracking workflow comprises of four steps. These steps are seismic data conditioning, edge detection (variance or chaos attribute), edge enhancement, and interpretation. These steps are discussed below in terms of their usefulness to this study.

#### 4.3.2.1 Data conditioning

The lowest horizon picked in the study area, 1At1, is structurally complex, with the horizon being discontinuous and showing a lot of displacement. The eastern portion of the seismic volume shows a lot of noise, especially towards the 16At1 horizon. It is not necessarily that the structures are complex, but possibly the energy used to image these horizons has low S/N ratios, or these horizons are at greater depth. In such areas, manual picking was employed as autotracking could not track the remainder of the horizon. Unfortunately, manual picking can introduce inconsistent picking, which are referred to as mispicks due to the lack of clarity in the continuity of horizons.

The solution to this is smoothing the data over areas with poor S/N ratios. Data smoothing is a process that involves using filters to reduce noise such as random noise, spikes, and acquisition footprint

(Chehrazi et al, 2013 and Otchere et al, 2022). These filters are classified into two main groups, namely, nonlinear, and linear filters. Linear filters use a moving window known as a kernel, wherein the input pixel is at the center of the kernel, thus allowing for an averaged weighting of neighboring pixels. This study employed two linear filters, i.e., Kriging and Gaussian filter to smooth data. The Gaussian filter requires that spikes should be removed, pre-smoothing (Randen et al, 2000), and this filter was used for the seafloor and horizon 22At1 as it assisted in removing high frequency background noise. Additionally, this filter was useful for specific horizons (22At1) due to the filter's tendency to smooth out important structures and smear edges, and since these horizons lack mispicks and structures, this will not be greatly affected by the smoothing operation.

Conversely, horizon 1At1 and 16At1 were smoothed using the Kriging filter due to its ability to spatially estimate any point using surrounding data points to find a weighted average value (De Rubeis et al, 2005). Although this method is the best linear unbiased predictor, using this filter runs the risk of losing small scale variability such as minor faults.

#### **4.3.2.2 Edge Detection (Chaos attribute)**

The chaos attribute is known for showing zones with differing chaoticness within the seismic volume, illustrating differences in dip and azimuth. Typically, the chaos attribute is used to enhance faults and chaotic textures such as carbonate reefs, gas chimneys, and channels. Chaos is measured from a minimum of 0 to a maximum of 1, with uncolored values indicating minimum chaoticness and typically the continuity of horizons.

The chaos attribute has one main parameter, which is a directional filter defined by sigma and is best when set between ranges of 1.5 to 2.5 (Figure 4.5). The filter sizes used for this project are shown in Table 4-3.

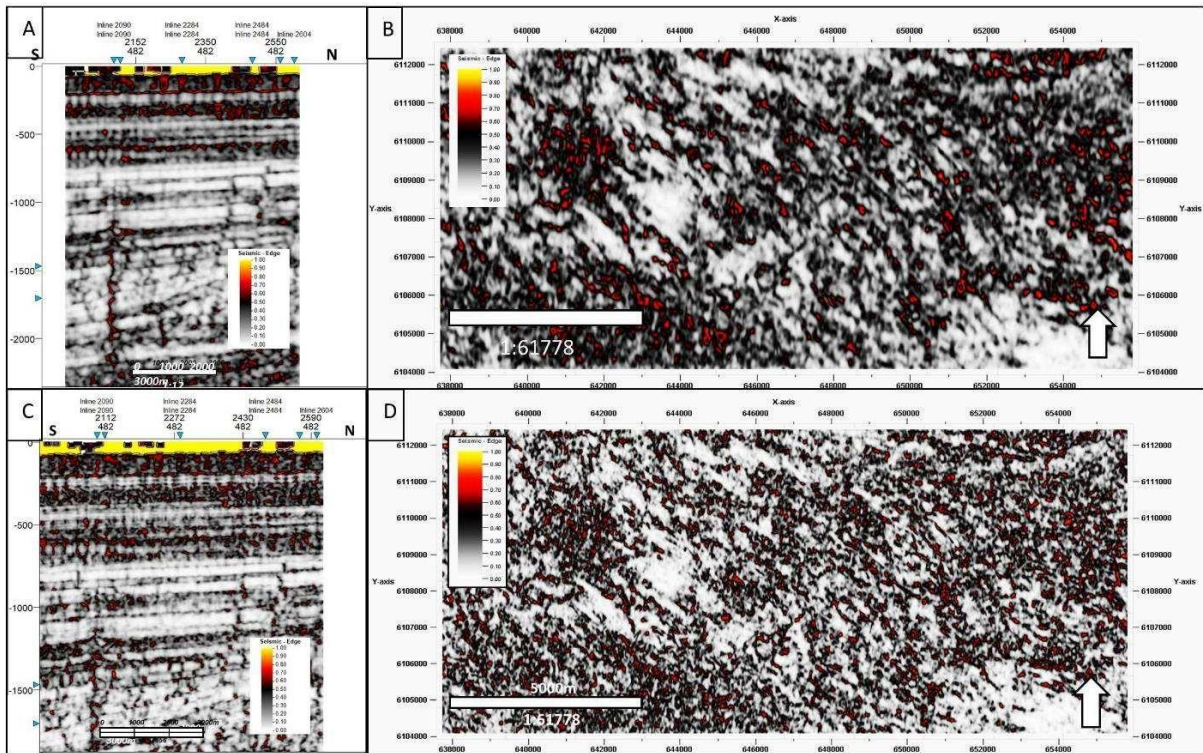


Figure 4.5: Chaos sections showing variations of parameters with the inline vertand crossline as indicators of position. a) Seismic chaos section with sigma filter of 2.5 in the X, Y, Z directions. b) Z slice at the TWT 1467 showing the sigma filter of X, Y, Z in the range of 2.5. c) Seismic chaos section (same as a) with the sigma filter of 1.5 in the X, Y, Z directions. D) Z slice at TWT 1467 showing the sigma filter of X, Z, Y in the range of 1.5.

Table 4-3. Summary of the Chaos attribute parameters that were used in this study.

Filter $\sigma$	X	Y	Z	
	1.5	1.5	1.5	Fig 4.5 c and d
	2.5	2.5	2.5	Figure 4.5 a and b

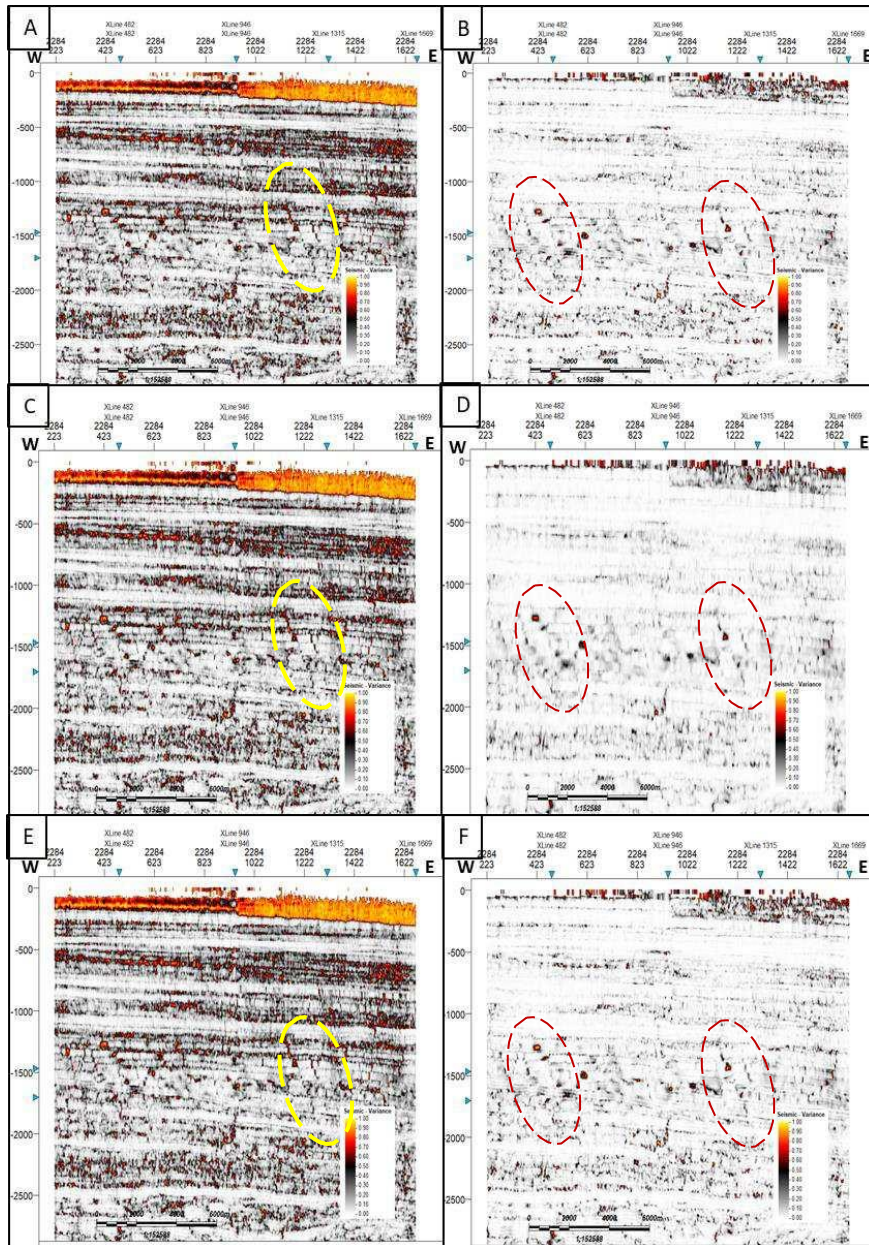


Figure 4.6: Seismic section with the variance attribute applied with different parameters. These parameters include: a) Dip correction on with crossline and inline range of 2 and vertical smoothing of 8; b) Dip correction off with crossline and inline range of 2 and vertical smoothing of 8; c) Dip correction on with the same crossline and inline range of 2 and vertical smoothing of 15; d) Dip correction off with same crossline and inline range, and vertical smoothing; e) Dip correction on crossline and inline range of 3 with vertical smoothing of 8; f) Dip correction off with crossline and inline range of 3, with vertical smoothing of 8. Within the yellow and red circles, these are the faults used to compare the increase or decrease of resolution as the parameters are changed.

The chaos parameters chosen for interpretation were the ones with 2.5 sigma filters as these show the strictures and horizons more clearly when attenuating the noise more. Conversely, the smaller the sigma filter value, i.e., the less clearly structures can be seen. However, this sigma filter value will not contain as much noise.

#### 4.3.2.3 Edge Detection (Variance attribute)

Variance is useful for the extraction of edge features and is best used in areas which have high vertical angle faults. Changes in amplitude due to faults may result in a larger variance. Additionally, features such as igneous bodies that are disruptive to adjacent reflectors have high variances, whilst channel downcutting is highlighted by hot variance colors. The variance parameters in PETREL include inline and crossline ranges, dip correction, and vertical smoothing. The inline and crossline ranges are set equally in both directions, with larger filter sizes resulting in smoother data. The dip correction parameter determines if variance is computed along a dipping plane, while vertical smoothing utilizes a triangular weighting filter to enhance continuity. Ranges for mild smoothing are from 8 to 15 samples, whilst greater smoothing ranges are from 15 to 25 samples (Figure 4.6).

Based on these parameters, it is clear that when dip correction is on, the noise in the background is enhanced, thus making structures such as faults less visible (Figure 4.6. a, c, e). However, when the dip correction is on, the horizons are shown more clearly.

Conversely, when the dip correction is off, the background is attenuated, thus making the fault structures more visible, whilst compromising the visibility of the distinct horizon layers. The parameter for inline and crossline of either 2 or 3 does not seem to affect the images that much, because figure 4.6.b and figure 4.6.f look very similar. However, when the vertical smoothing is changed from 8 to 15 from figure 4.6.b to figure 4.6.d, the resolution of the structures seems to lower in the latter. Using these results, images that had dip correction on were used to assist in picking the horizons, while the images that had an inline and crossline range of 2 or 3 with vertical smoothing of 8 was used to pick faults structures within the study area (can be varied between 0 and 50).

#### **4.3.2.4 Ant-tracking algorithm with edge enhancement attributes**

In this section, for the first step whereby we apply ant-tracking, the attribute structural smoothing (data conditioning) was not utilized as it may cause a loss of structural information while removing noise. The demonstration of smoothing in the previous section was to see the effects that smoothing would have on interpreting data. Unfortunately, smoothing the data prior caused the lose of valuable structural information. For the second step, referred to as edge detection (variance and chaos), variance was used as the method. This was due to its ability to delineate structures such as igneous bodies, faults, pockmarks, gas chimneys, and stratigraphic features such as channel downcutting and unconformities.

The ant-tracking algorithm can either be run on two main modes, passive ants or aggressive ants. The passive mode allows for the extraction of major structural features such as regional faults, whilst similarly, but on a smaller scale, aggressive mode allows for the extraction of subtle discontinuities such as minor faults and fractures. Both passive and aggressive ants have six custom parameters that can be set. These parameters are initial ant boundary, ant track

deviation, ant step size, illegal steps allowed, legal steps allowed, and stop criterion. The values, descriptions and implications of the values used are described in Table 4-4. The last parameter in ant-tracking is the Stereonet filter. This is used to delineate or rather pick which direction of faulting should be enhanced. If the incorrect direction is chosen, it may give redundant information or noisy results. Based on this, certain azimuth and dips were chosen for the study (azimuth of 285 to 150, dip of 0° to 90°), whilst the azimuth values which yielded noisy results, were rejected (Figure 4.7).

Table 4-4. Ant-track parameters used in this study in PETREL Schlumberger software.

Parameter	Aggressive ants	Passive ants	Description	Implication of values
Initial Ant Boundary	5	7	Limits the proximity of the ants placed within the seismic volume, thus controlling number of ants generated.	Larger values result in fewer ants which causes less detail to be captured.
Ant Track Deviation	2	2	Controls how far ants deviate on either side of tracking direction.	Greater value assumes more connections.
Ant Step Size	3	2	Determines the increment at which the ant agent advances for each search.	Increasing values allows ant to search further but decreases resolution.
Illegal Steps Allowed	2	1	Defines how far an ant agent can search beyond its current location, provided that no edge is detected.	Larger value will increase agent search connection.
Legal Steps Required	2	3	Controls the extent to which an ant can search beyond a detected edge.	Lower values result in restrictive action and more connections.
Stop Criterion (%)	10	5	Terminates an ant agent's advance if too many illegal steps occur	A larger percentage assumes further advancement of the ant.

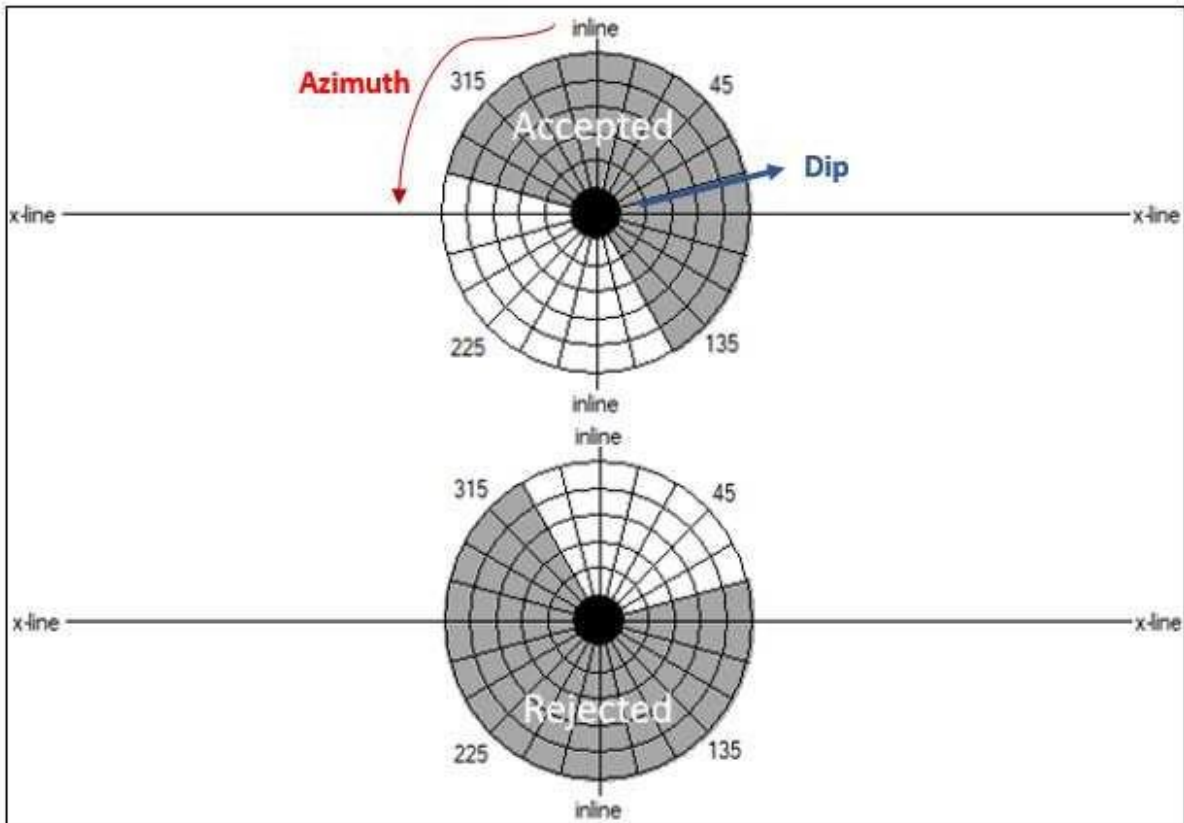


Figure 4.7: Stereonet filter used for ant-track to determine which dip and azimuth would be accepted for extracting faults. The grey area is the range of azimuths that were rejected, and the white is the range of azimuths that were accepted when running the ant-tracking filter. The red arrow indicates that the azimuth is the region 'around' the Stereonet and the blue arrow shows the dip which goes from degrees at the center of the Stereonet to 90 degrees at the outer edge of the circle/Stereonet. The accepted region has a dip ranging from 0° to 90° and Azimuth ranging from 285 to 150 (top). Conversely, the rejected region has a dip of 150 to 285 and an azimuth ranging from 75 to 330.

## 5. HORIZON PICKING USING STRATIGRAPHIC CORRELATION

First well log correlation was carried out, followed by the filling in of gaps in the lithology log using artificial neural networking. This then allowed for the clear picking of horizons in the seismic volume. An analysis of the sequence stratigraphy from the seismic volume could then be carried out to better understand the depositional environment.

### 5.1 ARTIFICIAL NEURAL NETWORK

Once well log correlations were carried out, artificial neural networking (ANN) was carried out to help predict lithologies where there were gaps in the logs, with gamma ray logs being used as a method to determine rock types based on the radioactive decay of thorium, uranium, and potassium in the rocks. (Chow et al, 2005).

Table 5-1. Rock types and the corresponding values of gamma ray (API) and associated Uranium, Thorium and Potassium values.

Rock Type	GR (API)	U (ppm)	Th (ppm)	K (%)
Interlaminated silt and shale	100.2	2.5	9.8	7.3
Stratified silt and clay	99.4	1.1	9.4	6.7
Radioactive shale	99.2	0.7	9.2	6.5
Interlaminated sand. bioturbated	89.3	0.04	7.9	5.2
Shale and silt /Marga bioturbated	73.5	0.03	8.3	5.6
Marga. bioturbated	71.8	0.03	8.0	5.32
Intercalated sand and shale	58.4	0.1	6.8	4.3
Interlaminated argillaceous silt	55.2	0.2	5.9	3.5
Medium grained Sandstone	52.7	0.14	6.4	3.9
Conglomerates. breccia	29.6	0.55	2.3	0.7

There is a general pattern of coarse lithologies being associated with lower gamma ray values, whilst the finer lithologies are associated with higher gamma ray values. Similarly, the density values of coarse lithologies are low to medium, while the density values of the finer lithologies are high (Figure 5.1). This relationship was therefore used to fill in gaps in the lithology log using ANN. The results and summation of these lithologies can be seen in Table 5-1.

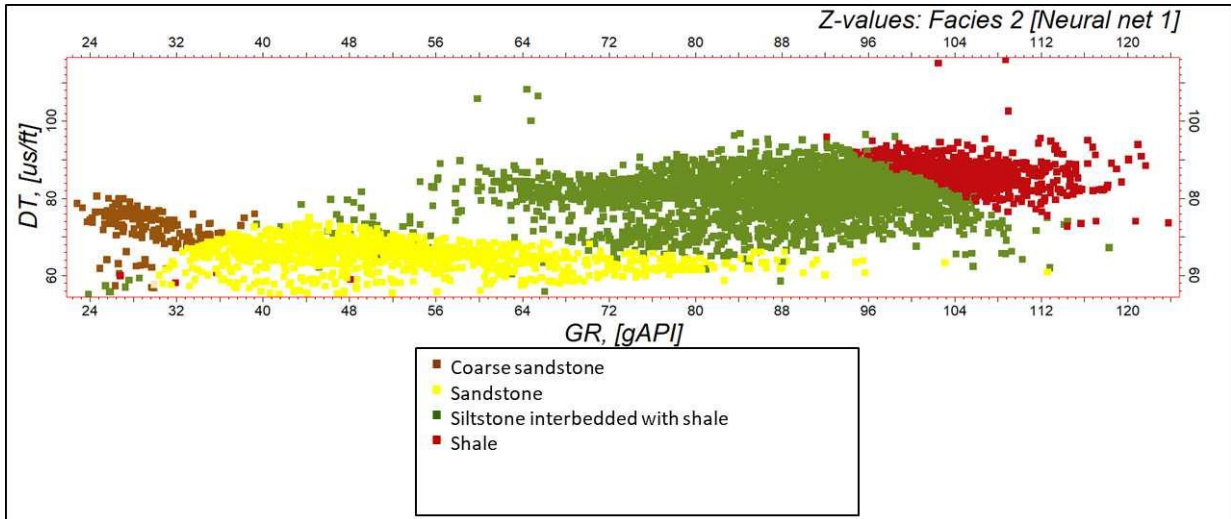


Figure 5.1: Sonic velocities (DT) versus gamma ray values (GR) for a range of rock types. Coarse sandstones show low sonic velocities (DT) and gamma values (GR), medium grained sandstones show low sonic velocity values but range in gamma ray values, siltstones have medium to high gamma and sonic values, whilst shale shows highest gamma ray and sonic values. This data was obtained using FO-1, FS-1 and FR-1 wells.

Table 5-2. Summary of the lithologies assigned using gamma ray (density) and seismic velocity values using the process of artificial neural networks.

Rock type	Sonic Velocity	Gamma Ray	Additional notes
Coarse sandstone	60 to 80 us/ft	24 to 38 gAPI	
Medium to fine sandstones	55 to 72 us/ft	32 to 88 gAPI	Exceptions of outliers that go up to 112 gAPI.
Siltstones interbedded with shales	62 to 90 us/ft	64 gAPI and 108 gAPI	An anomalous point between 44 to 64 gAPI
Shale	80 to 94 us/ft	90- 116 gAPI	Anomalous points around 76 us/ft and above the gamma ray values of 116 gAPI

## 5.2 STRATAL PATTERNS

Sequence stratigraphy is key in predicting depositional environments that existed within the study area during its evolution, as well as the external factors that may have affected the deposition, and sedimentation. Sequence stratigraphy is studied here using the seismic reflection method. A stratigraphic package is made up of several stratigraphic units/reflective sequences bounded by stratal surfaces. Stratal surfaces can either be unconformable or conformable. Unconformities are described as an erosional surface or surface whereby there was a hiatus in deposition. Conversely, a conformity or rather a conformable sequence is where there was no hiatus in deposition and/or between two surfaces (Mountain et al,2007). There are several reflective sequence patterns that have been observed in this study. They are categorized into two groups; those that terminate or are affected by the lower sequence boundaries, such as onlap and downlap; and those that are affected by the upper sequence boundaries, such as toplap and off-lap (Figure 5.2). Onlap is described as a surface which terminates against an older inclined stratum. This is normally seen in angular unconformities. Downlap also terminates against an older stratum; however, the older strata are horizontal as opposed to inclined. Toplap occurs when the strata terminate against a younger sequence above them (Figure 5.2). This regularly occurs in shallow marine deposits, specifically deltaic complexes. Unlike toplap patterns, an off-lap pattern has a nonsystematic termination against other strata and is typical in prograding basins. Using these sequences, one can determine reflection configurations. The four basic configurations are: parallel, divergent, prograding (sigmoid) and chaotic reflection (Figure 5.3).

From above 16At1 to present or in this case, the seafloor, the strata are all parallel to sub-parallel, with no truncation of any of the strata (Figure 5.4). The analysis of the stratal patterns in the seismic volume was carried out from the 1At1 horizon upward, which is mid-Hauterivian in age. From the 6At1 horizon to just above 13At1 (Albian), the strata appear to be semi parallel to parallel (Figure 5.4), while below 14At1, the horizons are truncated on the east side of the section, hence there is toplap (Figure 5.5). Above the 14At1 horizon (mid-Albian), the strata above it which is younger, truncates onto the 14At1 horizon, and this is known as downlap (Figure 5.6). The pattern of toplap is seen once again below the 15At1 horizon which occurs during the Cenomanian. However, the younger strata above the 15At1 horizon show a downlap pattern which is when younger strata terminate against less inclined older strata (Figure 5.7). Above this downlap series, there are more patterns of toplap series, shortly followed by onlap.

Finally, in the horizon below 16At1, there is an occurrence of toplap, and this occurs at the age of the Coniacian. There is another occurrence of toplap at 15At1 and the horizons above it up to 16At1, accompanied by a downlap at 15At1 onto 14At1. This results in a sigmoidal seismic reflection configuration (Figure 5.7). From above 16At1 to present or in this case, the seafloor, the strata are all parallel to sub-parallel, with no truncation of any of the strata (Figure 5.4).

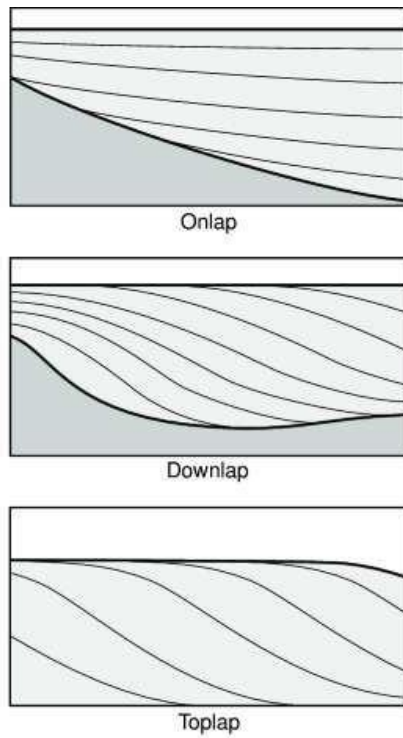


Figure 5.2: Stratigraphic patterns showing onlap, downlap, and toplap, in relation to the top or bottom stratigraphy (Mountain et al, 2007).



Figure 5.3: The four basic seismic reflection configurations (Papadimitriou, 2017).

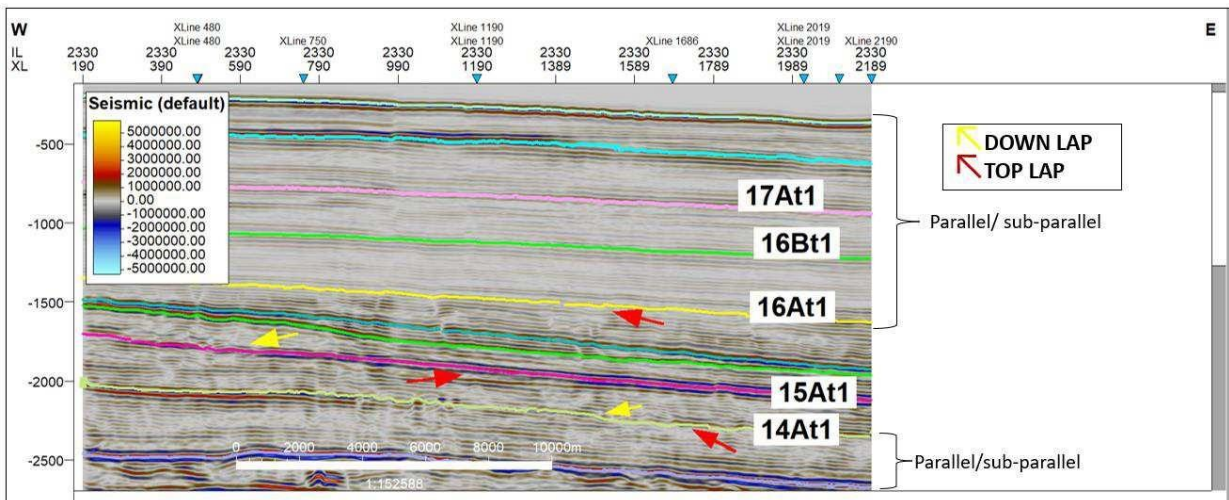


Figure 5.4: Terminating stratal patterns on inline 2330 displaying toplap termination against a younger top boundary, onlap terminating against older strata, and downlap terminating downward against older strata.

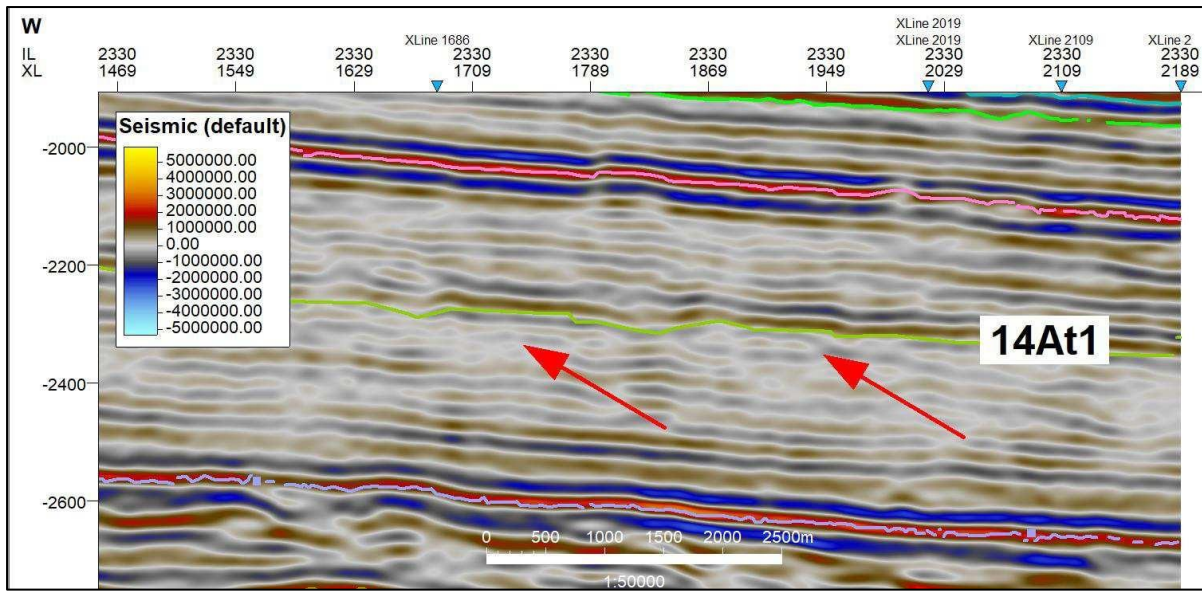


Figure 5.5: The red arrows show a slight toplap termination, however, majority of the layers are subparallel to the 14At1 boundary. While a slight toplap termination can be seen, the majority of the layers are subparallel to the 14At1 boundary.

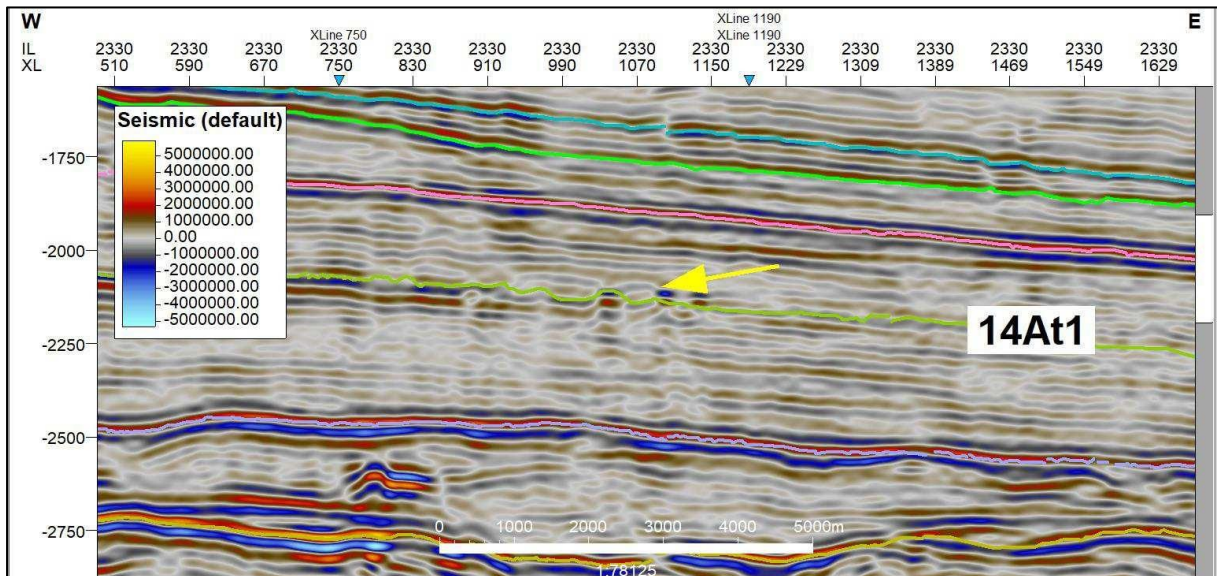


Figure 5.6: Seismic section showing downlap onto 14At1 (yellow arrow) with sediment movement direction from west to east. The strata truncate on to the older horizon (14At1).

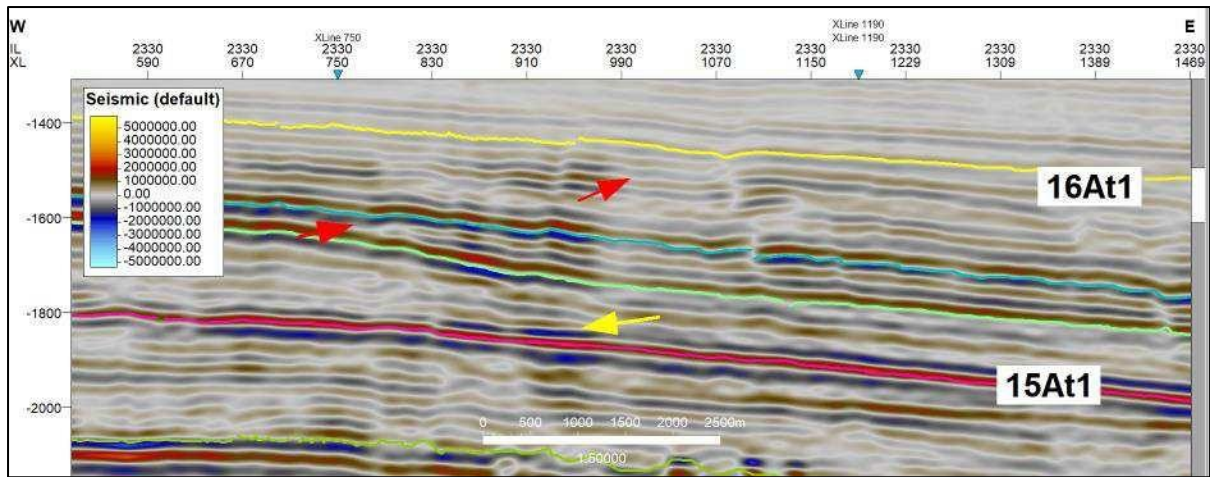


Figure 5.7: Yellow arrow shows downlap truncating on the 15At1 horizon, followed by red arrow showing toplap getting truncated by the 16At1 horizon. The downlap occurs during the Cenomanian age and the toplap occurs below the Coniacian age.

### 5.3 STRATIGRAPHIC ANALYSIS OF GAMMA RAY LOGS

Another method of analyzing stratal sequences and building a clearer cohesive image of a stratigraphic unit is by utilizing gamma ray logs. There are basic log patterns that are attributed to progradation, aggradation, retrogradation and/or a combination of these (Figure 5.8). Progradation typically displays a funnel shape, aggradation displays a cylindrical or serrated shape, retrogradation exhibits a bell shape, and a combination of retrogradation and progradation would result in a symmetrical shape (Radwan, 2001). Furthermore, the fining or coarsening upwards of a sequence is proportionally linked to the increase or decrease of gamma ray values. The implications that this may have on the environment of deposition will be discussed post the results.

Gamma ray logs were compared with lithologies to understand depositional environments. The types of stratal patterns seen above, namely, aggradation, progradation, and retrogradation, have implications on gamma ray sedimentation patterns, as well as the type of depositional environment, which will be discussed in the interpretation and discussion section later.

Starting from the BUSM (base upper shallow marine) to 1At1, there is a general trend indicating upward coarsening of lithologies (Figure 5.9). This is seen in the lithology column where sequence is coarsening upward. This is known as the funnel shape gamma ray trend. From 1At1 to 6At1, there is again upward coarsening, whereby the sequence is underlain by shale and overlain by siltstones (Figure 5.9).

Above the 6At1 horizon (mid-Hauterivian) to the 13At1 (Aptian) horizon, there are alternating lithologies of very similar gamma ray values, namely, layers of shales and siltstones. The 6A sequence is retrogradational due to the funnel shape seen in Figure 5.9 and minor change to bell shape in Figure 5.10. This sequence is quite extensive and shows that either these conditions were persistent for a while, or that the tectonic events that took place thereafter did not affect the sequence as much. The gamma ray trend seen in 13A sequence is known as funnel shaped as there is upward coarsening. The exception is the FR-1 well- on the far right in Figure 5.10, where there is upward fining of the sequence. The trend abruptly changes at 13At1 (Aptian), and once again a funnel shape gamma ray trend is observed with a sudden increase in gamma ray values as shale is overlain by siltstones.

From the Albian age (14At1) to Coniacian age (16At1), a cylindrical gamma ray pattern is observed (Figure 5.11). The lithology column contains sandstones, ranging from medium to fine sandstones. It looks cylindrical in the last well, but the other two wells are more detailed. The Coniacian (16At1) to Santonian age (16Bt1) horizons display a shift in gamma ray pattern. As opposed to funnel or cylindrical shape, a symmetrical shape is observed, whereby there is initial fining upwards of sequence, which transitions into a coarsening upwards as one approaches the 16Bt1 horizon (Figure 5.12). From the Santonian to present day age, there is a general cylindrical shape of the gamma ray log patterns, indicating links to coarse-to-medium-to-fine sandstone.

#### 5.4 INTERPRETATION AND DISCUSSION FOR STRATIGRAPHY

From BUSM to 1At1, the upward coarsening shape is known to occur in environments such as crevasse splays, mouth bars, shorefaces and submarine fan lobes. Considering that this is the synrift period, the most probable environment is a shore-facing regime. In addition, the fact that the lithology is mainly sandstones implies that the source of sediment is very close to land, despite the marine environment (Doust and Summer, 2007). These transitions into a new upward coarsening sequences are seen between horizons 1At1 and 6At1. It can be theorized that this too is a shore-facing environment, based on the similarities of the gamma ray patterns. However, it is a submarine fan lobe, juxtaposed on a lower shoreface, similar to the sequence from BUSM to 1At1. The proposed submarine lobe is suggested due to the change in the lithologies as observed from the wells – shale and siltstones (Figures 5.7 – 5.11) – which are typical in marine regimes. Additionally, the morphology of the gamma ray pattern mirrors the mud submarine lobes discussed by Shanmugam (2016).

From 6At1 to 13At1, the bell shape of the gamma ray log is associated with fluvial bars, channel fill, deltaic channels, and tidal flats, and reefs (Figure 5.8). According to Selley & van der Spuy (2016), during this period, there was progradation taking place, with a rise in sea-level as Falkland was breaking away from the African continent and there was access to sediment supply, hence the observed aggradation pattern. From 13At1 to 14At1, the pattern reverts to a funnel shape (upward coarsening). Due to the thermal sag or subsidence and the effect of eustatic levels, one may suggest that this is a delta front, whereby there is a rise in sea level with low sediment supply. Above this stack pattern, from the Albian aged 14At1 horizon to the Coniacian aged 16At1 horizon, the cylindrical shape is once again observed. This implies that there is aggradation taking place. The environments proposed for this are either a prograding delta or submarine canyon fill. The second proposed environment will be discussed in the later chapters, as to why it is a possibility.

Between 16At1 and 16Bt1, from Coniacian to Santonian age, the hourglass pattern indicates an offshore bar that is constantly reworked by regressive and transgressive phases. Above the Santonian aged 17At1 horizon, the occurrence of a cylindrical shaped gamma ray pattern suggests a fluvial channel environment as there is major uplift, insinuating a shift into the shelf environment (Davies, 1997)

GR Log Pattern	Cylindrical/ Boxcar	Funnel	Bell	Symmetrical	Serrated/Irregular
GR Trend					
Sediment Supply	Aggrading	Prograding	Retrograding	Prograding & Retrograding	Aggrading
Depositional Environment (Common)	Fluvial channels, Carbonate shelf, Reef, Submarine canyon fill, Prograding delta distributaries, Aeolian dunes, evaporite fill of basin	Crevasse splay, River, Mouth bar, Delta front, shoreface, Submarine fan lobe	Fluvial Point bar, Tidal point bar, deep tidal channel fill, Deltaic channels, proximal deep sea settings, Tidal flats	Reworked offshore bar, regressive to transgressive shore face delta,	Fluvial flood plain, Storm dominated shelf, mixed Tidal flat, Debris flow, Canyon fill, Deep marine-slope

Figure 5.8: Gamma ray (GR) log patterns linked to sediment supply and sedimentary facies (Radwan, 2021).

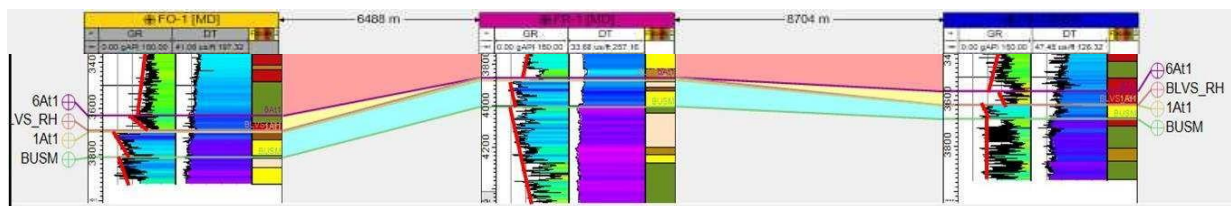


Figure 5.9: NNW to SSE well profile from BUSM to 1A1 and 1A1 to 6A1 showing a gamma ray (GR) repetitive coarsening upward patterning. This is known as funnel shape.

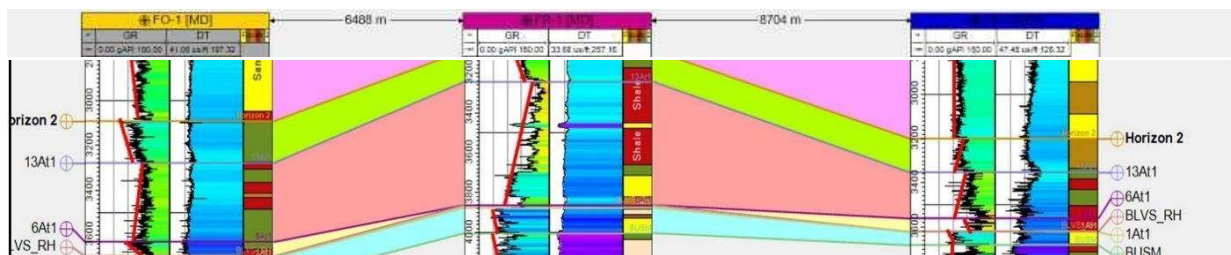


Figure 5.10: NNW to SSE well profile from 6A1(Hauterivian) to 13A1 (Aptian) showing a general gamma ray (GR) trend of fining upward, which is a bell shape.

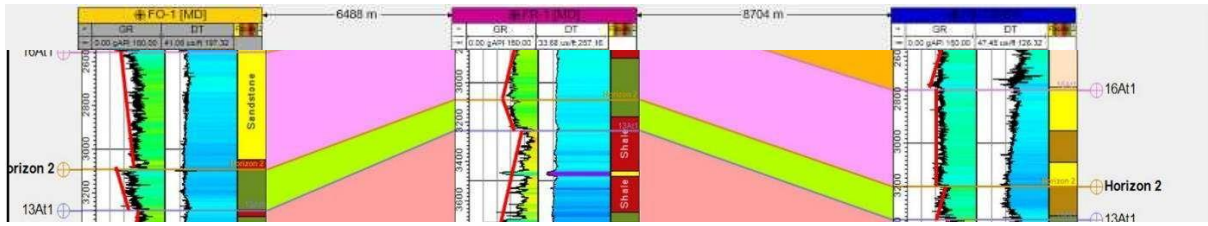


Figure 5.11: NNW to SSE well profile from 14At1 (annotated as horizon 2) to 16At1 (Coniacian aged) displaying a cylindrical gamma ray pattern, whereby there is neither coarsening to fining upward of lithology.

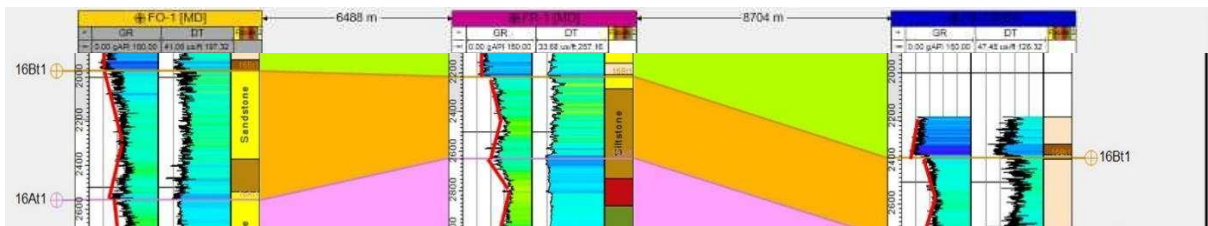


Figure 5.12: NNW to SSE well profile from 16At1 (Coniacian age) to 16Bt1 (Santonian age), showing a gamma ray (GR) pattern with a symmetrical shape, whereby there is initial fining upward of sequence followed by coarsening upward of sequence within one interval.

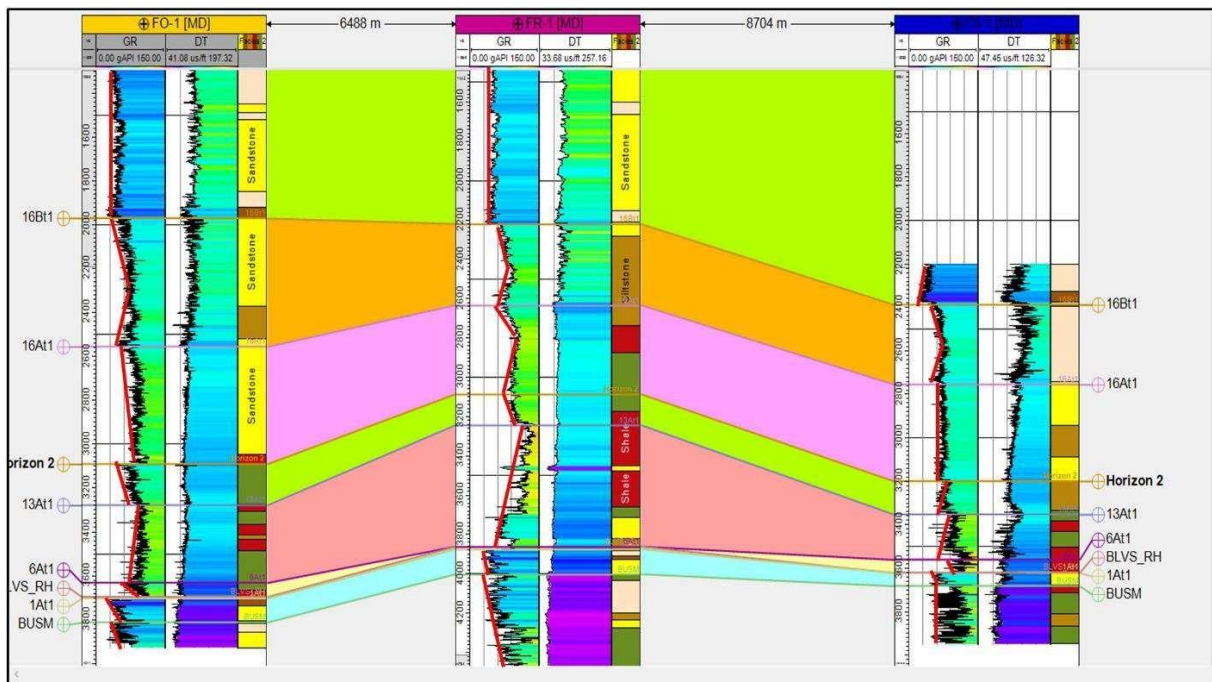


Figure 5.13: NW to SE well profile. Gamma ray log patterns (GR, red lines) in wells FO-1, FR-1 and FS-1 indicating prograding (upward coarsening), retrograding (upward fining) and aggradation sediment supply. This is supported by the logged rock types.

The implication of these stratal patterns is that there was a constant change in environments, and thus periods of either non-deposition, erosion, or tectonism, which affected the stratigraphic stack patterns. The constant changes discussed in stratal patterns seen between 14At1 and 16At1, to the stratal patterns above that which are subparallel (alluding to a stable or con changing environment) indicate a major shift in either tectonic or sedimentation environment. This change can be characterized as being from the syn-rift environment, through this period of transition, into a post-rift environment.

## **6. FAULT PICKING USING VOLUMETRIC AND HORIZON ATTRIBUTES**

The Bredasdorp Basin is a rift basin within the greater Outeniqua Basin. Extensional basins are resultant of magmatism acting on the lithosphere, lower crustal flow, or flexural uplift. Either horizontal or lateral extensional forces acting at the lateral boundaries normally in passive continental margins affect the structures that occur within these environments (Frizon de Lamotte et al, 2015). In the synrift stages, localized extension and faulting can be dependent on pre-existing structures such as normal faults which exploit anisotropies rooted from previous tectonism (Ebinger et al, 1993 and Schlische and Withjack, 1999). There is a characteristic structural architecture documented in rift basins, specifically the basin shape, and this displacement geometry is dependent on the nucleation, propagation, and linkage of the normal fault system.

Displacement on a fault is variable, with the greatest displacement being at the center and going towards zero at the tips. Typically, these normal faults form half graben structures with steep bounding faults exceeding 45° (Schlische and Withjack, 1999). Faults can also be concave upward, in which case they are known as listric faults, with a detachment at depth.

In both unsuccessful and successful rifts, rifting stages may be variable. Post-rifting, there can be further modification of the fault structures caused by either a contractional phase of tectonism or transpressional faulting. Such post-rift tectonism results in fault inversion, which typically has structures such as reverse faults and/or thrust faults (Ebinger et al, 1993 and Frizon de Lamotte et al, 2015).

The importance of rift basins is due to their significance in hosting most of the world's petroleum provinces. Fault detection in rift basins is therefore imperative in seismic interpretation, especially in the exploration phase of oil and gas fields. The structural interpretation of these geological features is done through seismic edge detection methods (Basir et al, 2013). These edge detection methods are especially useful for gaining comprehensive insight into faults and their interactions with related fracturs. Although edge detection methods can be compounded or superimposed on one another to enhance such features, this poses the risk of introducing noise (Pederson et al, 2005). Ant-tracking, as previously mentioned, is such an attribute, and is advantageous as it dismisses structures such as channels because it does not enhance internal chaotic texture, processing effects, or channel boundaries. Ant-tracking is more focused on surface like features having a predetermined orientation range, such as faults. That said, while this attribute may be effective, to obtain a consistent fault interpretation from human judgement or input is also important (Basir et al, 2013).

### **6.1 ANT-TRACK APPLICATION AND SUPPORTING ATTRIBUTES**

As mentioned in the methodology, the ant-track attribute was utilized to pick faults more clearly. Ant-track with a passive filter applied to the seismic data, allowed faults to stand out from the chaotic background. The direction designated on the Stereonet filter is SE to NNW, with the dip ranging from 0° to 90° (Figure 4.7). However, if the Stereonet filter direction is changed (to the rejected region in Figure 4.7), the filter removes or rather over smooths the faults (Figure 6.1.a).

The ant track attribute was initially applied to time slice 1527, due to it depicting the structures best, through the different filters that and angles that were applied. The ant-track results show a few structures which could be interpreted as faults. When applying the passive filter, there seems to be more faults than the smoothed ant-track might suggest (Figure 6.1.b). The aggressive ants show similar trends to the passive ants, however, through applying the aggressive ants, either more noise or minor structures are introduced to the time-slice (Figure 6.1.c and Figure 6.1.d). If these are minor structures, the study will not be using them, as major structures of the region are of more value for the scope of the study.

## 6.2 STRUCTURAL FRAMEWORK

Using the attributes described in section 3.5, faults were delineated and fault properties (i.e., strike, dip, and dip direction) analyzed. The faulting is almost non-existent between horizons 16At1 and 13At1, indicating that there are two major phases of faulting, namely, above 16At1 and below 13At1 (Figure 6.2). In the first phase of faulting below 13At1, the faults predominantly strike E-W, while a few trends N-S (Figure 6.3). The N-S faults are mainly concentrated on the eastern section of the study area. The E-W trending faults display a series of horsts and grabens.

Above 16At1, the faults strike E-W and N-S, which is line with the regional trend observed of WNW-ESE. The faults striking N-S display a repetitive series of normal faults forming horsts and grabens. The E-W striking faults are generally parallel to each other, with the exception of 3 or 4 of these faults intersecting each other to form horsts and grabens (Figure 6.4). Just as the N-S faults were concentrated on the eastern side below 13At1, the same is true for the fault set above 16At1.

When analyzing the dip of the faults, there are two distinct ranges of fault dips observed, which are common to extensional basins. The faults below horizon 13At1 show dip measurements ranging between 20° to 50° (Figure 6.5). These faults have steeper dips towards the top of the fault (50°), and gradually become gentler (20°) towards the bottom of the fault base. In some cases, they become shallower or gentler at both the top and bottom of the fault. On the other hand, the faults above 16At1 are much steeper than their counterparts (Figure 6.5). The dip measurements of these faults range from 25° to 85°. There are some faults which are extremely steep at the top (70° to 80°) but become gentler at the base of the faults (30°). Layer decollement was investigated, and that is not the case here, nor is the evidence available to support this. Additionally, it is mentioned that these faults are common in extensional basins.

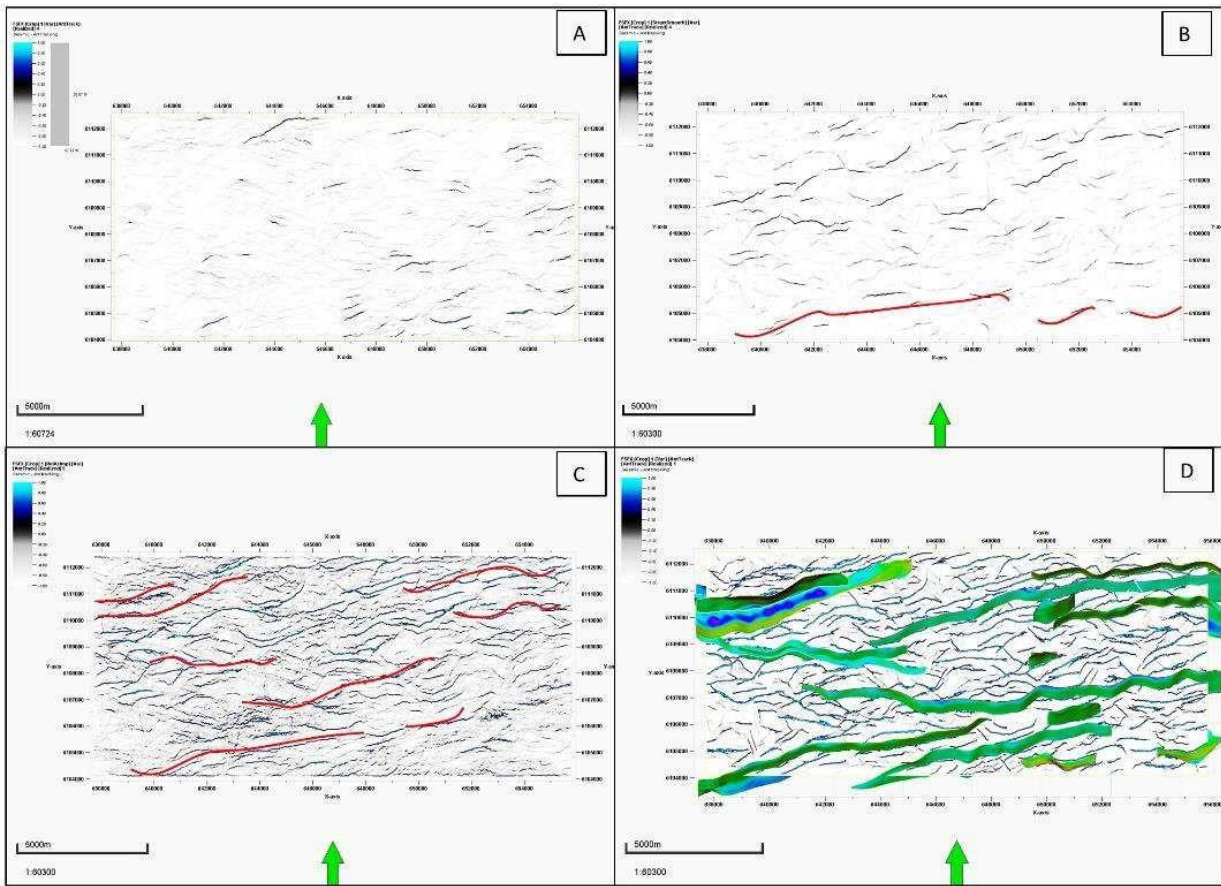


Figure 6.1: Ant-tracking with different filters and attributes applied to TWT 1257. a) Smoothing was applied to the variance slice prior to the ant-track algorithm applied, this attenuated the faults to a point where they nearly disappear. b) Ant-track algorithm without smoothing but with the passive filter applied to it. The red line represents faults that have been picked. c) Ant-track algorithm without smoothing, but with an aggressive filter applied to it. The aggressive filter shows more faults and hence the several red lines are marked. d) Ant-track algorithm showing the tracked faults intersecting this time slice. The general trend is west-southwest to east-northeast.

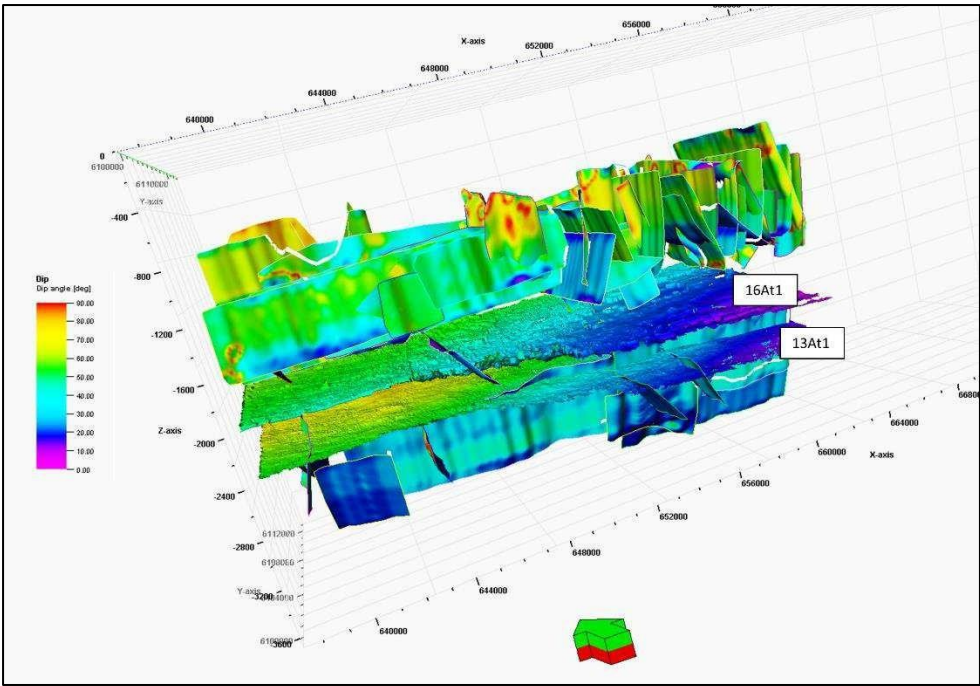


Figure 6.2: Horizons 16At1 and 13At1 and intersecting faults. The colors represent the dip angle. Two phases of faulting are seen below horizon 13At1 and above 16At1, with limited faulting between these horizons.

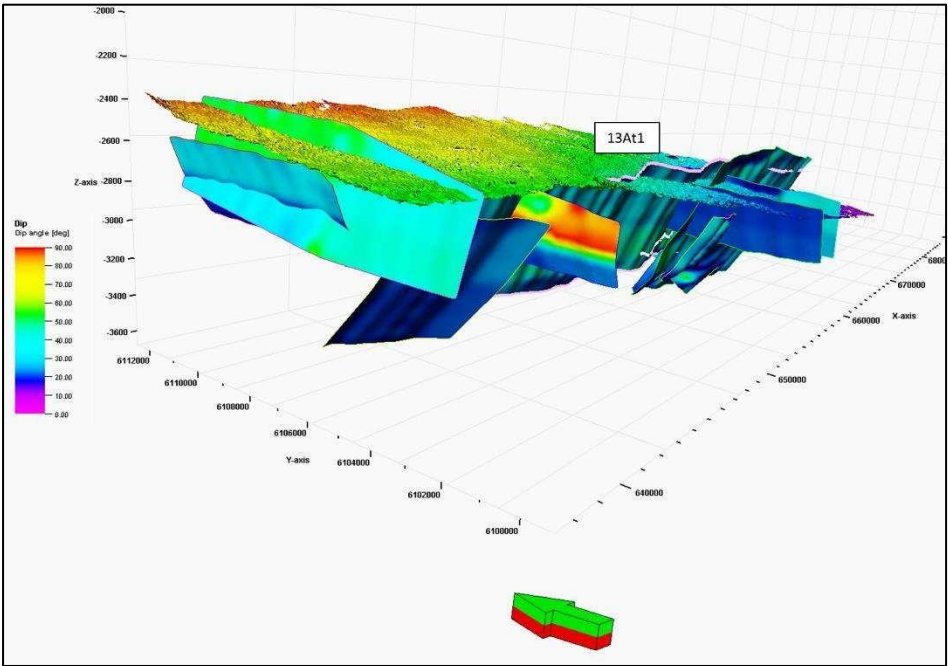


Figure 6.3: First phase of faulting below the Aptian age 13At1 horizon, with the dominant faulting trending E-W.

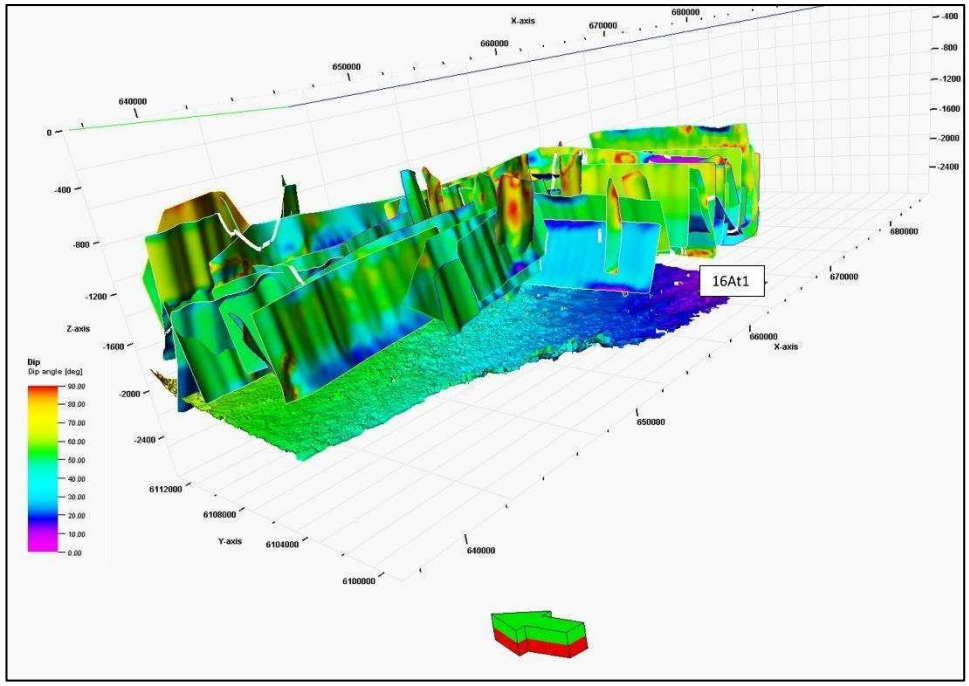


Figure 6.4: Second phase of faulting above the Santonian aged 16At1 horizon, mainly with faults trending N-S forming grabens, and those trending E-W being parallel to one another.

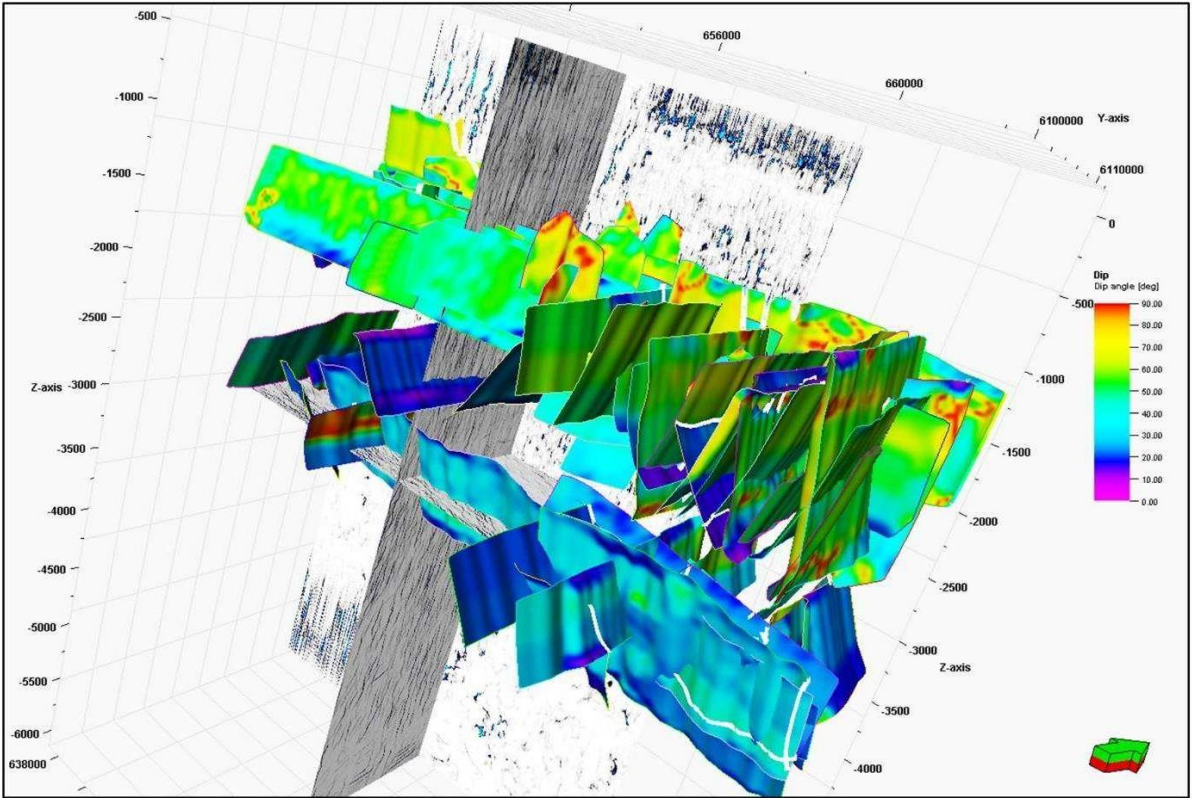


Figure 6.5: Mapped faults in the study area, with two seismic sections with the chaos attribute applied. The first phase of faulting below horizon 13At1 shows faults with dips ranging from 20° to 50°. These faults have a higher dip towards the top and become shallower towards the bottom of the faults, thus exhibiting a listric fault pattern. The second phase of faulting above horizon 16At1 has dips greater than 55°, with N-S faults exhibiting a horst and graben pattern.

### 6.3 INTERPRETATION AND DISCUSSION FOR STRUCTURAL FRAMEWORK

Observations from the study area were compared with available results found in the literature. Davies (1997) showed that rifting took place in three stages, which were the late Jurassic (below 1At1 and BUSM), the Valanginian (below 1At1), and the early Hauterivian (below 6At1). The results of this study exhibit two stages of rifting, below the Aptian aged 13At1 down to below the Valanginian aged 1At1 horizon, and above the Coniacian aged 16At1 horizon with a lack of faulting between. This is supported by the two sets of faults with a clear 'boundary'. The boundary exhibits a hiatus in extension. This hiatus coincides with the period of source deposition during the Aptian age, which is defined by the 13At1 boundary.

The first set of faults below 13At1 which are characterized by grabens and half grabens trending E-W, are very similar to those described by Davies (1997), which were described as early rifting faults trending WNW-ESE. These grabens indicate an extensional regime spreading in the N-S direction, where structures form structural traps for hydrocarbons. These faults have varying dips, with the shallowest dip being at the bottom. This is indicative of listric faults, which according to Shelton (1986), are common in normal faults and flatten with increasing depth. Listric faults are typical in environments where brittle rock overlies ductile rock, often in extensional systems. Additionally, according to McClay and Scott (1991), in horst and graben systems, an upper roll-over with crestal collapse can cause a change in angle of the fault along its plane. This configuration is especially common in extensional environments.

The few faults in this first set that do not follow these trends could represent older faults that were reactivated. This is supported by Dingle (1974) and Davies (1997), whose research suggests that these faults could be inherited from the Cape Orogeny.

For the second set of faults above 16At1, there are two main trends in these normal faults. The first trend would define those that are trending N-S and form grabens, suggesting that the basin extended in a NE-SW direction. This hypothesis is supported by Bird et al (2005), whose research on stress regimes using numerical modelling suggested that the stress direction of the extension was approximately 145°, and of a normal faulting regime.

The second set of faults trend E-W and do not form grabens or half grabens as much but are rather parallel to one another. The implications of this in an extensional regime that has undergone extensive tectonism fault inversions. According to Davies (1997), and Selley and van der Spuy (2016), the normal extensional faults were modified by the dextral shearing of the Agulhas Falkland Fracture Zone (AFFZ), during the separation of Falkland from Africa. Bird et al (2005) suggests that the greatest shear stress is present offshore in the region of the Bredasdorp basin. The commonly accepted suggestion is that these modified faults formed due to the Bouvet hotspot transit as it passed under the basin, causing upwarping and down warping (Storey, 1995).

## **7. EVIDENCE OF HYDROCARBON MIGRATION**

Using the picked horizons and faults, as well as horizon and volumetric attributes, evidence for pockmarks and fluid or gas escape structures were documented. Some of the volumetric attributes used to capture this feature include the envelope and chaos attributes, while the applied horizon attributes include dip illumination and amplitude contrast. The attributes also highlighted an erosive feature that was initially identified on a time slice.

Fluid flow in sedimentary basins is typically seen as sub-vertical structures, often concentrated along features such as faults (Hovland et al, 2002). These sub-vertical structures are used to assess hydrocarbon migration in basins which have potential for petroleum exploration. Differing studies have referred to these structures as gas chimneys, acoustic pipes, or seismic chimneys. A common characteristic of chimneys in a seismic section is highly discontinuous reflections in zones of incomplete coherence (Saeki et al, 2009). The reflections on either side of the vertical disturbance display a sharp upward or downward bend. The surficial expression of these disturbances which help expel the fluids are known as pockmark craters on the ocean floor and they are circular in shape (Hovland et al, 2002 and Saeki et al ,2009).

The incoherency of these features may be due to attenuation and scattering of the signal, hence one should be cautious when delineating such structures.

According to Carlson et al (1988), a distinctive feature of a submarine canyon is cut and fill stratigraphy, i.e., an erosional surface that has been infilled by younger sediments. The cause or creation of canyons can be initiated by several factors, i.e., submarine slides, debris flows, soft sediment deformation, or turbidity currents. In addition, the seismic profile of such structures is known to have hummocky like patterns, that strongly correlate with debris flow.

Another way to identify canyons is by observing contour lines and their proximity to each other, which has implications for the degree of inclination of the slope. In the case of canyons, the contour lines would be very close at the mouth of the canyon, followed by gentler contours which ultimately form an elongate shape (Mauffrey et al,2017).

Submarines canyons are synonymous with passive margins and result from long periods of formation. Due to their place of origin, Liu et al (1993) suggest that submarine canyons originate mainly from tectonic processes.

### **7.1 POCKMARKS AND FLUID ESCAPE STRUCTURES**

The envelope attribute was applied to the seismic volume and time slices were investigated for evidence of gas escape structures.

The time slice 2134 sec TWT is above horizon 16At1 at depths of approximately 2600 m but falls within the zone of faulting (Figure 7.1a). It shows other semi-circular structures, most likely a gas chimney or a paleo pockmark, which has a diameter of approximately 860m (red arrow).

Additionally, a change is seen from the NW corner to the SE corner. The NW corner shows higher values of relative amplitude (deeper hue of blue), whilst the SE corner shows lower values of relative amplitude (lighter hue of blue). This change is seen in both images in Figure 7.1, which lie at different depths. The 1252 sec TWT time slice is approximately at horizon 16Bt1 and is above the picked faults, with a depth of 2000m (Figure 7.1b). This slice shows several semi-circular to circular structures on the western side of the time slice (red ellipse). These structures vary from 400m to 900 m in diameter and are most likely paleo pockmarks. Moreover, using the dip illumination horizon attribute, a paleo pockmark with a diameter of 860 m is seen further north (Figure 7.1b, red arrow). The outer diameter of the circular structure is highlighted due to a high dip ratio. This paleo pockmark in Figure 7.1a is also evident on the dip ratio slice shown in Figure 7.2.

Seismic sections were also investigated to find gas escape structures (Figure 7.3.a). Seismic sections with the chaos attribute (Figure 7.3.b), the variance attribute (Figure 7.3.c) and the envelope attribute (Figure 7.3.d) applied to them, display strata that are disturbed by a vertical structure, with a bit of noise. Applying these attributes, it is observed that the strata are not displaced on either side of the vertical feature. The gas escape structure extends from above 13A (Aptian age) to just above sequence 16B (Santonian age).

When applying the edge detection horizon attribute to this feature on horizon 15At1, the feature is observed on the far western side. Conversely, adjacent to this feature are two black circular to semi-circular features which could be interpreted as paleo pockmarks (Figure 7.4).

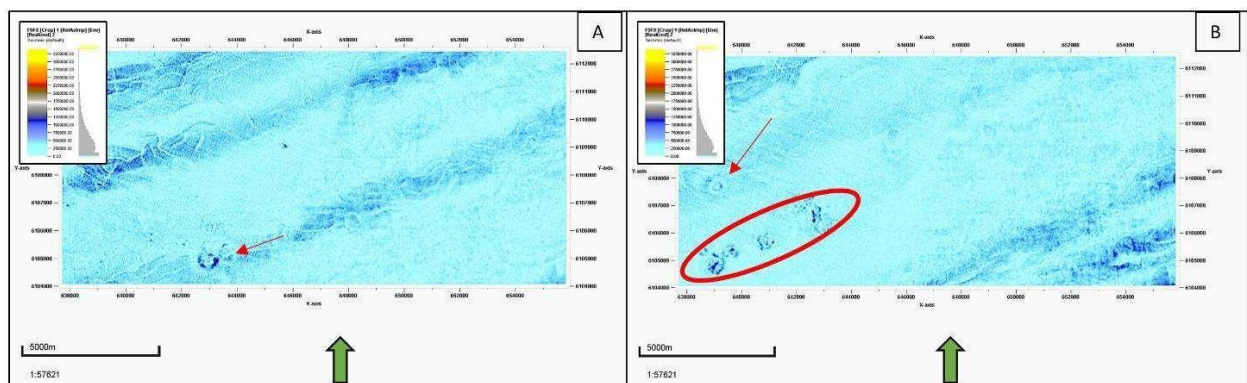


Figure 7.1: Time slices with the envelop attribute applied: a) 2134 sec TWT time slice with pockmark shown (red arrow) with a diameter of 860m. b) 1252 sec TWT time slice pockmarks trending NE-SW (red ellipse) varying from 400m to 900m in diameter. The second pockmark further north has a diameter of 750m (red arrow).

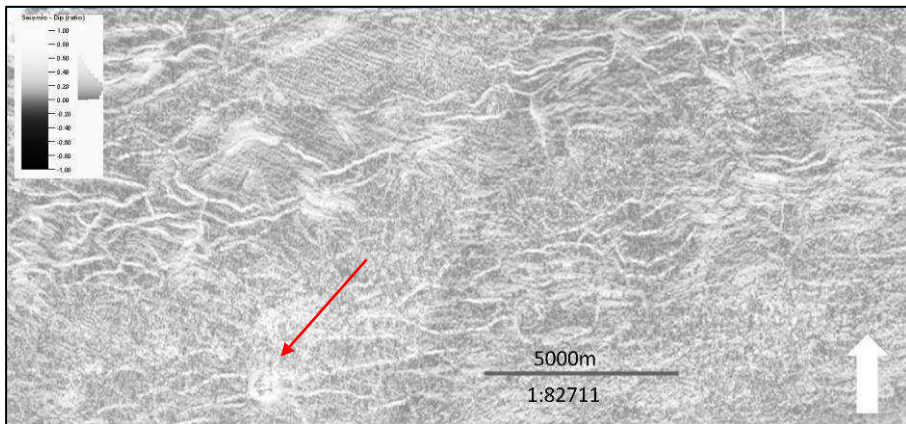


Figure 7.2: Time slice at 2134 sec TWT with dip ratio applied. The pockmark in the southwest (red arrow) is evident, with a diameter of 860m. The diameter of the pockmark is shown by the high dip ratio (white), and the center of the diameter highlighted by the low dip ratio.

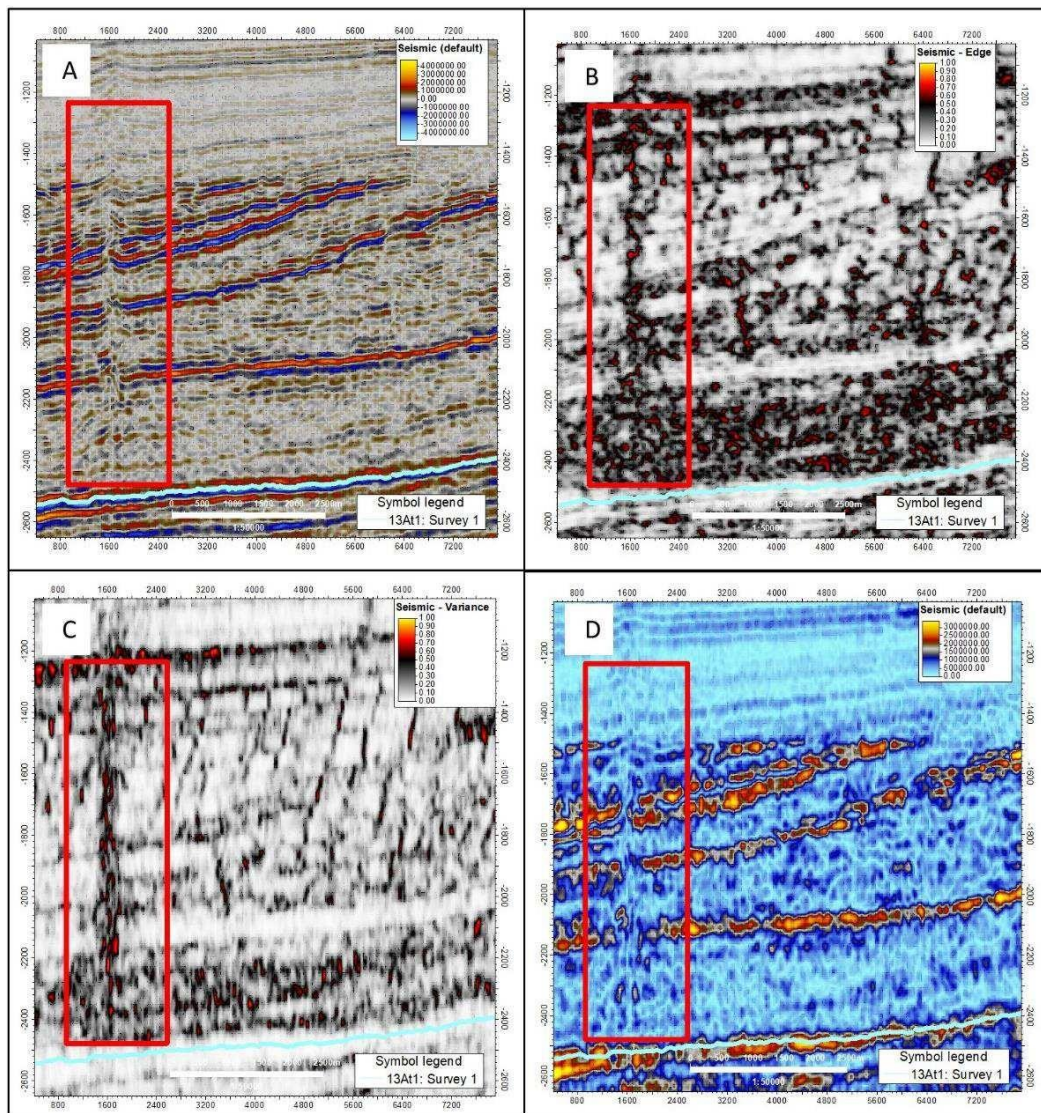


Figure 7.3: a) Seismic section (crossline 482) showing strata that have been disturbed by a vertical structure (red rectangle) which terminates at 16At1 (seismic line below red rectangle). This disturbance propagates from the Aptian age 13At1. b)

Chaos attribute applied; c) Variance attribute applied. The feature is clearer, as there is less noise in the background. d) Envelope attribute does not highlight the vertical feature but rather the strata which are disrupted on either side of the structure.

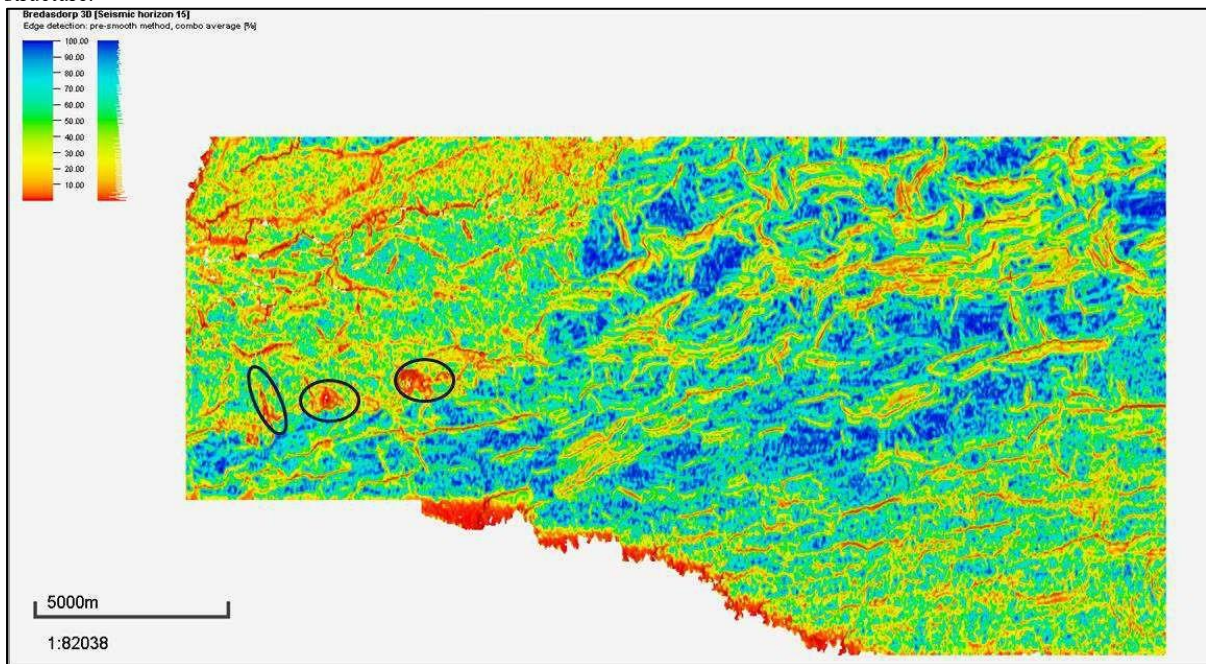


Figure 7.4: Horizon 15At1 with edge detection attribute applied. The black circles indicate the gas escape features seen in Figure 7.1b on time slice 1252. These features form circular structures on surface, with the exception of the left most black circle, which indicates an oblate shape.

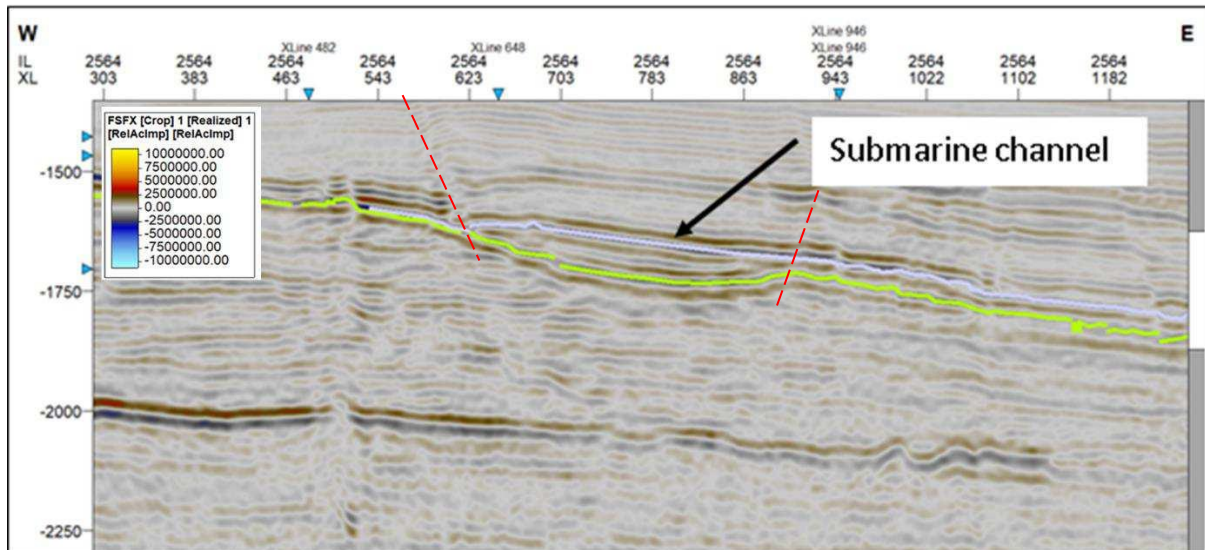


Figure 7.5: Inline seismic section 2564 showing the undulating channel with the green line. The purple line above it presents the channel top. The red lines represent faults which bound the faults on either side.

## 7.2 EROSIVE FEATURES

An erosive feature is also evident on the seismic volume. The incision is made obvious by the undulating strata that is marked by the lime green line in Figure 7.5. The undulation is infilled by sediments which stop at the strata marked in purple (Figure 7.5). Using the TWT difference between these lines, as well as the sonic log, the depth of the channel is calculated to be 1585m and this occurs above the 17At1 horizon, which has an age of between 83.6 to 72 million years (Campanian Age). An envelope time slice and dip ratio attribute were applied to enhance this undulation in the time slice at 1650 sec TWT. The dip ratio time slice shows the erosive feature, which could either be a submarine slump or a channel (marked with a black circle) having an oblate shape, with higher dip ratio around the edges of the feature (Figure 7.6.a). Furthermore, the envelope time slice displays a similar oblate shape (circled in black) which is more pronounced on the northern side where there are brighter (yellow and red) spots (Figure 7.6.b). The envelope horizon attribute shows that the feature is not circular but is rather an elliptical feature with a span of 3594m in the east- west direction, and 3515m in the N-S direction.

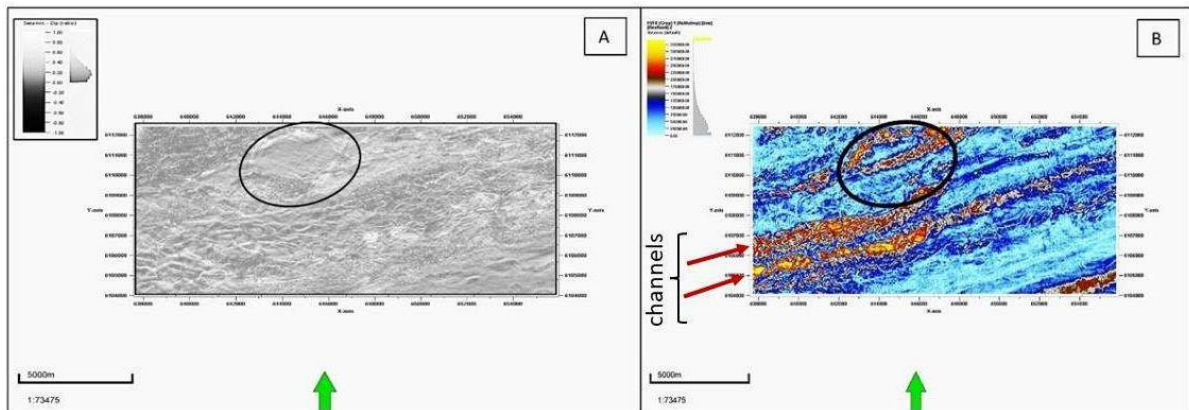


Figure 7.6: Time slice at 1650 sec TWT, with a) dip illumination attribute applied which highlights the sub-circular channel (black circle), with the highest dip ratio at the edges of the channel; b) envelope attribute applied which illustrates the same sub-circular feature, being more pronounced on the northern side by the partial half circular bright spots (red and yellow), and possible channels that are slightly sinuous and parallel shown in the red arrow. The green arrows indicate the north direction.

### **7.3 INTERPRETATION AND DISCUSSION POCKMARKS AND EROSIVE FEATURES**

The abundance, distribution and drivers of pockmarks can impart important information about the slope stability of sedimentary basins and continental margins. Gas migration is indicated by mud volcanoes, gas chimneys and carbonate mounds, with leakage from deeper sources and reservoirs (Anka et al, 2011). Connate water, fresh meteoric water, and hydrocarbon fluids are all indications of fluid migration in the Bredasdorp Basin. Migration of either connate water or hydrocarbon fluid occurs between 9At1 and 13At1 and is due to the compaction of porous and permeable sandstones. If this source was from meteoric water, the rocks would have to be exposed, which does not seem plausible in this case. This occurs mainly in subsiding basins as there is usually sudden compaction of larger layers of shale (Davies, 1997).

In this study, the pockmark structures observed are aligned ENE-WSW, very similar to the parallel faults that are seen in the previous section. It cannot be confirmed if all pockmarks originate from such depths or from similar sources but given that the hydrocarbon source is known to be mainly of Aptian age, it can be interpreted, in conjunction with previous literature discussed in chapter 2, that the escaping fluid represents the hydrocarbons escaping from the source which is known to be 13At1. The related faults may be an additional conduit for fluid migration.

The observed erosive feature slants towards the distal side of the basin. This canyon-like feature is developed within Santonian to Campanian aged sediments, which correlates to the major uplift of the African coast margin and gravity faulting (Selley and van der Spuy, 2016). Similar structures are seen within the Orange Basin on the west coast of South Africa.

The development of submarine channels occurs on either continental shelf or slope because of slumping and mass wasting or turbidity currents. The presence of faults enhances the possibility of slumping. The identified feature has faults on either side, both the eastern and western side, of the observed boundaries. This morphology is archetypal of continental slopes, where thick and relatively uniform sedimentology sequences form canyons due to headward erosion. The propagation of the canyon from the north to the south suggests that the source originated from the southern tip of Africa (Peidou et al, 2017). These faults can be attributed to tectonics, i.e., extensional growth faults. Slumping has previously been recorded during the Agulhas slump, which resulted in a submarine landslide where mass movement occurred from NW to SE of the basin (Peidou et al, 2017). It is important to note that the canyon represents a very short period in the basin's evolution.

## **8. TECTONIC EVOLUTION OF THE BREDASDORP**

## BASIN

The commencement of rifting in the Bredasdorp basin is believed to have been around the late Oxfordian to early Jurassic, however much research is uncertain of this (Thomas, 1999 and Sonibare et al, 2015). The research done in this study does not determine when the rifting commenced, and so literature will be used to describe basin evolution prior to the Valanginian.

The first marine incursions are considered to have occurred during the mid-Jurassic period in the first phase of the synrift. During this phase, the marine incursions were succeeded by major tectonic uplift in the late Jurassic period, during the Tithonian age. The first phase is concluded by early Cretaceous flooding, during the Berriasian age.

The second phase of the synrift, according to the results above, observe the basin to be spreading in the N-S direction, whilst forming normal listric faults. Consequently, the heat from the lithosphere causing the spreading results in thermal subsidence of the basin. This leads to the basin being plunged further into marine conditions, with the sediment source from the North mainly being that of the underlying clastics of the Cape and Karoo Supergroup. However, since the sediment supply is not abundant, sediment starvation results in the formation of an oil-prone source.

The final stage of the second phase of synrift is followed by the reactivation of old faults formed during the Cape Fold Belt Orogeny, with the N-S spread of the basin still being intact. During this time, which is the Hauterivian age, there is an occurrence of marine sediment in the basin as the marine conditions persist, as shown in Figure 5.4, whereby below 13At1 horizon, the strata is parallel to sub-parallel.

In the post-synrift phase, other tectonic forces come into play, mainly transform faulting influenced by the initiation of the breakup of the Falklands during the Aptian age. At this point, the N-S spread of the basin stops being prominent, but the sea level continues to rise, and thus progradation of the basin persists. Unlike earlier Valanginian aged counterparts where there was limited supply of sediment, at this stage, there is an increase in sediment supply to the basin and anoxic conditions develop (which are favorable for the formation of hydrocarbons), and so a source rock can be formed.

Tectonically succeeding this, is a short period of compression which forms the Infanta and Agulhas arches. Although this is a short period of compressions, it has great effects on the basin such that it contributes to a high level of sedimentation resulting aggradation, even though there is progradation still taking place basin wide. The limited supply of oxygen due to the confining arches further exacerbates the anoxic conditions, which amplifies the richness of the organic source.

As the drift phase commences post the syn-rift phase, thermal decay begins to occur. Although thermal

subsidence does not immediately follow thermal decay (during the Aptian age), its effects are seen during the Coniacian age when thermal sag starts to affect the sedimentation of the basin. From the onset of the Coniacian age, progradation of the basin starts to cease, and the environment of deposition changes from deep marine to shallow marine and continental. The tectonic structures that are mainly affecting the basin include the transform faults caused by the AFFZ, as well as the final separation of the Falklands from the southern tip of Africa. This in turn affected the direction of rifting, which predominantly became E- W.

The major shift in tectonic activity affected the stability of the continental slope, resulting in the formation of a slump structure and possibly the initialization of pockmarks and/or other fluid migration structures in the study area.

The final major tectonic uplift event occurs during the Campanian age, which results in the deposition of shelf sediments, i.e., clastic sediments. This event is due to the mantle swell or hotspot that passes through the basin during the Maastrichtian age. Post these events, the basin is infilled by shelf sediments such as sandstones of varying sizes (coarse grained to fine grained), which can be seen in the gamma ray logs interpretation of the artificial neural network.

## **9. CONCLUSIONS**

To summarize, pre-stack time migrated 3D seismic data was imported into Schlumberger PETREL 2018 for analysis and interpretation. The seismic data was tied to the well logs to better correlate the horizons and optimize the picking of horizons. Well logs were used to create artificial neural networks

to predict lithologies, and their patterns were used to predict the most probable environments of deposition. Seismic attributes such as chaos, variance, edge detection, envelope, dip illumination and ant-tracking were applied to the seismic volume after it had been put through the process of data conditioning. The use of attributes such as variance, envelop, chaos and ant-track when optimizing the parameters to favorable conditions is useful for enhancing the structures in seismic sections. Furthermore, when seismic data is used in correlation with the well logs and lithology predicting algorithms such as ANN, it can be used to deduce the sequence stratigraphy of a basin.

Considering all available data, it can be suggested that core logs gas escape would have been a more helpful resource in ground-truthing the ANN model, as well as the well log lithologies. In addition, the gamma ray patterns used to predict progradation, retrogradation, and aggradation are more generalized, and could not hold true in some cases.

The structural framework was considerably helpful in predicting the possible tectonic activity in relation to rifting of the basin, based on the graben patterns and the occurrence of the listric faults. However, a geomechanical study would be useful in predicting the present-day stresses and orientations for a more accurate picture of the tectonism that took place. Although it must be acknowledged that the stresses will most likely have changed over time.

The result in this paper addresses the aims and objectives such that the following was found:

- There is sufficient probable source rock based on the extensiveness of the marine sediments.
- The presence of unconformities may behave as traps for potential gas, together structural traps like faults.
- The presence of possible gas escape structures shows probability of gas rich source.
- faults may be conduits for hydrocarbon migration.

Future possible work could include:

- Mapping faults below 13At1 to determine the onset of rifting.
- Using horizon attributes to determine the depositional environments for each of the horizons.

## 10. REFERENCES

- Admasu, F., Back, S. and Toennies, K., 2006. Autotracking of faults on 3D seismic data. *Geophysics*, 71(6), pp. A49-A53
- Agwu, O.E., Akpabio, J.U., Ekpenyong, M.E., Inyang, U.G., Asuquo, D.E., Eyou, I.J. and Adeoye, O.S., 2021. A critical review of drilling mud rheology models. *Journal of petroleum science and engineering*, 203, p.108659.
- Akinlua, A., Sigidle, A., Buthelezi, T. and Fadipe, O.A., 2015. Trace element geochemistry of crude oils and condensates from South African Basins. *Marine and Petroleum Geology*, 59, pp.286-293.
- Asquith, G.B., Krygowski, D. and Gibson, C.R., 2004. *Basic well log analysis* (Vol. 16). Tulsa: American Association of Petroleum Geologists.
- Ayodele, O.L., van Bever Donker, J.M. and Opuwari, M., 2016. Pore pressure prediction of some selected wells from the Southern Pletmos Basin, offshore South Africa. *South African Journal of Geology* 2016, 119(1), pp.203-214.
- Basir, H.M., Javaherian, A. and Yarak, M.T., 2013. Multi-attribute ant-tracking and neural network for fault detection: a case study of an Iranian oilfield. *Journal of Geophysics and Engineering*, 10(1), p.015009.
- Barnes, A.E., 2007. A tutorial on complex seismic trace analysis. *Geophysics*, 72(6), pp. W33- W43.
- Barnett, W., Armstrong, R.A., and de Wit, M.J., 1997. Stratigraphy of the upper Neoproterozoic Kango and lower Palaeozoic Table Mountain groups of the Cape fold belt revisited. *South African Journal of Geology*, 100(3), pp.237-250.
- Basir, H.M., Javaherian, A. and Yarak, M.T., 2013. Multi-attribute ant-tracking and neural network for fault detection: A case study of an Iranian oilfield. *Journal of Geophysics and Engineering*, 10(1), p.015009.
- Beamish, G.W., 1989. Seismic expression of depositional systems tracts and application to hydrocarbon exploration in Bredasdorp basin, offshore South Africa. *AAPG (Am. Assoc. Pet. Geol.) Bull. ;(United States)*, 73(CONF-890404-).
- Bizarro, P., 1998. Subcircular features and autotracking artefacts in 3D seismic interpretation, a case study from the central North Sea. *Petroleum Geoscience*, 4(2), pp.173-179.
- Bjorlykke, K., 2010. *Petroleum geoscience: From sedimentary environments to rock physics*. Springer Science & Business Media.

Brown, L.F. ed., 1995. Sequence Stratigraphy in Offshore South African Divergent Basins: An Atlas on Exploration for Cretaceous Lowstand Traps by Soekor (Pty) Ltd, AAPG Studies in Geology 41 (41). AAPG.

Cameselle, A.L., 2016. Sedimentary processes and resulting continental margin configuration during large-scale sea-level drawdown: The Messinian Salinity Crisis in the Western Mediterranean Sea, PhD, Universitat de Barcelona, 199pp.

Chehrazi, A., Rahimpour-Bonab, H. and Rezaee, M.R., 2013. Seismic data conditioning and neural network-based attribute selection for enhanced fault detection.

Chopra, S., Castagna, J. and Portniaguine, O., 2006. Seismic resolution and thin-bed reflectivity inversion. CSEG recorder, 31(1), pp.19-25.

Chopra, S. and Marfurt, K.J., 2007a. Seismic attributes for prospect identification and reservoir characterization. Society of Exploration Geophysicists and European Association of Geoscientists and Engineers, 481 pp.

Chopra, S. and Marfurt, K.J., 2007b. Volumetric curvature attributes add value to 3D seismic data interpretation. The Leading Edge, 26(7), pp.856-867.

Chow, J.J., Ming-Chung, L. and Fuh, S.C., 2005. Geophysical well log study on the paleoenvironment of the hydrocarbon producing zones in the Erchungchi Formation, Hsinyin, SW Taiwan. TAO: Terrestrial, Atmospheric and Oceanic Sciences, 16(3), p.531.

Cox, K.G., 1992. Karoo igneous activity, and the early stages of the break-up of Gondwanaland.

Geological Society, London, Special Publications, 68(1), pp.137-148.

Cox, T. and Seitz, K., 2007. Ant tracking seismic volumes for automated fault interpretation. In CSPG CSEG Convention, Alberta (Vol. 670571).

Dalley, R.M., Gevers, E.C.A., Stampfli, G.M., Davies, D.J., Gastaldi, C.N., Ruijtenberg, P.A. and Vermeer, G.J.O., 2007. Dip and azimuth display for 3D seismic interpretation. First Break, 25(12).

Davies, C.P.N., 1997. Hydrocarbon evolution of the Bredasdorp Basin, offshore South Africa— From source to reservoir, PhD, University of Stellenbosch, 1123 pp.

Dentith, M. and Mudge, S.T., 2014. Geophysics for the mineral exploration geoscientist. Cambridge University Press. pp.351-369.

Di, H. and Gao, D., 2014. Gray-level transformation and Canny edge detection for 3D seismic

discontinuity enhancement. *Computers & Geosciences*, 72, pp.192-200.

Dingle, R.V. and Scrutton, R.A., 1974. Continental breakup and the development of post - Paleozoic sedimentary basins around southern Africa. *Geological Society of America Bulletin*, 85(9), pp.1467-1474.

De Rubeis, V., Tosi, P., Gasparini, C. and Solipaca, A., 2005. Application of kriging technique to seismic intensity data. *Bulletin of the Seismological Society of America*, 95(2), pp.540-548.

Ebinger, C.J., Deino, A.L., Tesha, A.L., Becker, T. and Ring, U., 1993. Tectonic controls on rift basin morphology: evolution of the Northern Malawi (Nyasa) Rift. *Journal of Geophysical Research: Solid Earth*, 98(B10), pp.17821-17836.

Evans, B.J., 1997. A handbook for seismic data acquisition in exploration. Society of Exploration Geophysicists 320pp.

EPCM holdings, 2019. What does Brulpadda, Total's offshore discovery, mean for SA's future?

<https://epcmholdings.com/brulpadda-totals-offshore-discovery/> Accessed February 2020

Fitzgerald, P.A.U.L., 2002. Tectonics and landscape evolution of the Antarctic plate since the breakup of Gondwana, with an emphasis on the West Antarctic Rift System and the Transantarctic Mountains. *Royal Society of New Zealand Bulletin*, 35, pp.453-469.

Frizon de Lamotte, D., Fourdan, B., Leleu, S., Leparmentier, F. and de Clarens, P., 2015. Style of rifting and the stages of Pangea breakup. *Tectonics*, 34(5), pp.1009-1029.

Hakami, A.M., Marfurt, K.J. and Al-Dossary, S., 2004. Curvature attribute and seismic interpretation: Case study from Fort Worth Basin, Texas, USA. In *SEG Technical Program Expanded Abstracts 2004*. Society of Exploration Geophysicists, pp. 544-547.

Hashim, M.A., 2015. Investigating subsurface heterogeneities and its impact on the variation in interval velocities: implications to velocity modelling in the Bredasdorp basin (Doctoral dissertation, University of the Western Cape).

Herron, D.A., 2011. First steps in seismic interpretation. Society of Exploration Geophysicists.

Hovland, M., Gardner, J.V. and Judd, A.G., 2002. The significance of pockmarks to understanding fluid flow processes and geohazards. *Geofluids*, 2(2), pp.127-136.

Hu, J.L., Kang, Z.H. and Yuan, L.L., 2014. Automatic fracture identification using ant tracking in Tahe oilfield. *Advanced Materials Research* 962, pp. 556-559.

Johnston, S.T., 2000. The Cape Fold Belt and Syntaxis and the rotated Falkland Islands: dextral transpressional tectonics along the southwest margin of Gondwana. *Journal of African Earth Sciences*, 31(1), pp.51-63.

Khair, H.A., Cooke, D., King, R., Hand, M. and Tingay, M., 2012. Preliminary workflow for subsurface fracture mapping using 3d seismic surveys. A case study from the cooper basin, south australia. Geothermal Research Council Conference, Reno-Nevada.

Koson, S., Chenrai, P. and Choowong, M., 2013. Seismic attributes and their applications in seismic geomorphology. *Bulletin of Earth Sciences of Thailand*, 6(1), pp.1-9.

Lawal, A., Al-Dharrab, S., Deriche, M., Alregib, G. and Amir Shafiq, M., 2016, October. Fault detection using seismic attributes and visual saliency. In *SEG International Exposition and Annual Meeting* (pp. SEG-2016). SEG.

Lawver, L.A., Gahagan, L.M. and Coffin, M.F., 1992. The development of paleoseaways around Antarctica. *Antarctic research series*, 56, pp.7-30

Lines, L.R. and Newrick, R.T., 2004. Fundamentals of geophysical interpretation. Society of Exploration Geophysicists. pp.43-107.

Luo, Y., Higgs, W.G. and Kowalik, W.S., 1996. Edge detection and stratigraphic analysis using 3D seismic data. *SEG Technical Program Expanded Abstracts*, pp. 324-327.

Magoba, M., 2019. Investigation of the acoustic impedance variations of the upper shallow marine sandstone reservoirs in the Bredasdorp basin, offshore South Africa, PhD, University of Western Cape.

Mahlalela, V., Tectonic Evolution of the deepwater Orange Basin (offshore South Africa) using 3D reflection seismic data: implications for hydrocarbon systems, MSc, University of Witwatersrand

Mahlalela, V., Manzi, M.S.D., Jinnah, Z., Bourdeau, J.E. and Durrheim, R.J., 2021. Structural characteristics and 3D seismic detection of gas migration pathways in the deep-water Orange Basin, South Africa. *Marine Geophysical Research*, 42, pp.1-17.

Malehmir, A., Koivisto, E., Manzi, M., Cheraghi, S., Durrheim, R.J., Bellefleur, G., Wijns, C., Hein, K.A. and King, N., 2014. A review of reflection seismic investigations in three major metallogenic regions: the Kevitsa Ni–Cu–PGE district (Finland), Witwatersrand goldfields (South Africa), and the Bathurst Mining Camp (Canada). *Ore Geology Reviews*, 56, pp.423-441.

Manzi, M.S., Gibson, M.A., Hein, K.A., King, N. and Durrheim, R.J., 2012a. Application of 3D seismic techniques to evaluate ore resources in the West Wits Line goldfield and portions of the West Rand goldfield, South Africa Application of 3D seismic techniques. *Geophysics*, 77(5),

pp. WC163-WC171.

Manzi, M.S., Durrheim, R.J., Hein, K.A. and King, N., 2012b. 3D edge detection seismic attributes used to map potential conduits for water and methane in deep gold mines in the Witwatersrand basin, South Africa. *Geophysics*, 77(5), pp. WC133-WC147.

Manzi, M.S.D., 2014. Application of 3D Seismic Analysis Techniques to Evaluate Ore Resources on Kloof, South Deeps and Driefontein Gold Mines, Witwatersrand Basin, South Africa, PhD, University of the Witwatersrand, total.

Manzi, M.S., Hunt, E.J. and Durrheim, R.J., 2019. 3D Reflection Seismic Imaging for Gold and Platinum Exploration, Mine Development, and Safety: Case Studies from the Witwatersrand Basin and Bushveld Complex (South Africa). *Ore Deposits: Origin, Exploration, and Exploitation*, pp.237-256.

Martin, A.K., Goodlad, S.W., Hartnady, C.J.H. and Plessis, A.D., 1982. Cretaceous palaeopositions of the Falkland Plateau relative to southern Africa using Mesozoic seafloor spreading anomalies. *Geophysical Journal International*, 71(3), pp.567-579.

Mauffrey, M.A., Urgeles, R., Berné, S. and Canning, J., 2017. Development of submarine canyons after the Mid-Pleistocene Transition on the Ebro margin, NW Mediterranean: The role of fluvial connections. *Quaternary Science Reviews*, 158, pp.77-93. McClay, K.R. and Scott, A.D., 1991. Experimental models of hanging wall deformation in ramp-flat listric extensional fault systems. *Tectonophysics*, 188(1-2), pp.85-96.

McMillan, I.K., Brink, G.J., Broad, D.S. and Maier, J.J., 1997. Late Mesozoic sedimentary basins off the south coast of South Africa. *Sedimentary Basins of the World*, 3, pp.319-376.

Miller, P., Dasgupta, S. and Shelander, D., 2012. Seismic imaging of migration pathways by advanced attribute analysis, Alaminos Canyon 21, Gulf of Mexico. *Marine and Petroleum Geology*, 34(1), pp.111-118.

Mountain, G.S., Burger, R.L., Delius, H., Fulthorpe, C.S., Austin, J.A., Goldberg, D.S., Steckler, M.S., McHugh, C.M., Miller, K.G., Monteverde, D.H. and Orange, D.L., 2007. The long-term stratigraphic record on continental margins. *Continental margin sedimentation: from sediment transport to sequence stratigraphy*, pp.381-458.

Nietzsche, F. (2005). Common techniques for quantitative seismic interpretation. In Avseth, P. Mukerji, T and Mavko, G (Eds.), *Quantitative Seismic Interpretation: Applying Rock Physics Tools to Reduce Interpretation Risk*. Cambridge: Cambridge University Press.

Norton, I.O. and Sclater, J.G., 1979. A model for the evolution of the Indian Ocean and the breakup of

Gondwanaland. *Journal of Geophysical Research: Solid Earth*, 84(B12), pp.6803- 6830.

Nyasha and Nyaungwa (2019) <https://www.moneyweb.co.za/news-fast-news/namibia-plans-to-add-220-mw-to-electricity-grid-by-2023/> Accessed Sept 2019

Otchere, D.A., Tackie-Otoo, B.N., Mohammad, M.A.A., Ganat, T.O.A., Kuvakin, N., Miftakhov, R., Efremov, I. and Bazanov, A., 2022. Improving seismic fault mapping through data conditioning using a pre-trained deep convolutional neural network: A case study on Groningen field. *Journal of Petroleum Science and Engineering*, 213, p.110411.

Papadimitriou, N., 2017. Geodynamics and synchronous filling of a rift type-basin evolved through compression tectonics (The western margin of the Levant Basin, PhD, Université Pierre et Marie Curie-Paris VI, pages.

Petroleum Agency South Africa (2013). History of Exploration and Production. <http://www.petroleumagency.co.za/index.php/24-petroleum-geology-resources/> Accessed on April 29th, 2020.

Pigott, J.D., Kang, M.H. and Han, H.C., 2013. First order seismic attributes for clastic seismic facies interpretation: Examples from the East China Sea. *Journal of Asian Earth Sciences*, 66, pp.34-54.

Posamentier, H. W., 2004, Seismic geomorphology: Imaging elements of depositional systems from shelf to deep basin using 3-D seismic data: Implications for exploration and development, in R. J. Davies, J. A. Cartwright, S. A. Stewart, S. A. Lappin, and J. R. Underhill, eds., 3-D seismic technology, applications to the exploration of sedimentary basins: Geological Society (London) Memoir 29, p. 11–24.

system from shelf to deep basin using 3D seismic data: implications for exploration and development. Geological Society, London, Memoirs, 29(1), pp.11-24.

Radwan, A.E., 2021. Modeling the depositional environment of the sandstone reservoir in the Middle Miocene Sidri Member, Badri Field, Gulf of Suez Basin, Egypt: Integration of gamma- ray log patterns and petrographic characteristics of lithology. *Natural Resources Research*, 30(1), pp.431-449.

Ramiah, K., Trivedi, K.B. and Opuwari, M., 2019. A 2D geomechanical model of an offshore gas field in the Bredasdorp Basin, South Africa. *Journal of Petroleum Exploration and Production Technology*, 9(1), pp.207-222.

Randen, T., Monsen, E., Signer, C., Abrahamsen, A., Schlaf, J., Sæter, T. and Hansen, J.O., 2000, August. Three-dimensional texture attributes for seismic data analysis. SEG Annual Meeting. OnePetro.

Rijks, E.J.H. and Jauffred, J.C.E.M., 1991. Attribute extraction: An important application in any

detailed 3-D interpretation study. *The Leading Edge*, 10(9), pp.11-19.

Rider, M., 1996. *The Geological Interpretation of Well Logs*. 2nd Edition, Rider-French Consulting Ltd., Sucherland. Süß, M.P. and Shaw, J.H., 2003. P wave seismic velocity structure derived from sonic logs and industry reflection data in the Los Angeles basin, California. *Journal of Geophysical Research: Solid Earth*, 108(B3).

Roux, J., 1997. Potential outlined in southern Outeniqua Basin off S. Africa. *Oil and Gas Journal*, 95(29).

Schlische, R.W., Withjack, M.O., Olsen, P.E., and Kent, D.V., 1999. Rift basin architecture and evolution. Climatic, biotic, and tectonic pole-to-pole coring transect of Triassic-Jurassic Pangaea: International Continental Drilling Program.

Sheriff, R.E., 2002. *Encyclopedic dictionary of applied geophysics*. Society of exploration geophysicists. pp.243.

Silva, C.C., Marcolino, C.S. and Lima, F.D., 2005. Automatic fault extraction using ant tracking algorithm in the Marlim South Field, Campos Basin. *SEG Technical Program Expanded Abstracts*, pp. 857-860.

Sonibare, W.A., Sippel, J., di Primio, R., Anka, Z., Scheck-Wenderoth, M. and Mikeš, D., 2018. Present-day thermal field and Mesozoic-Cenozoic thermal evolution of the Western Bredasdorp Basin (South Africa): An integrated 3D numerical forward modelling approach. *Marine and Petroleum Geology*, 93, pp.57-78.

Storey, B.C., 1995. The role of mantle plumes in continental breakup: case histories from Gondwanaland. *Nature*, 377(6547), pp.301-308.

Talagapu, K.K., 2005. 2D and 3D land seismic data acquisition and seismic data processing. Department of Geophysics, College of Science and Technology Andhra University. Andhra Pradesh.

Taner, M.T., 2001, Seismic attributes, *CSEG recorder*, 26 (7), 49–56.

Thomas, R.J., Von Veh, M.W. and McCourt, S., 1993. The tectonic evolution of southern Africa: an overview. *Journal of African Earth Sciences (and the Middle East)*, 16(1-2), pp.5-24.

Thomson, K., 1999. Role of continental break-up, mantle plume development and fault reactivation in the evolution of the Gamtoos Basin, South Africa. *Marine and petroleum geology*, 16(5), pp.409-429.

Van der Spuy, D., 2003. Aptian source rocks in some South African Cretaceous basins. *Geological Society, London, Special Publications*, 207(1), pp.185-202.

Van Wyk, N.J., 1989. Application of sequence stratigraphy to oil and gas exploration in Bredasdorp basin offshore South Africa. AAPG Bull. ;(United States), 73(CONF-890404-).

Westbrook, G.K., Chand, S., Rossi, G., Long, C., Bünz, S., Camerlenghi, A., Carcione, J.M., Dean, S., Foucher, J.P., Flueh, E. and Gei, D., 2008. Estimation of gas hydrate concentration from multi-component seismic data at sites on the continental margins of NW Svalbard and the Storegga region of Norway. *Marine and Petroleum Geology*, 25(8), pp.744-758.

Winters, S.J., Brink, G.J. and Kuhlmann, S., 1993, April. Integration of Reservoir and Source Distribution with Seismic Sequence Stratigraphy and Geophysical Modelling in The Discovery of Hydrocarbons Within a Cretaceous Sequence, Bredasdorp Basin, South Africa. SAGA Biennial Conference and Exhibition, pp. 224-224.

Wong, J., Han, L., Stewart, R.R., Bentley, L. and Bancroft, J., 2009. Geophysical well logs from a shallow test well and automatic determination of formation velocities from full-waveform sonic logs. *CSEG Record*, 34, pp.21-30.

Yilmaz, Ö., 2001. *Seismic data analysis: Processing, inversion, and interpretation of seismic data*, Society of exploration geophysicists. pp.159-271.

ZHAO, B.L., 2008. Application of multi-component seismic exploration in the exploration and production of lithologic gas reservoirs. *Petroleum Exploration and Development*, 35(4), pp.397- 412.